A Magnetohydrodynamic Theory of Molecular Tornadoes

by

Kelvin Au

A Thesis submitted to the Faculty of Graduate Studies of

The University of Manitoba

in partial fulfillment of the requirements of the degree of

MASTER OF SCIENCE

Department of Physics and Astronomy

University of Manitoba

Winnipeg, Manitoba, Canada

Copyright © 2017 by Kelvin Au

Abstract

A theory of self-gravitating, pressure truncated, rotating molecular filaments with helical magnetic fields is developed to model molecular tornadoes recently observed in the Galactic Centre. A Monte Carlo exploration of the model parameter space is constrained by observations of three molecular tornadoes via three parameters involving observable quantities. It is found that torsional Alfvén wave physics is an important condition in realistic models. A virial analysis indicates that the magnetic field component dominates the pressure component, and both dominate self-gravity.

"Phase diagrams" of numerical solutions to rotating, self-gravitating, unmagnetized cylinders are constructed to better understand solutions with "density inversions" found in the molecular tornado models. By varying free parameters of rotation and equation of state (EOS), five solution types are found and categorized. Self-truncating solutions with density inversions are found to occupy a larger portion of the solution space around the isothermal EOS.

Contributions

This thesis contains the original work of:

> Au, K. and Fiege, J. D. Magnetohydrodynamic Models of Molecular Tornadoes. The Astrophysical Journal, 843:107, July 2017. doi: 10.3847/1538-4357/aa77f6

in Chapter 7. This manuscript is a collaborative work between my thesis advisor Dr. Jason D. Fiege and myself. Numerical results of the magnetohydrodynamic models of molecular tornadoes are based on a code largely written by myself, and began with the help of Dr. Fiege who also taught me the squashing transformation technique. Much of the theoretical work was performed by Dr. Fiege with some contributions from myself. The theoretical work was checked by myself. Aesthetic input on the scatterplot figures was provided by Erica Franzmann. The manuscript was written by myself and edited by Dr. Fiege with comments from an anonymous referee via *The Astrophysical Journal*.

This thesis is written by myself with consultation and editing with Dr. Fiege. The virial analysis of Chapter 6 was done by Dr. Fiege with contributions and check by myself. Chapter 8 on the phase space of self-gravitating, rotating cylinders was done by myself with suggestions of methodology from Dr. Fiege. Dr. Fiege also suggested the method of integrating in terms of pressure instead of density for solving the self-truncating solutions presented in Chapter 8.

Acknowledgements

I would first like to thank my thesis advisor Dr. Jason D. Fiege, who convinced me to undertake graduate studies with him. I have gained invaluable knowledge and skills with his encouragement, guidance, and mentorship. His enthusiasm, drive, and passion for astrophysics has been inspirational ever since my first year undergraduate astronomy course with him.

Thanks to Benson Guest for agreeing to help read a draft of one of the thesis chapters and providing constructive feedback. Thanks to Victor Arendt who helped with a read-through of the Magnetohydrodynamics chapter. Erica Franzmann, Benson Guest, Chelsea Braun, and Keagan Blanchette graciously helped in my preparation for the oral examination by providing feedback, critique, and questions about my presentation, which I am thankful for.

Thank you to the physics faculty whom I have had the opportunity to learn from.

Thank you to the office staff who have provided assistance with administrative tasks. Thank you to Maiko Langelaar for his help with all things IT-related.

Thank you to my fellow physics students who have endured years of assignments, labs, and exams alongside me.

Thank you to my parents Yu-Shui Au, and Yue-Lan Yu who have given me unconditional support during my studies, and have taught me the immeasurable value of an education.

Table of Contents

List of Tables

List of Figures

Chapter 1

Introduction

While counting stars in the Milky Way, Herschel (1785) noticed that there were parts of the sky where stars were apparently absent. Unbeknownst to Herschel, these regions were not actually absent of stars, but dusty clouds in the foreground were blocking the radiation from these stars. Noticeable absence of stars in certain regions against background stars is still a useful method of finding dusty clouds. Counting background stars is useful in mapping their internal structure (Lada et al. 1994, 1999, Alves et al. 1998, 2001).

Since Herschel's first account of the existence of molecular clouds, much has been learned about them, and it would be a mistake to diminish their importance in understanding astrophysical processes. Molecular clouds are complicated, but are part of the stellar life cycle as they are common sites of star formation. Filamentary features are often seen in collections of clouds, so understanding the physical processes involved in the molecular cloud environment provides a underlying knowledge of their description.

Even more recently observed are objects known as molecular tornadoes. What makes these objects particularly interesting is that unlike molecular filaments observed so far, molecular tornadoes possess striking helically wound morphology. Molecular tornadoes are not nearly as thoroughly explored as molecular clouds are despite their somewhat closeby vicin-

ity in the Galactic Centre (GC). However, molecular tornadoes are collections of gas and dust as well, and much of the physics involved are similar, or are at least analogous to those of molecular clouds. There have been three molecular tornadoes found so far: the Pigtail molecular cloud (Pigtail)(Matsumura et al. 2012), Double Helix Nebula (DHN) (Morris et al. 2006), and the Galactic Centre Tornado (GCT) (Sofue 2007). The physics in describing their structure is interesting because it requires the combination of many physical effects such as kinematics, electromagnetism, and fluid dynamics. Furthermore, these astrophysical processes all take place within an extreme and unique environment in the Galactic Centre (GC) known as the Central Molecular Zone (CMZ), which make it an interesting laboratory for testing magnetohydrodynamic (MHD) theories.

Understanding molecular tornadoes requires knowledge of the astrophysical processes surrounding molecular clouds. In Chapter 2, the current physical understanding of molecular is detailed beginning with radiation emission processes, and then detailing relevant astrophysical processes and properties such as turbulence and magnetic fields. Having understood the physics surround molecular clouds, the extreme environment of the CMZ is discussed in Chapter 3 since this is the environment where molecular tornadoes reside. A theoretical background of magnetohydrodynamics is introduced in Chapter 4, which is necessary to understand because molecular tornado structure combines kinematic effects with electromagnetism, and hydrodynamics. Having understood magnetodhydrodynamic theory and having sufficient background of the physics of molecular clouds, a theoretical, and an observational study of filamentary molecular clouds are presented in Chapter 5, which puts Chapters 6, 7, and 8 into context. A virial analysis of molecular tornadoes reveals a useful form of the virial equation outlined in Chapter 6. Chapter 7 describes the details of the radial equilibrium structure of molecular tornadoes when incorporating the combined effects of generally helical magnetic fields, differential rotation, external pressure, and the physics of torsional Alfvén waves. The phenomenon of nonmonotonically changing radial density solu-

tions known as "density inversions" are explored in Chapter 8 in order to better understand them. Finally a brief summary, discussion, and notes on potential future project directions are outlined in Chapter 9.

Chapter 2

Molecular Clouds

The physics of molecular clouds provides a foundational understanding of molecular filaments and molecular tornadoes. Each of these objects are, in a general sense, collections of gas and dust. Molecular clouds are well studied and their properties are generally well understood. Properties of molecular clouds are understood mainly from information gathered by emission from molecules and dust. Radiation emission and radiative transfer are first discussed followed by the relevant energetics, which motivates a discussion of turbulence and magnetic fields. Molecular cloud theory such as Jeans Instability, gravitational collapse, and the role of magnetic fields in star formation follow.

2.1 Molecular Emission

The mass of the interstellar medium (ISM) is approximately 70% hydrogen and its various forms such as neutral hydrogen (HI), ionized hydrogen (HII), and molecular hydrogen (H_2) (Bodenheimer 2011). The remainder is mostly helium (28%), while metals constitute an even lesser amount (2%). Interstellar dust is typically carbonaceous and typically form oxides, silicates, or metals. Hydrogen atoms are observed via the 21-cm radio-wavelength emission

line, which is used to probe neutral gas. This line is produced from the transition of the spin angular momentum of electrons of hydrogen atoms. This is the hyperfine structure or spin and magnetic field coupling between the spin of the electron and magnetic field of the proton. Energy is lost from this process as electrons undergo this "spin-flip" transition; the electron spontaneously transitions from a higher energy state to a lower one, which emits radiation.

Emission from the ISM can also come from vibrational and rotational transitions of molecular energy states. Typical temperatures of the ISM makes it impossible to observe any emission or absorption lines in the visible and radio portions of the electromagnetic spectrum for H_2. The electromagnetic spectrum of H_2 is produced by rotation and vibration that may be observable in temperatures that are much higher than the typical ISM or in shocked regions (Wilson et al. 2013, and references therein). Instead of observing H_2 directly, other molecules, known as tracers, *do* have observable transitions that can be used to estimate the amount of H_2. The total mass can be estimated under an assumption that the abundance between the two molecules are related by empirically determined conversion factors. A typical tracer of H_2 is carbon monoxide (CO). CO is a particularly useful molecule for probing the interior of molecular clouds, which are at the appropriate temperatures and densities for exciting rotational transitions. Typically, the ratio of H_2 to CO is on the order of $\sim 10^4 - 10^5$ (Tielens 2005).

Radiation from the rotational modes of CO can be approximated by the rigid rotator model. Rotation is described by the principle axes of the molecule with corresponding principal moments of inertia. A symmetric top molecule is one that has two equal principle moments of inertia greater than its thrid, such as CO. The rigid rotator inertia is modeled by

$$I = \mu r_0^2, \tag{2.1}$$

where $\mu := m_1 m_2/(m_1 + m_2)$ is the reduced mass with intermolecular separation r_0. As the angular momentum quantum number J transitions, the corresponding energy state is described by

$$E_J = hBJ(J+1), \tag{2.2}$$

where $B := h/8\pi^2 I$, and h is the Planck constant. The frequency of the radiation from a change in energy states is described by (from upper state i to lower state j)

$$\nu_{ij} = 2B(J+1). \tag{2.3}$$

Transitions of rotational modes only occur between adjacent states. Further correction factors are added to Equations 2.2 and 2.3 if the rigid rotator approximation is not assumed, which are due to the small increase in intermolecular separation distance due to centrifugal forces. It is clear from Equation 2.3 and the definition of B that (reduced) mass is inversely proportional to the radiation frequency. This means that more massive molecules tend to have spectra that are observable at lower frequencies. Generally, most transitions for molecules are observed in the near-infrared to radio frequencies. For example, the CO($J = 1 \rightarrow 0$) transition occurs at $\sim 115\,\mathrm{GHz}$ or $\sim 2.6\,\mathrm{mm}$. Equations 2.2 and 2.3 describe a ladder-like change in energy and frequency as they are quantized by J.

2.2 Radiative Transfer

Regardless of whatever radiative source is observed, the radiation emitted must traverse through the interstellar medium (ISM), which has a plethora of gas and dust, before it reaches the observer. There are optical effects within the line of sight (LOS) that must be accounted for.

Radiation intensity at a particular frequency ν is given by I_ν (or equivalently, at a given

wavelength λ by I_λ). As this radiation traverses through the ISM, some of it may be absorbed or further radiation may be emitted through excitation of the atoms and molecules in the medium. Absorptive properties of the medium decrease the intensity while the emission is additive. This process is described by the equation of radiative transfer

$$\frac{\mathrm{d}I_\nu}{\mathrm{d}s} = -\kappa_\nu I_\nu + j_\nu, \tag{2.4}$$

where κ_ν is the absorption coefficient, and j_ν is the emission coefficient. Equation 2.4 describes the rate at which the intensity $\mathrm{d}I_\nu$ changes over a distance $\mathrm{d}s$ as the sum between the absorption $-\kappa_\nu I_\nu$ and emission j_ν processes. The *optical depth* or *opacity* quantifies the absorption of the medium and is defined by

$$\mathrm{d}\tau_\nu := -\kappa_\nu \mathrm{d}s, \tag{2.5}$$

which can be found from Equation 2.4 when $j_\nu = 0$. Optical depth increases away from the observer ($\tau_\nu = 0$ at the observer). The physics described by the equation of radiative transfer (Equation 2.4) links the emission and absorption properties of the medium. Equation 2.4 is easily solved when j_ν and κ_ν are not functions of s. Both sides can first be divided by κ_ν such that

$$\frac{1}{\kappa_\nu}\frac{\mathrm{d}I_\nu}{\mathrm{d}s} = -I_\nu + \frac{j_\nu}{\kappa_\nu}. \tag{2.6a}$$

The *source function* is defined by $S_\nu := j_\nu/\kappa_\nu$. Multiplying both sides by $-\mathrm{d}s$ and using the optical depth (Equation 2.5) results in the expression:

$$\frac{\mathrm{d}I_\nu}{I_\nu - S_\nu} = -\kappa_\nu \mathrm{d}s = \mathrm{d}\tau_\nu. \tag{2.6b}$$

Since the optical depth increases away from the observer, Equation 2.6b can be integrated

by

$$\int_{I_{\nu,0}}^{I_\nu} \frac{\mathrm{d}I_\nu^{'}}{I_\nu^{'} - S_\nu} = \int_{\tau_\nu}^{0} \mathrm{d}\tau_\nu^{'}. \tag{2.6c}$$

Generally, S_ν is not a constant in frequency, and may vary with s. However, if it is assumed that S_ν does not vary with s then this implies that the ratio between absorption and emission coefficients is fixed. Making this assumption S_ν can still vary with ν such that following through with the integration yields a physically meaningful relationship for radiative transfer:

$$I_\nu = S_\nu(1 - \mathrm{e}^{-\tau_\nu}) + I_{\nu,0}\mathrm{e}^{-\tau_\nu}. \tag{2.7}$$

In the limit of high optical depth ($\tau_\nu \gg 0$), it is obvious from Equation 2.7 that $I_\nu = S_\nu$. Equivalently, $I_\nu = S_\nu$ can also be obtained if $\mathrm{d}I_\nu/\mathrm{d}s = 0$ in Equation 2.6a. In other words, high optical depth implies that the radiation field approaches a limit equal to the source function. This is the limit known as *thermodynamic equilibrium* (TE). Consider particle motion and photon motion in the medium. If the mean free path of gas particle collisions is small relative to the scale height of the temperature gradient, then particles can exchange energy with each other to reach equilibrium. In this statistical limit of many energy-sharing collisions within a region of constant temperature, the velocity distribution of these particles follows Maxwell-Boltzmann statistics. Analogously, the photons in a high optical depth medium can exchange energy with the particles and equilibrate provided their mean free path is also much less than the scale height of the temperature gradient. In other words, in TE, both the particles and photons are in equilibrium and can be described by the same temperature T. Such a medium is known as a *blackbody*, and the intensity of the radiation is described by Planck's Law

$$B_\nu(T) = \frac{2h\nu^3}{c^2}\frac{1}{\mathrm{e}^{h\nu/kT} - 1}, \tag{2.8}$$

where k is Boltzmann's constant and c is the speed of light, such that $I_\nu = S_\nu = B_\nu$. However, if the radiation field (the photons) are *not* in equilibrium with the particles, then this is known as *local thermodynamic equilibrium* (LTE), and so $I_\nu \neq S_\nu = B_\nu$. The mean free path of the particles are still usually small relative to the scale height of the local temperature gradient such that the velocity distribution is described by Maxwell-Boltzmann statistics locally, but the intensity is not that of a blackbody.

Brightness Temperature

The brightness temperature $T_B(\nu)$ describes where the temperature of a blackbody has the specific intensity $B_\nu(T_B) = I_\nu$. Thus, in the limit of TE the brightness temperature is given by

$$T_B := \frac{h\nu}{k}\left[\ln\left(\frac{2h\nu^3}{c^2}\frac{1}{I_\nu} + 1\right)\right]^{-1}. \tag{2.9}$$

Radio astronomers typically take advantage of the *Rayleigh-Jeans approximation* in the limit of $h\nu \ll kT$ such that the brightness temperature is given by

$$T_B = \frac{c^2}{2k}\frac{I_v}{\nu^2}. \tag{2.10}$$

While this approximation may be useful for radio astronomers, it is not applicable for submillimetre observations of molecular clouds in general since the frequency of submillimetre emission is larger than that of radio ($\sim 10^2\,\mathrm{GHz}$ compared with $\sim$ MHz) and typical molecular cloud temperatures are somewhat low ($T \sim 10\,\mathrm{K}$).

2.3 Observations

The rotational transition line of CO are excellent for probing molecular clouds. The $J = 1 \to 0$ and $J = 2 \to 1$ transitions are sensitive at densities as low as $\simeq 3 \times 10^3 J^3\ \mathrm{cm}^{-3}$ and

temperature of $\simeq 3J^2$ (Tielens 2005). "Lukewarm" gas is best probed by mid-J ($J = 7 \rightarrow 6$) transition of CO, while higher transitions ($J = 14 \rightarrow 13$) of CO are best at tracing "warm" gas due to shocks.

Molecules like CS, HCN, and HCO^+ have a larger dipole moment and have critical densities that are higher than CO's. This makes these molecules more suitable for observing dense molecular cloud cores. Homonuclear diatomic molecules like H_2, N_2, and O_2 do not possess a permanent dipole moment and so do not undergo radiative rotational transitions (Bodenheimer 2011). This makes these molecules difficult to detect and is why tracer molecules are used instead.

Rare isotopes of C such as ^{13}C may form molecular ^{13}CO. Since the ^{13}C isotope is more rare than the typical ^{12}C atom, the abundance of ^{13}CO is less than that of ^{12}CO. This lower abundance means that its emission is optically thinner than CO, which allows observations to probe higher density gas. Even more rare is the ^{18}O isotope, as its abundance $^{18}O/^{16}O \gg ^{13}C/^{12}C$, so that $C^{18}O$ probes even higher density gas. Langer & Penzias (1990) observe the rare isotopes of $^{13}C^{18}O$ and $^{12}C^{18}O$ to determine the $^{12}C/^{13}C$ ratio across the Galaxy in nine interstellar clouds. They found a gradient in the $^{12}C/^{13}C$ ratio ranging from about 24 at the GC, 30 at 5 kpc, and 70 at 12 kpc. The average ratio is about 57 at the solar radius, and is higher in Orion at 67. Mizuno et al. (1994) try to trace cloud collapse in the process of star formation within the Taurus molecular cloud. They observed $C^{18}O$, which traces molecular hydrogen at densities of $n(H_2) \approx 10^{3-4}\,\mathrm{cm}^{-3}$. These densities are an order of magnitude to two orders of magnitude more dense than that of an average cloud (Mizuno et al. 1994). Mizuno et al. (1994) goes further and observes more exotic molecules such as C_3H_2 and $H^{13}CO^+$, which are collisionally excited at $n(H_2) \gtrsim 10^5\,\mathrm{cm}^{-3}$. At these densities, dense cloud cores may be collapsing to form stars.

2.4 Categorization

The environment of the ISM and the properties of molecular clouds exhibit great variation. Each molecular cloud is unique and categorizing individual clouds into groups of clouds is no easy task. Still, it may be helpful to broadly classify groups of molecular clouds to try and understand what similarities that they may have - whatever they may be. The categorization of molecular clouds is not always consistent between various works, but the terminology generally has a working understanding.

There is a relative hierarchy of cloud structure size. Giant molecular clouds (GMCs) constitute most of the mass of large clouds. GMCs can have masses of $\sim 10^3$ $M_\odot$ to $\sim 2\times10^5$ $M_\odot$, have reasonably well defined boundaries, and typically contains dense substructures (Draine 2011). Categories of giant molecular clouds and dark clouds can be distinguished by mass. Gravitationally bound groups of GMCs are known as GMC complexes. These collections of GMCs mostly have masses $\gtrsim 10^{5.3}$ $M_\odot$ to 6×10^6 $M_\odot$. For example, the Orion molecular cloud (OMC) complex resides approximately 414 pc away from the Sun, has a mass of approximately 3×10^5 $M_\odot$. The OMC complex consists of 3 GMCs: Orion A, Orion B, and the Northern Filament. Neglecting magnetic fields, the virial theorem suggests the mass of these GMCs are 1.2×10^5 $M_\odot$, 0.6×10^5 $M_\odot$, and 0.8×10^5 $M_\odot$, respectively (Draine 2011). These inferred masses can vary up to a factor of 2 when magnetic fields are included. Within Orion A is the Orion Nebula, which is also known as M42 or NGC1976. Cloud complexes are groups of distinct clouds, while clumps consist of self-gravitating entities within clouds that may host star-forming regions, and cores are peaks in density within star-forming regions that may be capable of producing single or multiple stars, depending on the core size. Intensities and radial velocities of molecular lines, and sub-mm thermal emission maps are useful for probing the internal and distinct structures of cloud complexes. Categorization of cloud complexes are summarized in Table 2.1.

Categories	Size (pc)	n_H (cm^{-3})	Mass ($M_\odot$)	Δv (km s^{-1})	T (K)	B (μG)
GMC	$2-20$	10^3-10^4	$10^3-10^{5.3}$	$2-9$	$7-15$	$1-15$
Dark Cloud	$0.3-6$	10^2-10^4	$5-500$	$0.4-2$	$3-15$	$20-30$
Warm Cloud Core	$0.1-0.3$	10^5-10^6	$\sim 10^2$	$0.8-3$	$25-60$	$10-10^3$
Dark Cloud Core	$0.05-0.3$	10^4-10^5	$10-10^3$	$0.3-0.8$	$8-12$	$10-20$

Table 2.1: Categorization of clouds and their associated properties. The linewidth is denoted by Δv, and B is the magnetic field strength. Table adapted from Goodman et al. (1989), Crutcher (1994), Mundy (1994), Mac Low & Klessen (2004), Ostriker et al. (2001), Crutcher (2001), Rathborne et al. (2006), Troland & Crutcher (2008), Draine (2011), Bodenheimer (2011, and references therein).

2.5 Energetics

Molecular clouds collapse when the gravitational energy overcomes thermal, turbulent, and magnetic energies. A brief look at the energetics of an idealized molecular cloud is useful in gauging the relevant physics in molecular clouds. Assuming a spherical cloud with uniform mass distribution, the gravitational energy is described by

$$E_g = -\frac{3}{5}\frac{GM^2}{R}, \tag{2.11}$$

where G is the gravitational constant, M is the cloud's total mass, and R is the radius. The total thermal energy for an isothermal gas is

$$E_{th} = \frac{3}{2}kT, \tag{2.12}$$

where k is Boltzmann's constant, and T is the temperature. Turbulent kinetic energy is described by

$$E_{turb} = \frac{1}{2}M\sigma^2, \tag{2.13}$$

Categories	$\lvert\epsilon_g\rvert$ (eV cm^{-3})	ϵ_{th} (eV cm^{-3})	ϵ_{turb} (eV cm^{-3})	ϵ_{mag} (eV cm^{-3})
GMC	$10^{-3} - 10^{5}$	~ 0	$10^{-3} - 10^{4}$	$0.3 - 60$
Dark Cloud	$10^{-6} - 10^{3}$	~ 0	$10^{-5} - 700$	$100 - 200$
Warm Cloud Core	$300 - 10^{4}$	~ 0	$20 - 10^{3}$	$20 - 10^{5}$
Dark Cloud Core	$3 - 10^{7}$	~ 0	$0.3 - 10^{4}$	$20 - 100$

Table 2.2: Energy densities of cloud complexes based on the maximum range of quantities in Table 2.1.

where $\sigma = \Delta v/\sqrt{8\log(2)}$ is the mean velocity dispersion. Magnetic energy is given by

$$E_{mag} = \frac{B^2}{8\pi} V, \tag{2.14}$$

with magnetic field strength B that is assumed to be constant and uniform, and V is the volume of the spherical molecular cloud. It follows that the energy density is given by $\epsilon = E/V$. Table 2.2 tabulates the maximum energy density ranges based on Table 2.1. It is seen from Table 2.2, that the thermal energetics are unimportant, but turbulence, and magnetic fields can play an important role in the support against self-gravity and consequently in the process of star formation.

2.6 Turbulence

Turbulent fluid motions are characterized by large and unpredictable fluctations in velocity or pressure (Tielens 2005). Turbulence is important in molecular cloud structure because turbulent motions form and shape (filamentary) molecular clouds as suggested by both observations (Federrath et al. 2016, and references therein), and simulations (Kirk et al. 2015, and references therein).

While turbulent motion is stochastic in nature, there is some scale dependence in flow

behaviour. Such a scaling behaviour was first noted by Larson (1981) who found empirically that $\sigma \sim l^q$, where $q = 0.38$ is the linewidth-size scaling index that he found in his study of turbulence and molecular cloud sizes. For GMCs, Solomon et al. (1987) found $q \approx 0.5$. Such scaling relations are further discussed in Section 2.6.1.

A useful parameter that characterizes the onset or presence of turbulence is the *Reynolds number*. A large Reynolds number describes the flow when there is there is significant shear or perpendicular velocity gradients. It is expressed as

$$Re = \frac{vL}{\nu}, \tag{2.15}$$

where v is the mean velocity, L is a characteristic length scale, and ν is the viscosity. This is a ratio of the inertial forces to viscous forces. Turbulent flow occurs when $Re \gg 1$.

Kolmogorov (1941) describes the turbulent scaling relations for incompressible flow. The regime of incompressible flow applies when velocities are negligible compared to the isothermal sound speed $\sigma_{thermal} = (P_{th}/\rho)^{1/2}$, where ρ is the density, and P_{th} is the thermal pressure. This is to say that Kolmogorov turbulence describes a reasonable approximation for subsonic turbulence in a incompressible gas. Energy dissipation occurs for scales smaller than the Reynolds scale l_v when the viscous length scales in the hydrodynamic equations $\sim \nu v(l)/l^2$ exceed the nonlinear coupling terms between scales $\sim v(l)^2/l$, where ν is the kinematic viscosity. Between scales smaller than the system as a whole and larger than l_v, it is assumed the specific energy transfer rate $\dot{\mathcal{E}}$ is conserved, and is the same as the dissipation rate at the scale of l_v. This is known as the *inertial range* of Kolmogorov turbulence and the energy dissipation rate goes at a constant rate as $\dot{\mathcal{E}} \sim v(l)^3/l$ or $v = (\dot{\mathcal{E}}l)^{1/3}$. Kinetic energy density on scales of the wave number $k = 2\pi/l$ is given by $\mathrm{d}(v^2)/\mathrm{d}k$. Thus the *Kolmogorov*

energy spectrum is given by

$$E(k)\,\mathrm{d}k = \frac{2}{3}(2\pi\dot{\mathcal{E}})^{2/3}k^{-5/3}\,\mathrm{d}k, \tag{2.16}$$

which is remarkably similar to the spectrum of Larson's First Law (see Section 2.6.1).

2.6.1 Larson's Laws

Larson (1981) conducted an extensive study of molecular clouds using the observational studies at the time. He compiled the works from 38 different sources in his analysis. His analysis described general trends in the properties of molecular clouds that would later be simply recognized as "Larson's Laws." Larson's Laws can be summarized most simply by turbulence, gravity, and density.

Turbulence: Size-Linewidth Relation

Larson (1981) described a consistent relationship between the spectral lines (CO, H_2CO, NH_3, OH, among others) of numerous molecular clouds, and their maximum linear extent (a characteristic length) L. This size-linewidth relation, the first of Larson's Laws, relates the 3-dimensional velocity dispersion with L. The velocity dispersion of a gas can be determined by observing the Doppler broadening of molecular lines caused by the motion of the gas along the line of sight. Except for the densest central regions of cores, the line width is usually wider than can be explained solely by the thermal component of the gas as a nonthermal component from turbulence is included in the velocity dispersion. This first law says that the velocity dispersion is directly proportional to the size of the molecular cloud. An assortment of molecular clouds were organized in a log-log plot of σ against L. Larson found that the

scatter of these objects fitted a straight line such that

$$\frac{\sigma}{(\mathrm{km\ s^{-1}})} = 1.10 \left(\frac{L}{\mathrm{pc}} \right)^{0.38}. \tag{2.17}$$

Larson (1981) drew the comparison of this scaling relationship with that of the Kolmogoroff law (Equation 2.16). The similarity in the scaling relationship may be explained if observed motion in molecular clouds are due to subsonic turbulence.

Gravity: Mass-Linewidth Relation

Like the first of Larson's Laws, the second law was discovered via a log-log relationship between σ and the molecular cloud mass M as

$$\frac{\sigma}{(\mathrm{km\ s^{-1}})} = 0.42 \left(\frac{M}{\mathrm{M_\odot}} \right)^{0.20}. \tag{2.18}$$

Larson (1981) found that most of the molecular clouds in his study were in approximate virial equilibrium. For molecular clouds to remain coherent, it would be expected that the turbulent motions that tend to dissipate the structure roughly balance the confining gravitational pressure. Such turbulent motions may also cause molecular cloud substructures to form such as filaments (McKee & Ostriker 2007).

Density: Size-Density Relation

The third law was derived from the two aforementioned laws. Roughly, the density goes as $\rho \sim M/L^3$. By equating Equations 2.17 and 2.18, the density goes as $\rho \sim L^{-1.10}$ or as the average volume density

$$\frac{\langle n(H_2) \rangle}{(\mathrm{cm^{-3}})} = 3400 \left(\frac{L}{\mathrm{pc}} \right)^{-1.10}. \tag{2.19}$$

This also implies that the surface density Σ of molecular clouds is roughly constant since $n \propto L^{-1}$ and $\Sigma \propto M/L^2$, then $\Sigma \propto \rho L \propto nL \propto constant$.

Comments on Larson's Laws

Since the pioneering work of Larson (1981), further investigations of Larson's Laws have been conducted such as in Solomon et al. (1987), Heyer et al. (2009), Lombardi et al. (2010), and in simulations (Kritsuk et al. 2013). Such investigations have noted differences in Larson's Laws such as in the power index of the size-linewidth relationship. Solomon et al. (1987) found an analogous size-linewidth relationship for GMCs that behaved as $\sigma \sim R_{pc}^{0.5}\,\mathrm{km\,s^{-1}}$, where $R_{pc} \equiv R/(1\,\mathrm{pc})$. Heyer et al. (2009) found a scaling relation like Larson's third law in GMCs located in the Milky Way that follows $\Sigma \sim R^{-1}$. The size-linewidth relation has even been observed in extragalactic GMCs that scales as $\sigma \sim R^{0.6}$ (Bolatto et al. 2008). The general scaling relationships of Larson's Laws set a foundational knowledge of how molecular clouds behave in the broadest sense, since they are the result of fundamental physics of turbulence and virial equilibrium.

2.7 Magnetic Fields

Magnetic fields permeate the ISM, and play a role in many physical processes throughout the Galaxy such as star formation and particle acceleration. A number of techniques can be used to probe the Galactic magnetic field. Among them, radio synchrotron emission is one of the most promising as it is observed everywhere in the Galaxy, and the Faraday rotation of this radiation is measurable. More limited tools include that of starlight polarization measurements, which provide directional information on the magnetic fields up to a few kpc, but not magnitudes (Landecker 2012, and references therein). Galactic magnetic fields can be measured via Faraday rotation of signals from pulsars and extragalactic sources (Landecker

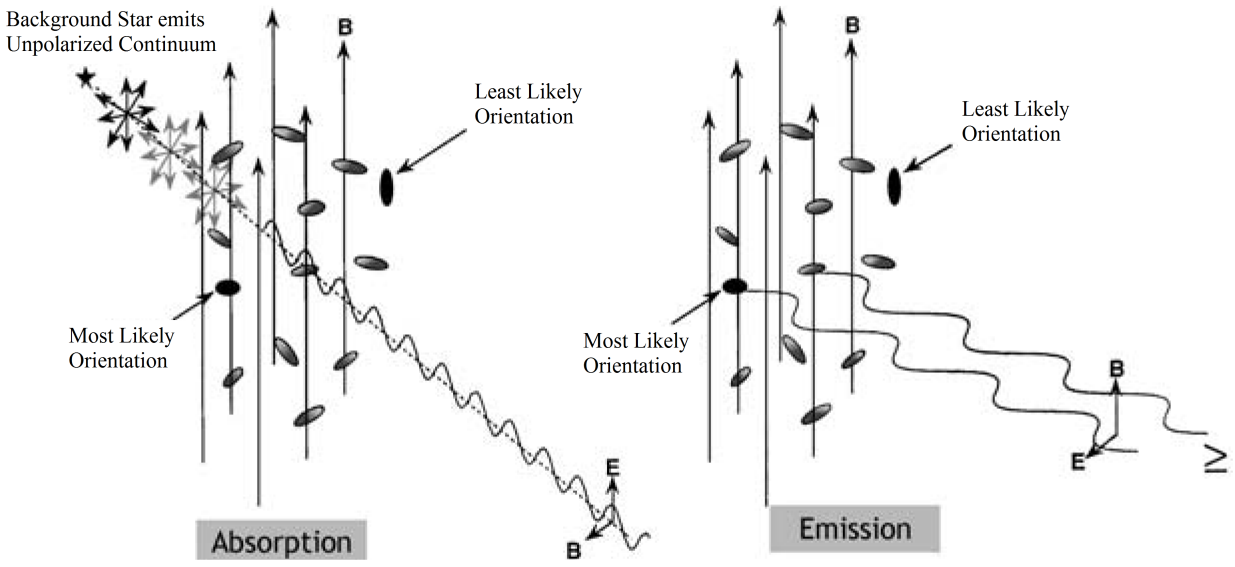

Figure 2.1: (left) Schematic of how dust grains aligned with magnetic fields polarize background source radiation. (right) Polarized emission from dust grains aligned with their long axis orthogonal to the magnetic field. Figure adapted from Weintraub et al. (2000).

2012, and references therein). Generally, the Galactic magnetic field strength is on the order $\sim \mu$G (Landecker 2012, and references therein).

There are two primary methods for obtaining strength measurements of the magnetic field in molecular clouds. Zeeman splitting measures the LOS component of the magnetic field via magnetic field interactions with atomic structure. The Chandrasekhar-Fermi (CF) method measures the plane-of-sky component by considering the effect of nonthermal turbulence. First, the effect of magnetic fields on dust grains and the resulting submillimetre polarization is discussed, followed by a discussion of the CF method, and afterwards the measurement of magnetic field strengths by Zeeman splitting is discussed.

2.7.1 Polarization by Dust Grains

The rotation of dust grains may be due to thermal rotation or "Brownian rotation." This is described by the angular velocity of grain rotation $\omega_T \approx (kT_{gas})^{1/2}/(\rho a^5)^{1/2}$, where a is an effective grain radius, ρ is its density, and T_{gas} is the gas temperature (Lazarian et al. 1997).

Alternatively, suprathermal rotation is a possibility. Suprathermal rotation may be due to irregularities in the dust grain shape or surface which may cause variation in photoelectric emissivity, and random surface site distributions on which hydrogen molecule recombination can be catalyzed (Purcell 1979). The net result of this leads to unbalanced torques and spinning of the grain. Elongated dust grains have the tendency to align their long axis perpendicular to magnetic field lines (Davis & Greenstein 1951, Gold 1952, Morris & Serabyn 1996, Lazarian et al. 1997). Grains must rotate to orient themselves perpendicular to the magnetic field lines. An aspherical dust grain will have its axis of greatest inertia aligned with the angular momentum due to the dissipation of rotational kinetic energy. Thermal, and superthermal rotation, along with possible paramagnetic alignment, radiative torques, and mechanical alignment from collision with gas flows (Gold 1952, Lazarian et al. 1997) tend to orient aspherical dust grains such that their long axis lies orthogonal to magnetic fields in their environment.

This behaviour has interesting effects on the polarization of radiation, and is a useful tool in determining the geometry of magnetic fields. Dust grains may emit polarized radiation as depicted in the right side panel of Figure 2.1. Thermal emission from dust grains is linearly polarized in the millimetre or sub-millimetre wavelengths. Dust grains are aligned orthogonal to the environmental magnetic field. The emission is such that the electric field vector $\boldsymbol{E}$ points parallel with the long axis of the grains, and the resulting component of the magnetic field vector $\boldsymbol{B}$ is perpendicular to the polarization vector. At millimetre wavelengths, there is minimal absorption of dust grain emission, which makes them excellent probes for high density regions such as molecular clouds.

Light is also polarized by interstellar absorption. This phenomenon is depicted schematically in the left panel of Figure 2.1. Since dust grains align their long axis orthogonal to the magnetic field, the parallel component electric field vector $\boldsymbol{E}$ with the dust grains is absorbed, and the resulting observed magnetic field vector $\boldsymbol{B}$ is parallel with the polarization

vector. This technique is only useful at low optical depth, and therefore cannot be used to observe magnetic fields in dense regions of molecular clouds where stars form.

2.7.2 Chandrasekhar-Fermi Method

The Chandrasekhar-Fermi (CF) method is a technique used to estimate the magnitude of the plane-of-sky magnetic field component (Chandrasekhar & Fermi 1953*a*, Crutcher et al. 2003). From the irregular fluctuations in polarization of distant stars, Chandrasekhar & Fermi (1953*a*) reasoned that the Galactic magnetic field lines are not straight, but perhaps "wavy." This suggests that the magnetic fields are affected by turbulence such that the plane of polarization is deviated from the direction of the Galactic spiral arms. The nonuniform nature of the magnetic field lines have a perturbed nonthermal component that can be described by the Alfvén speed $v_A = B/\sqrt{4\pi\rho}$ where B is the magnetic field strength, and ρ is the density of the medium. Magnetic and velocity perturbations (δB and δv, respectively) are then related by $\delta v = \delta B/\sqrt{4\pi\rho}$. Thus, the average plane-of-sky magnetic field $B_\perp$ will be dispersed according to

$$B_\perp = Q\sqrt{4\pi\rho}\frac{\delta v}{\delta\phi}, \tag{2.20}$$

where Q is a correction factor of order unity, and $\delta\phi = \delta B/B_\perp$ is the dispersion in the polarization emission position angles (Crutcher et al. 2003). A difficulty in applying the CF method is the required knowledge of the plane-of-sky velocity perturbation δv. However, it may be possible to infer δv from the radial velocity dispersion. Ostriker et al. (2001) investigated the CF method by simulating interstellar plasmas and calibrated $Q \approx 0.5$ for molecular cloud conditions. As an estimate, the Chandrasekhar-Fermi method may be useful, though there still exists some uncertainty as numerical simulations have suggested it tends to overestimate the magnetic field strength by a factor of approximately 2 (Heitsch & Li 2004, and references therein).

2.7.3 Zeeman Splitting

Zeeman splitting is another useful tool for probing magnetic fields within molecular clouds (Landecker 2012, and references therein). Zeeman splitting is a mechanism that reveals information about the component of the magnetic field that is parallel to the LOS. The mechanism arises from the interaction between external magnetic fields and the total angular momentum of different transition states. These transitions are quantized, and so there is a ladder of energy states split between the orbital angular momentum and spin angular momentum components. In the absence of a magnetic field, atoms intrinsically possess quantized energy levels due to the spin-orbit interaction between electrons and their nuclei known as the fine structure interaction. When an external magnetic field is introduced then there is a spin-magnetic field interaction that splits the energy levels. This is to be distinguished from the hyperfine interaction between the magnetic moments of the electron(s) of an atom and its nucleus. These quantized energy levels are proportional to the strength of the magnetic field, and it is in this measurement of the spectral lines that the strength of the magnetic field can be deduced. There are three separate frequencies that a spectral line is split into by an external magnetic field B: 1. $\nu_0 - \nu_Z$, 2. ν_0, and 3. $\nu_0 + \nu_Z$, where ν_0 is the line frequency, $\nu_Z = B \times Z$, and Z is the Zeeman sensitivity in Hz/μG. The Zeeman-split line frequencies are easily distinguished when B is sufficiently large such that $\nu_Z \sim \Delta\nu$, where $\Delta\nu$ is the line width and is much less than the turbulent line width. All three line frequencies are linearly polarized in the plane of the sky such that the ν_0 component is parallel to the magnetic field direction while the $\nu_0 - \nu_Z$ and $\nu_0 + \nu_Z$ components are perpendicular. For a magnetic field parallel to the LOS, the $\nu_0 - \nu_Z$ and $\nu_0 + \nu_Z$ components are circularly polarized in opposite direction. The magnetic field strength can be derived from variations in the circular polarization (Crutcher et al. 2003).

Crutcher et al. (2010) provide a table of the LOS component of the magnetic field $B_{\|}$ in a number of molecular clouds along with their volume densities based on Zeeman observations.

The median field strength within molecular clouds of volume densities $n < 300$ cm^{-3} is approximately 5 μG, while those with larger densities scale approximately as $49 n_4^{0.5}$ μG, where $n_4 = n_H/10^4\,\mathrm{cm}^{-3}$ (Draine 2011).

2.8 Jeans Instability

Molecular clouds are self-gravitating, and therefore not in equilibrium with the ISM pressure. The presence of magnetic fields, turbulent pressure, and gravity allow molecular clouds to remain stable on timescales of $\simeq 3 \times 10^4$ years (Tielens 2005). Instabilities cause molecular clouds to clump under self-gravity, which can cause strongly self-gravitating cores to form. For a general grasp of how instabilities cause molecular clouds or filaments to clump, it is useful to discuss the Jeans Instability, which describes instability of a nonrotating, unmagnetized, initially uniform and stationary, and self-gravitating gas (Jeans 1902). This presents a purely hydrodynamic system, thus the relevant fluid equations are the continuity equation

$$0 = \partial_t \rho + \boldsymbol{\nabla} \cdot (\rho \boldsymbol{v}), \tag{2.21a}$$

the momentum equation

$$\rho \partial_t \boldsymbol{v} + \rho(\boldsymbol{v} \cdot \boldsymbol{\nabla})\boldsymbol{v} = -\boldsymbol{\nabla} P - \rho \boldsymbol{\nabla} \Phi, \tag{2.21b}$$

and Poisson's equation

$$\nabla^2 \Phi = 4\pi G \rho, \tag{2.21c}$$

where t is time, ρ is density, $\boldsymbol{v}$ is velocity, P is pressure, G is the universal gravitation constant, and Φ is the gravitational potential. The equation of state is assumed to be isothermal $P = \sigma^2 \rho$, where velocity dispersion accounts for both a thermal and nonthermal turbulent component such that $\sigma = \sqrt{\sigma^2_{thermal} + \sigma^2_{nonthermal}}$. The gas is subject to perturbations of

the form $f_1^* = f_1(\boldsymbol{x})\mathrm{e}^{i(\boldsymbol{k}\cdot\boldsymbol{x}+\omega t)}$, where f_1 is the perturbed quantity, $\boldsymbol{k}$ is the wave vector, $\boldsymbol{x}$ is the position vector, and ω is the angular frequency of the perturbation. After linearizing Equations 2.21 and some algebra, the dispersion relation is given by

$$-\omega^2 = -k^2\sigma^2 + 4\pi G\rho_0. \tag{2.22}$$

By defining

$$k_J := \frac{4\pi G\rho_0}{\sigma^2} \tag{2.23}$$

as the Jeans wavenumber, the dispersion relation can be written in an especially physically illuminating way as

$$-\omega^2 = (k_J^2 - k^2)\sigma^2. \tag{2.24}$$

In this form, the dispersion relation reveals that unstable solutions are those which $-\omega^2 > 0$, or equivalently when $k_J > k$. This critical, Jeans wavenumber provides a *Jeans length* that describes the characteristic scale where the cloud breaks apart. Via $k_J = 2\pi/\lambda_J$, the Jeans length is given by

$$\lambda_J = \sqrt{\frac{\pi\sigma^2}{G\rho_0}}. \tag{2.25}$$

From the Jean's wavelength, the characteristic mass of the clumps can be calculated via $M = \rho_0 V$, where the volume V is of a uniform sphere with radius $R_J = \lambda/2$. Thus, the *Jeans mass* is given by

$$M_J = \frac{4\pi}{3}\rho_0\left(\frac{\lambda_J}{2}\right)^3. \tag{2.26}$$

Since $M_J^{1/3} \propto \lambda_J \propto \sigma \propto \sigma_{nonthermal}$, turbulence acts to support the cloud by increasing the fragmentation scale.

It should be noted that the Jeans Instability is not entirely realistic and has been the subject of some controversy. Known as *Jeans Fudge*, the solution to Poisson's equation

in an infinite, constant density medium is not unique. It is assumed that $\nabla^2\Phi = 0$ by symmetry, which may be physically reasonable, but cannot be obtained from rigorous mathematics. Nevertheless, it is generally regarded that the Jeans Instability provides a useful understanding of the scales which gravitational instabilities develop in molecular clouds.

2.9 Gravitational Collapse of a Sphere

Internal gas pressure within a molecular cloud is insignificant initially as radiation from molecular transitions cools the gas efficiently. The free-fall timescale is derived from the gravitational collapse of a pressure-free spherical cloud due to its self-gravity, which is described by

$$\begin{aligned} \tau_{ff} &= \left(\frac{3\pi}{32G\rho_0}\right)^{1/2} \\ &\simeq 0.5 \times 10^6 \mathrm{yr}\left(\frac{n}{10^4\,\mathrm{H_2\,cm^{-3}}}\right), \end{aligned} \tag{2.27}$$

although pressure gradients become important at later times. Since the density of a molecular cloud is higher in its centre, τ_{ff} suggests that the core will be first to collapse, followed by the outer layers. For a uniform sphere of density ρ_0, τ_{ff} implies that all layers of the sphere collapse at the same time, which is known as *homologous collapse*.

2.10 Role of Magnetic Fields in Star Formation

Cases such as that of Jeans Instability in nonmagnetized scenarios provide a foundational knowledge and insight as to how further physical interactions might affect the star formation process. There are two regimes as to how magnetic fields influence the collection of interstellar matter to form dense molecular clouds, and then proceed to collapse and form stars. They provide limiting cases as to how magnetic fields may control formation.

2.10.1 Bonnor-Ebert Stability

Stability of a nonmagnetic, self-gravitating spherical cloud under the influence of an external pressure and supported by internal pressure can be described by the virial relation

$$0 = 2K + W, \tag{2.28}$$

where kinetic energy term is given by $K = (3/2)M\sigma^2 = (3/2)(P - P_S)V$ for an isothermal sphere of radius R and volume V under external pressure P_S, and W is the gravitational energy given by Equation 2.11. Isolating for P_S yields

$$P_S = CR^{-3} - DR^{-4}, \tag{2.29}$$

where $C \equiv 3M\sigma^2/4\pi$ and $D \equiv 3GM^2/20\pi$. Equation 2.29 characterizes a range of P_S where the cloud is *Bonnor-Ebert stable*, that is, where the cloud is in balance between external pressure, internal pressure, and self-gravity. There exists a maximum P_S of Bonnor-Ebert stability as described by Equation 2.29. When P_S exceeds this critical point, the cloud is *Bonnor-Ebert unstable* and internal pressure is not sufficient to keep the cloud from collapsing under self-gravity and external pressure. This critical pressure is described by $P_{S,crit} = (27/256)(C^4/D^3) \approx 0.11(C^4/D^3)$ as determined from Equation 2.29.

Magnetic fields threading through a cloud provide support against collapse. A magnetic energy term is introduced to the virial relation via an additive term $B^2V/4\pi$, which can be written in terms of the magnetic flux $\Phi = B(4\pi R^2)$, where B is the magnetic field strength. By including magnetic fields, Equation 2.29 can be rewritten as

$$P_S = CR^{-3} - D\left(1 - \frac{5}{144\pi}\frac{1}{G}\frac{\Phi^2}{M^2}\right)R^{-4}. \tag{2.30}$$

It is more easily seen from Equation 2.30 that the magnetic field support and self-gravity

both scale as R^{-4}, but with opposing signs. Thus, there exists a critical point where these two effects balance exactly, which is obtained where the term in parenthesis on the right-hand side of Equation 2.30 is equal to zero such that

$$\frac{M}{\Phi} = \frac{1}{12}\sqrt{\frac{5}{\pi}}\frac{1}{\sqrt{G}} \approx 0.11\frac{1}{\sqrt{G}}. \tag{2.31}$$

This is the criterion which separates *subcritical* from *supercritical* clouds.

2.10.2 Subcritical and Supercritical Clouds

The two cases revolve around the scenario where magnetic and gravitational energies are in balance such that the equilibrium of the cloud is described by Equation 2.31, or more generically in terms of the magnetic critical mass as

$$M_\Phi \equiv c_\Phi \frac{\Phi}{\sqrt{G}}, \tag{2.32}$$

(Nakano & Nakamura 1978) which has some dependence on the molecular cloud morphology. The coefficient c_Φ is dependent on density and magnetic field distributions within the cloud. For the isothermal sphere, $c_\Phi \approx 0.11$ as shown above in Equation 2.31. Another example from Tomisaka et al. (1988*a*) found $c_\Phi = 0.17$ as the critical value for a cold cloud threaded by a poloidal field and constant flux-to-mass ratio. Thus, the two cases describing molecular cloud collapse and equilibrium are the supercritical and subcritical cases where $M > M_\Phi$ and $M < M_\Phi$, respectively.

In the subcritical cloud case, the magnetic field is the dominant mechanism that influences the formation and evolution of molecular clouds, and the formation of protostars from gravitational collapse of dense cores. In this regime, the mass-to-flux ratio $M/\Phi = c_\Phi/\sqrt{G} < 1$ and ambipolar diffusion (see Section 4.3) plays an important role by accumulating mass in

cloud cores. If the magnetic field is only frozen into ionized gas and dust, then neutral gas and dust are able to contract gravitationally toward the core, albeit at a relatively slow rate on the order of the ambipolar diffusion timescale τ_{ff} (Section 4.3, Equation 4.17). This way, only the mass accumulates in the cloud core, and not the magnetic flux. The mass-to-flux increases for the core. With supercritical mass-to-flux, cores can collapse to form stars when the magnetic flux dissipates by ambipolar diffusion. Magnetic fields alone are not enough to prevent gravitational collapse. Turbulence may be the more important factor in providing molecular cloud support (Mac Low & Klessen 2004).

Chapter 3

Central Molecular Zone

The Central Molecular Zone (CMZ) is an approximately 500 pc region in the Galactic Centre that extends from roughly $l = -1.0°$ to $+1.5°$ (Langer et al. 2017). The CMZ surrounds the central supermassive black hole and is a much more extreme environment compared to other parts of the Galaxy; much of its properties and characteristics are unique in comparison, and is currently a very active area of research (Morris & Serabyn 1996, Longmore et al. 2013, Rathborne et al. 2014, Kruijssen et al. 2014, 2015, Federrath 2016, Federrath et al. 2016, Henshaw et al. 2016, Langer et al. 2017). Morris & Serabyn (1996) and Mills (2017) provide an overview of the CMZ. This section highlights points made by Morris & Serabyn (1996) and Mills (2017) as to how the CMZ is an extreme environment relative to typical Galactic disk conditions. This is important to understand, since the CMZ environment is where molecular tornadoes are observed (Morris et al. 2006, Sofue 2007, Matsumura et al. 2012). As a brief overview, some of the extreme properties compared to the Galactic disk are (Mills 2017, and references therein)

1. high densities on the order of $10^4\,\mathrm{cm}^{-3}$, which is several orders of magnitude greater compared to the Galactic disk;

2. extreme turbulence as evident by line widths of $15 - 50\,\mathrm{km\,s}^{-1}$ compared to $\sim 1 -$

$10\,\mathrm{km\,s^{-1}}$ of giant molecular clouds in the Galactic disk;

3. hot molecular gas with typical temperatures of $50 - 100\,\mathrm{K}$ and as high as $400 - 600\,\mathrm{K}$; and

4. strong magnetic fields with strengths of $\sim 10\,\mu\mathrm{G} - \mathrm{mG}$ (Ferrière 2009).

Hot, dense, turbulent molecular gas threaded by strong magnetic fields in the GC make it an extreme environment for astrophysical processes.

3.1 Density

Giant molecular clouds constitute the most dense gas in the CMZ. Six of eight of the most massive cloud concentrations in the CMZ lie at positive latitudes (Longmore et al. 2013). There is a large cloud population in the CMZ may be an indicator for the density of these objects. A large population suggests that these clouds are long-lived and gravitationally bound. Molecular clouds in the GC experience strong tidal forces due to strong gradients in total mass distribution within a radius of 1 kpc. These tidal forces are compensated by the self-gravity of a molecular cloud. A typical radius of 50 pc from the orbital model of Kruijssen et al. (2015) implies that the stability of these clouds requires a critical density above $10^4\,\mathrm{cm^{-3}}$ (Güsten & Downes 1980).

Observations of CO suggest densities of $\sim 10^4\,\mathrm{cm^{-3}}$ (Bally et al. 1988), $\gtrsim 10^4\,\mathrm{cm^{-3}}$ (Tsuboi et al. 1999) from CS observations, and $\gtrsim 10^5\,\mathrm{cm^{-3}}$ from observations of HCN (Jackson et al. 1993). Even larger densities have been suggested from the analyses of some individual clouds. CS observations of M-0.02-0.07, and the Sickle cloud suggest densities from $\sim 10^5$ to $10^6\,\mathrm{cm^{-3}}$ (Serabyn & Guesten 1991, Serabyn et al. 1992). HC_3N observations of the Sgr B2 cloud indicates that it harbours even greater densities in excess of $10^7\,\mathrm{cm^{-3}}$ at the core (Lis & Goldsmith 1991).

3.2 Temperature

NH_3 studies were first indicative of the hot temperatures of CMZ clouds (Güsten et al. 1981, Morris et al. 1983). Such studies suggest average gas temperatures of $60 - 120\,\mathrm{K}$ (Guesten et al. 1985). These high temperatures in NH_3 are supported by observations of CH_3CN and CH_3CCH by Guesten et al. (1985), which reveal temperatures of $50 - 100\,\mathrm{K}$. Quadrupole rotational transitions of H_2 reveal hot dense gas of $600\,\mathrm{K}$ (Rodríguez-Fernández et al. 2001). Extremely excited NH_3 shows that hot gas is present toward Sgr B2 at $600 - 700\,\mathrm{K}$ (Mauersberger et al. 1986). Hot gas around $400\,\mathrm{K}$ appears to be present among CMZ clouds in general as NH_3 transitions indicate (Mills & Morris 2013). Hot gas is most likely to be present due to the observed excitation of NH_3, but there is the possibility that this may be due to recently formed excited NH_3 or is a low density component whereby the NH_3 has not yet reached thermodynamic equilibrium with the surrounding gas.

3.2.1 Heating

Far-ultraviolet radiation may play a significant role in the high temperatures observed in the CMZ. The GC houses a large population of young massive stars that ionize the ISM to tens of parsecs (Mills 2017, and references therein). This may be most important for heating diffuse gas because heating does not penetrate to dense cloud interiors such as those with temperatures of $50 - 200\,\mathrm{K}$ traced by NH_3. The interface of molecular gas in the CMZ with the radiation field forms photo-dominated regions (PDR), which may be responsible for $10 - 30\%$ of the observed warm ($T \sim 150\,\mathrm{K}$) H_2 column density (Rodríguez-Fernández et al. 2001, 2004). PDR heating cannot penetrate to dense cloud interiors where molecules like H_2CO are found, and so may not be important in heating dense cloud interiors (Ao et al. 2013).

X-ray heating in X-ray dominated regions (XDRs) penetrates more deeply into dense

regions than ultraviolet does. The GC is a source of X-ray emission (Koyama et al. 1989), and there may be X-rays from diffuse hot plasma as well (Koyama et al. 1996). XDRs can penetrate 10× more deeply than a PDR (Rodríguez-Fernández et al. 2004), but may still not account for temperatures above 100 K (Ao et al. 2013). This is because the total X-ray luminosity is too low even though a PDR has the potential to heat the entire column of observed warm CMZ gas (Mills 2017).

Cosmic rays are particles (mostly protons) accelerated to relativistic speeds that are thought to originate from supernova remnants (Ackermann et al. 2013). Cosmic rays can penetrate deeper into CMZ gas than X-rays. The ionisation rate in the CMZ is proposed to be an order of magnitude or more above the typical interstellar rate (Güsten et al. 1981, Indriolo & McCall 2012). Ionisation rates several orders of magnitude above typical interstellar values can provide reasonable heating to explain CMZ gas temperatures. Cosmic rays are highly penetrative and can uniformly heat cloud interiors to high temperatures even at high $10^4 - 10^5\,\mathrm{cm}^{-3}$ densities (Ao et al. 2013). Molecules are preferentially heated by cosmic ray interactions (Ao et al. 2013).

3.3 Turbulence

Turbulence may be another source for heating CMZ gas through dissipation of supersonic turbulence (Goldreich & Kwan 1974, Pan & Padoan 2009). Ao et al. (2013) shows that dissipation of turbulence can heat CMZ gas to $50-60$ K. Such a heating source would require an energy injection mechanism. One such mechanism is suggested to be tidal shearing due to differential Galactic rotation (Fleck 1980, Wilson et al. 1982, Güsten 1989). Acoustic gas instabilities (Kruijssen et al. 2014, Krumholz & Kruijssen 2015) may also be source for such turbulence.

Regardless of the length scale, molecular clouds in the GC have been found to have wider

turbulent line widths than those in the Galactic disk from a few tenths (Mills 2017, and references therein) to tens (Bally et al. 1987, Shetty et al. 2012) of parsecs. The linewidth of CMZ clouds typically range from $20 - 50\,\mathrm{km\,s^{-1}}$ (Bally et al. 1987, Lis & Menten 1998). An isothermal sound speed of $0.3 - 0.6\,\mathrm{km\,s^{-1}}$, and gas temperatures of $30 - 100\,\mathrm{K}$ imply that the turbulence is supersonic. The origin of the turbulent gas is not conclusively determined. One possibility may be tidal shearing to due Galactic rotation (Mills 2017, and references therein). Turbulence may be a contributing factor to the reduced star formation rates in the GC (Kruijssen et al. 2014).

3.4 Magnetic Fields

The presence of magnetic fields in the CMZ is indirectly revealed through a number of atomic nonthermal radio filaments (NTFs), which are relatively thin (fractions of parsecs wide and tens of parsecs long), and may present themselves in isolation or in bundles like those in a feature known as the Radio Arc (Yusef-Zadeh et al. 1986, Morris & Serabyn 1996). Radio polarization studies of these NTFs has brought insight to the direction of the local magnetic field, which are to be oriented parallel to these NTFs (Tsuboi et al. 1995). Although the orientation of these NTFs are often aligned together in bundles, there have been observations of randomly oriented nonthermal filaments, which suggest that strong fields may be a local phenomenon (LaRosa et al. 2000, Yusef-Zadeh et al. 2004). The strength of the magnetic field may be inferred from the morphology of these NTFs and the radio synchrotron emission (Morris 2014). By setting a lower bound on the strength of this field, it is suggested that the strength within the NTFs is on the order of several milligauss (Morris & Serabyn 1996, Yusef-Zadeh et al. 1996).

Additionally, the polarization of emission due to dust is an indicator of the magnetic field properties (Chuss et al. 2003, Novak et al. 2003). Zeeman observations have also been

conducted for several molecular species (Mills 2017, and references therein). Such magnetic field strengths in the CMZ are much stronger than in less extreme environments in the Milky Way. The average total strength of the magnetic field in our Galaxy is on the order of μG (Plante et al. 1995, Beck 2003, Crutcher et al. 2003). In the GC, the magnetic field strengths are tens of μG up to 1 mG in dense CMZ gas (Ferrière 2009). In the central few parsecs around the circumnuclear disk (CND), magnetic fields might have strengths of $2 - 4$ mG (Killeen et al. 1992, Plante et al. 1995, Crutcher et al. 2003).

3.5 Star Formation

The GC is clearly a physically different environment than the Galactic disk. Gas densities, temperatures, turbulence, and magnetic fields are comparatively more extreme. Such an environment is surprisingly quiescent in terms of star formation, since clouds with densities of 10^4 cm^3 in the Galactic disk should be actively forming stars (Mills 2017). It is possible that such extreme conditions, in particular of the turbulence, that inhibit star formation (Longmore et al. 2013, Kruijssen et al. 2014). Kruijssen et al. (2014) propose that high turbulent gas pressure increases the critical star formation density to several orders of magnitude more than in the Galactic disk, $\sim 10^8$ cm^{-3} compared to $\sim 10^4$ cm^{-3} (Mills 2017). Turbulence may be the most dominant inhibiting factor relative to other physical effects such as magnetic fields and radiation pressure.

Chapter 4

Magnetohydrodynamics

Molecular filaments are described by the physics of magnetohydrodynamics (MHD) since they involve the interactions between electromagnetic fields and conducting fluids. Such interactions are interdependent since fluid motion and magnetic fields influence each other, which causes large scale motions of the filament itself. MHD is closely related to plasma physics and much of the physical descriptions involved are similar. An important distinction between the two can be described by the relative frequency of the electromagnetic field involved and the frequency of the charged particle collisions in the medium (Jackson 1975). In the regime above the collision frequency, electrons and ions tend to separate due to the acceleration caused by the electromagnetic fields. This charge separation causes a restoring force, and in turn causes oscillations in charge density as this restoring force battles with the electromagnetic field in the medium. If these oscillations are at high frequency (relative to the collision frequency) then this is the regime of plasma waves and plasma physics. MHD waves are lower frequency oscillations where there is no charge separation with the motion of the fluid. It is approximated that the motions are described as a single fluid, compared to plasma physics where charge separation occurs and is described by individual particle motions or particle distribution functions. This lack of charge separation means that the

displacement current in Ampere's law can be neglected, and the mechanical motion can be described by density, velocity, and pressure, which is the regime of MHD.

4.1 Magnetohydrodynamic Equations

Generally, an electrically neutral, conducting fluid in the presence of electromagnetic fields is described by the fluid density $\rho(\boldsymbol{x}, t)$, velocity $\boldsymbol{v}(\boldsymbol{x}, t)$, and pressure $P(\boldsymbol{x}, t)$, where $\boldsymbol{x}$ is the position vector. The motion can be described by the continuity equation

$$0 = \frac{\partial \rho}{\partial t} + \boldsymbol{\nabla} \cdot (\rho \boldsymbol{v}), \tag{4.1}$$

and the momentum equation

$$\rho \frac{\partial \boldsymbol{v}}{\partial t} + \rho(\boldsymbol{v} \cdot \boldsymbol{\nabla})\boldsymbol{v} = -\boldsymbol{\nabla} P + \rho \boldsymbol{\nabla} \Phi + \frac{1}{c}(\boldsymbol{J} \times \boldsymbol{B}) + \boldsymbol{F_\nu}, \tag{4.2}$$

where c is the speed of light, Φ is the gravitational potential, $\boldsymbol{J}$ is the current density, $\boldsymbol{B}$ is the magnetic field, and $\boldsymbol{F_\nu} = \eta \boldsymbol{\nabla}^2 \boldsymbol{v}$ is the viscous force with viscosity coefficient η. An ideal fluid is assumed such that the viscous force is negligible. The gravitational potential appears in the momentum equation (Equation 4.2 as Φ, which is described by Poisson's Equation

$$\nabla^2 \Phi = 4\pi G \rho. \tag{4.3}$$

The gravitational field is defined as $g := -\nabla \Phi$. The left-hand-side of the momentum Equation (4.2) contains the convective derivative

$$\frac{\partial}{\partial t} + \boldsymbol{v} \cdot \boldsymbol{\nabla}. \tag{4.4}$$

In cylindrical polar coordinates $(\hat{r}, \hat{\phi}, \hat{z})$, the three components of the convective derivative

are written as (Landau & Lifshitz 1987)

$$\frac{\partial v_r}{\partial t} + (\boldsymbol{v} \cdot \boldsymbol{\nabla}) v_r - \frac{v_\phi^2}{r}, \tag{4.5a}$$

$$\frac{\partial v_\phi}{\partial t} + (\boldsymbol{v} \cdot \boldsymbol{\nabla}) v_\phi - \frac{v_r v_\phi}{r}, \tag{4.5b}$$

and

$$\frac{\partial v_z}{\partial t} + (\boldsymbol{v} \cdot \boldsymbol{\nabla}) v_z. \tag{4.5c}$$

In addition to the equations of hydrodynamics (Equations 4.1 and 4.2), the effects of electromagnetics are taken into account via Faraday's Law

$$\boldsymbol{\nabla} \times \boldsymbol{E} = -\frac{1}{c}\frac{\partial \boldsymbol{B}}{\partial t}, \tag{4.6a}$$

and Ampére's Law (neglecting the displacement current)

$$\boldsymbol{\nabla} \times \boldsymbol{B} = \frac{4\pi}{c}\boldsymbol{J}, \tag{4.6b}$$

where $\boldsymbol{E}$ is the electric field. The current density $\boldsymbol{J}$ is described via Ohm's Law

$$\boldsymbol{J} = \kappa\left(\boldsymbol{E} + \frac{\boldsymbol{v}}{c} \times \boldsymbol{B}\right), \tag{4.7}$$

where κ is the electrical conductivity. By eliminating $\boldsymbol{E}$ in Faraday's Law (Equation 4.6a), and then using Ampére's Law (Equation 4.6b) to substitute for $\boldsymbol{J}$, Faraday's Law becomes

$$\frac{\partial \boldsymbol{B}}{\partial t} = \boldsymbol{\nabla} \times (\boldsymbol{v} \times \boldsymbol{B}) + \eta_e \nabla^2 \boldsymbol{B}, \tag{4.8}$$

where the *electrical resistivity* (or *magnetic diffusivity*) is given by

$$\eta_e = \frac{c^2}{4\pi\kappa}. \tag{4.9}$$

The second term on the right hand side of Equation 4.8 describes the diffusion and decay of the magnetic field due to *Ohmic dissipation*. The *magnetic Reynolds number* is given by the scales of the first and second terms on the right hand side of Equation 4.8 such that

$$R_{em} = \frac{vL}{\eta_e} \tag{4.10}$$

where L is a characteristic length and v is a characteristic velocity of the magnetic field. For $R_{em} \gg 1$, the effects of Ohmic dissipation are negligible. For a perfectly conducting medium ($\kappa \to \infty$), Equation 4.8 can then be written as

$$\frac{\partial \boldsymbol{B}}{\partial t} = \boldsymbol{\nabla} \times (\boldsymbol{v} \times \boldsymbol{B}). \tag{4.11}$$

Further simplification can be made by substituting $\boldsymbol{J}$ from Ampére's Law into the momentum equation (Equation 4.2) so that

$$\rho \frac{\partial \boldsymbol{v}}{\partial t} + \rho(\boldsymbol{v} \cdot \boldsymbol{\nabla})\boldsymbol{v} = -\boldsymbol{\nabla} P + \rho \boldsymbol{\nabla} \Phi - \frac{1}{4\pi} \boldsymbol{B} \times (\boldsymbol{\nabla} \times \boldsymbol{B}). \tag{4.12}$$

To complete the set of magnetohydrodynamic equations, an equation of state must be included. For this work, the effective pressure of the filament is related to its density by an isothermal equation of state described by

$$P = \sigma^2 \rho, \tag{4.13}$$

where σ is the total velocity dispersion including thermal and nonthermal components, and is constant within the filament. Equations 4.1, 4.11, 4.12,and 4.13 constitute the magnetohydrodynamic equations for an isothermal, compressible, perfectly conducting fluid. Collec-

tively, these equations are referred to as the *MHD equations*. These equations govern the structure and dynamics of molecular tornadoes (see Chapter 7). In Chapter 8 the assumption of isothermality is relaxed and the polytropic and logatropic equations of state are also considered.

4.2 Flux-Freezing

There is more physical insight to be gained from the equation of magnetohydrodynamics that are relevant to the behaviour of molecular tornadoes. If perfect conductivity is not assumed, then a characteristic time scale corresponding to the diffusion of the magnetic field can be obtained from the scales of Faraday's Law (Equation 4.8) as

$$\tau = \frac{4\pi\kappa L^2}{c^2}, \tag{4.14}$$

where L is a length scale of $\boldsymbol{B}$. It is obvious that by assuming a perfectly conducting fluid, then the relevant time scales for magnetic diffusion are not of concern in such a model. In relatively shorter time scales, Equation 4.11 is sufficient in describing the relationship between the magnetic field evolution and motion of the fluid. This is a phenomenon known as *flux-freezing* when this characteristic time scale is much larger than the kinematic timescale τ_{ff} (Equation 2.27). Flux-freezing describes how the flux through a loop moving with the local fluid motion remains constant through time. This can be thought of as having the magnetic field lines locked in with the fluid motion. Flux-freezing has been used to describe the nonequilibrium deformations of initially uniform clouds to cores (Franzmann & Fiege 2017). The flux-freezing assumption is used throughout the models explored in this work as a flux-to-mass ratio (see Chapter 7), and has also been used in the work of Fiege & Pudritz (2000*a*,*b*).

4.3 Ambipolar Diffusion

Ambipolar diffusion describes the movement of mass across magnetic field lines constituted by neutral gas. Even when gas is magnetically supported, it can still condense under self-gravity due to this process of ion-neutral drift. In other words, it can lower M_Φ (see Section 2.10) or equivalently, increase the local mass-to-flux ratio toward this critical value. Ambipolar diffusion is described by first considering the relative drift velocity between neutrals and ions (denoted with subscripts n and i, respectively) $\boldsymbol{v}_D = \boldsymbol{v}_i - \boldsymbol{v}_n$ in the presence of a magnetic field $\boldsymbol{B}$. The balance between the Lorentz force and ion-neutral drag is then described by

$$\frac{1}{4\pi}(\boldsymbol{\nabla} \times \boldsymbol{B}) \times \boldsymbol{B} = \alpha \rho_i \rho_n (\boldsymbol{v}_i - \boldsymbol{v}_n), \tag{4.15}$$

where ρ_i and ρ_n are the ion and neutral densities. The coupling coefficient is given by (Smith & Mac Low 1997)

$$\alpha = \langle \sigma v \rangle / (m_i + m_n) \approx 9.2 \times 10^{13}\,\mathrm{cm^3\,s^{-1}\,g^{-1}}, \tag{4.16}$$

where m_i and m_n are the mean mass per particle for the ions and neutrals, and σ is the ion-neutral cross-section. A typical time scale can be derived by considering the drift across a cylinder of radius R such that $\tau_{AD} = R/v_D$. The Lorentz force is then approximately $B^2/4\pi R$ and v_D can be found from Equation 4.15. Thus, the *ambipolar diffusion timescale* is described as

$$\begin{aligned} \tau_{AD} &= \frac{4\pi\alpha\rho_i\rho_n R^2}{B^2} \\ &= (25\,\mathrm{Myr})\left(\frac{B}{3\,\mu\mathrm{G}}\right)^{-2}\left(\frac{n_n}{10^2\,\mathrm{cm^{-3}}}\right)^2\left(\frac{R}{1\,\mathrm{pc}}\right)^2\left(\frac{x}{10^{-6}}\right), \end{aligned} \tag{4.17}$$

(Mac Low & Klessen 2004) where x is the ionization fraction. The ionization fraction is usually needs to be quite small for τ_{AD} to be relevant on astrophysical timescales. For example, cosmic ray ionization rates calculated by Elmegreen (1979) for dense cloud cores

suggested that the ionization fraction is approximately

$$x \approx (5 \times 10^{-8}) \left(\frac{n}{10^5 \, \mathrm{cm}^{-3}} \right). \tag{4.18}$$

The ambipolar diffusion timescale can be more than 10 times larger than the dynamical time scale τ_{ff} (Equation 2.27) of the system, which may explain low star formation rates by magnetic regulation observed in normal galaxies, and long lifetimes of molecular clouds (Blitz & Shu 1980, Solomon et al. 1987).

4.4 Alfvén Waves

As mentioned in the beginning of this chapter, the dynamics between magnetic fields and the charge carriers in the fluid can produce magnetohydrodynamic waves or perturbations. Magnetic fields provide a "tension" that restores fluid perturbations to the field lines resulting in transverse waves known as Alfvén waves. Since these are purely MHD waves, it suffices to perturb a static, non-self-gravitating medium, with constant density and uniform magnetic field. The equilibrium solution (denoted with a subscript 0) is subject to perturbations (denoted with a subscript 1) of the general Fourier wave form

$$f_1^* = f_1(\boldsymbol{x}) e^{i(\boldsymbol{k} \cdot \boldsymbol{x} - \omega t)}, \tag{4.19}$$

where f denotes a general perturbed quantity, $\boldsymbol{k} = 2\pi/\lambda \, \hat{n}$ is the wave vector, and ω is the angular frequency. Thus, the perturbed quantities are

$$\boldsymbol{B} = \boldsymbol{B}_0 + \boldsymbol{B}_1(\boldsymbol{x}, t), \tag{4.20a}$$

$$\rho = \rho_0 + \rho_1(\boldsymbol{x}, t), \tag{4.20b}$$

and

$$\boldsymbol{v} = \boldsymbol{v}_1(\boldsymbol{x}, t), \tag{4.20c}$$

From linearizing (keeping up to first order terms) the MHD equations then,

$$\partial_t \rho_1^* + \rho_0 \boldsymbol{\nabla} \cdot \boldsymbol{v}_1^* = 0, \tag{4.21a}$$

$$\rho_0 \partial_t \boldsymbol{v}_1^* = -\sigma^2 \boldsymbol{\nabla} \rho_1^* - \frac{1}{4\pi} \boldsymbol{B_0} \times (\boldsymbol{\nabla} \times \boldsymbol{B}_1^*), \tag{4.21b}$$

and

$$\partial_t \boldsymbol{B}_1^* = \boldsymbol{\nabla} \times (\boldsymbol{v}_1^* \times \boldsymbol{B_0}). \tag{4.21c}$$

Taking the time derivative of Equation 4.21b, substituting Equations 4.21a and 4.21c, and then dividing by ρ_0 yields

$$\partial_t^2 \boldsymbol{v}_1^* = -\sigma^2 \boldsymbol{\nabla}(\boldsymbol{\nabla} \cdot \boldsymbol{v}_1^*) - \frac{\boldsymbol{B}_0}{4\pi\rho_0} \times \boldsymbol{\nabla} \times [\boldsymbol{\nabla} \times (\boldsymbol{v}_1^* \times \boldsymbol{B}_0)]. \tag{4.22}$$

It is useful to define a quantity known as the Alfvén speed

$$v_A := \frac{B_0}{\sqrt{4\pi\rho_0}} \tag{4.23}$$

to use in Eq. 4.22, so that it becomes

$$\partial_t^2 \boldsymbol{v}_1^* = -\sigma^2 \boldsymbol{\nabla}(\boldsymbol{\nabla} \cdot \boldsymbol{v}_t^*) - \boldsymbol{v}_A \times \boldsymbol{\nabla} \times [\boldsymbol{\nabla} \times (\boldsymbol{v}_1^* \times \boldsymbol{v}_A)]. \tag{4.24}$$

Equation 4.23 describes the propagation speed at which the perturbation travels along magnetic field lines, where Equation 4.24 is the MHD wave equation. The Alfvén waves traverse in the direction of the magnetic field lines. For example, a cylindrical filament with an axial magnetic field (along the $\hat{z}$ direction), the direction of propagation would be along the axis

of the filament. Alfvén waves are most relevant to the torsional Alfvén waves in Chapter 7, though Equation 4.24 also permits magnetosonic solutions.

Chapter 5

Molecular Filaments

5.1 Filaments Threaded by Helical Magnetic Fields

Fiege & Pudritz (2000*a*) explain many important theoretical and numerical methods for understanding molecular filaments. Prior to this work, the detail of spherical molecular clouds had been well studied, but cylindrical molecular clouds had not been as thoroughly studied. Such a study was warranted since many molecular clouds are often filamentary in nature and host star formation. Fiege & Pudritz (2000*a*) conducted a virial analysis to explore global properties of molecular filaments, which were observationally constrained. They built exact numerical MHD models from the space of observationally constrained filaments and truncated by realistic external pressure to study the internal structure of filaments in equilibrium. An isothermal equation of state as well as a logatropic equation of state were used in their analysis.

The scalar virial theorem was employed to study the relationship between gravity, external pressure, turbulence, and magnetic fields. A useful form of the virial equation was written as

$$\frac{P_S}{\langle P \rangle} = 1 - \frac{m}{m_{vir}}\left(1 - \frac{\mathcal{M}}{|\mathcal{W}|}\right), \tag{5.1}$$

where S denoted surface terms such that P_S was the surface (external) pressure, $\langle P \rangle$ was the average internal pressure, m was the linear mass, and m_{vir} was the virial linear mass. Script notation denoted quantities per unit length such that $\mathcal{M}$ and $\mathcal{K}$ were the total magnetic and kinetic energies per unit length, respectively. These quantities were explicitly written in Fiege & Pudritz (2000*a*). Alternatively, Equation 5.1 was written explicitly in terms of the magnetic pressures as

$$\frac{P_S}{\langle P \rangle} = 1 - \frac{m}{m_{vir}} + \left(\frac{\langle P_{mag} \rangle - P_{mag,S}}{\langle P \rangle} \right), \tag{5.2}$$

which was useful in showing that the poloidal magnetic field supports the cloud via $\langle P_{mag} \rangle$, and that the toroidal magnetic field only contributed to the surface magnetic pressure $P_{mag,S}$ by a pinching effect.

The virial relation of Equation 5.1 was most easily understood by considering the case of unmagnetized filaments $\mathcal{M} = 0$. It was easily seen that in order for solutions to satisfy the virial relation, $m < m_{vir}$. If $m > m_{vir}$ then no solutions exist. As $m \to m_{vir}$ then, $P_S/\langle P \rangle \to 0$. Physically, this meant that the addition of mass to an already critical filament would cause an increase in self-gravity such that it would transition out of equilibrium, initiating radial collapse. Thus, m_{vir} was designated as a critical mass per unit length separating the domain where solutions exist from the domain where solutions do not exist.

For a magnetized filament, the critical mass per unit length is defined and denoted as m_{mag} when $P_S/\langle P \rangle \to 0$ in the virial relation (Equation 5.1) such that

$$m_{mag} = \frac{m_{vir}}{1 - \mathcal{M}/|\mathcal{W}|}. \tag{5.3}$$

The sign of $\mathcal{M}$ indicates the dominant component of the helical magnetic field; $\mathcal{M} < 0$ means the toroidal component is dominant while $\mathcal{M} > 0$ denotes a dominant poloidal field (Fiege & Pudritz 2000*a*). Thus, is it easy to interpret the physical significance of Equation 5.3. A

dominant poloidal field supports the filament allowing for larger m_{mag}, while the toroidal field pinches the filament and lowers m_{mag} relative to m_{vir}. The absence of magnetic fields ($\mathcal{M} = 0$) recovers the critical mass per unit length $m_{mag} = m_{vir}$ as expected.

Fiege & Pudritz (2000*a*) used the virial equation (Equation 5.1) as a method to determine that toroidal fields dominate the field ($\mathcal{M} < 0$) in real molecular filaments; thus the field must be helical. Observations gave reasonable constraints to the terms m/m_{vir} and $P_S/\langle P \rangle$, allowing $\mathcal{M}/|\mathcal{W}|$ to be estimated. Based on the global properties described by the virial theorem, Fiege & Pudritz (2000*a*) found that helical magnetic fields were necessary for a sample of observed molecular filaments to maintain virial equilibrium as shown in Figure 5.1 (from Fiege & Pudritz (2000*a*)). This was because molecular filaments exhibit high turbulence, which could not be confined solely by external pressure and self-gravity alone. Additional magnetic confinement was needed to assist in maintaining the equilibrium structure regardless of the equation of state.

Having analyzed the global properties of molecular filaments, exact numerical MHD models were then explored to study the internal equilibrium structure. The Fiege & Pudritz (2000*a*) model assumes constant poloidal and toroidal flux-to-mass ratios to describe the magnetic fields as explained in Fiege & Pudritz (2000*a*) and schematically illustrated in Figure 5.2. Via the MHD equations (see Section 4.1), they constructed models of molecular filaments with external pressure truncation, helical magnetic fields, and the isothermal and logatropic equations of state.

A known analytic solution was used as comparison to these exact MHD models. Ostriker (1964) found that nonrotating, unmagnetized, non-pressure-truncated cylinders followed radial density profiles described by

$$\rho = \frac{\rho_0}{\left(1 + \frac{r^2}{8r_0^2}\right)^2}, \tag{5.4}$$

which follow steep $\sim r^{-4}$ profiles at large radii. This Ostriker solution was used as a com-

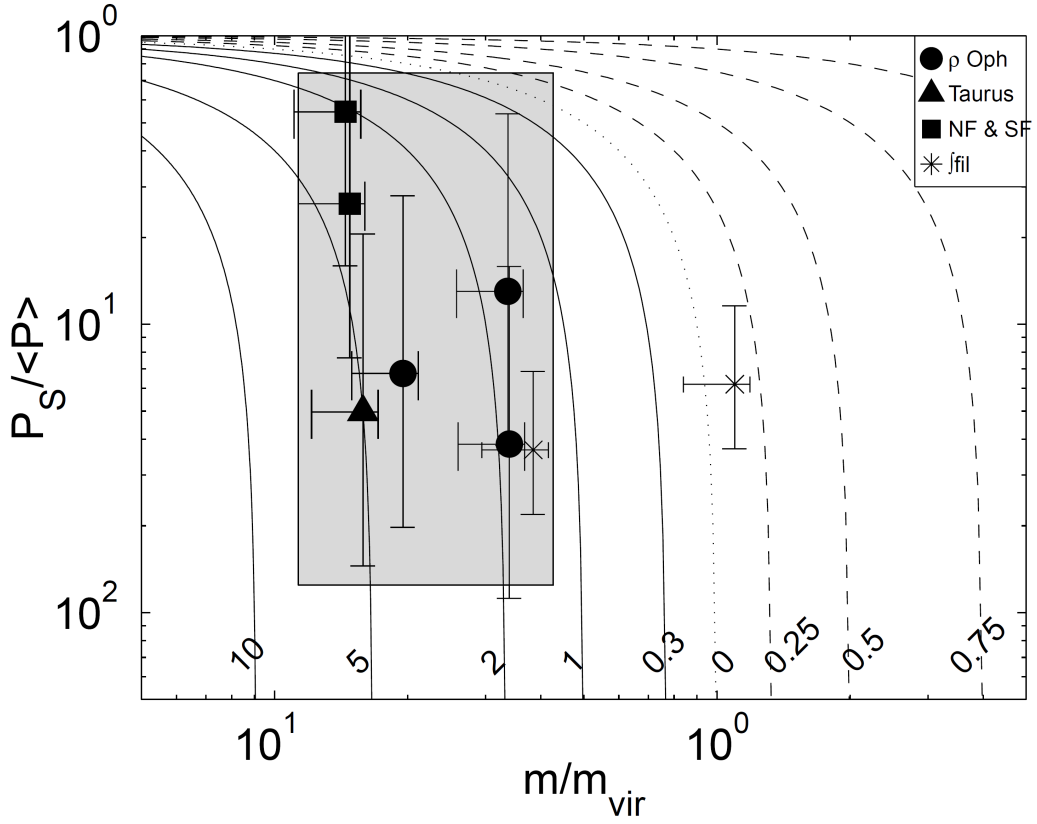

Figure 5.1: Fiege & Pudritz (2000*a*) used the virial relation of Equation 5.1 to constrain their numerical MHD models by observations of real molecular filaments. Various molecular filaments are plotted on this diagram which indicate the presence of helical fields. Curves indicate constant $\mathcal{M}/|\mathcal{W}|$ values. Solid lines denote toroidally dominated ($\mathcal{M} < 0$) fields. Dashed lines denote poloidally dominated ($\mathcal{M} > 0$) fields. Dotted lines denote unmagnetized filaments and combinations of magnetic fields with no net affect on the internal filament structure. Exact data of the sampled molecular filaments are provided in Fiege & Pudritz (2000*a*). Figure credit: Figure 1, Helical fields and filamentary molecular clouds - I, J. D. Fiege and R. E. Pudritz, *Monthly Notices of the Royal Astronomical Society*, Volume 11, Issue 1, Fiege & Pudritz (2000*a*).

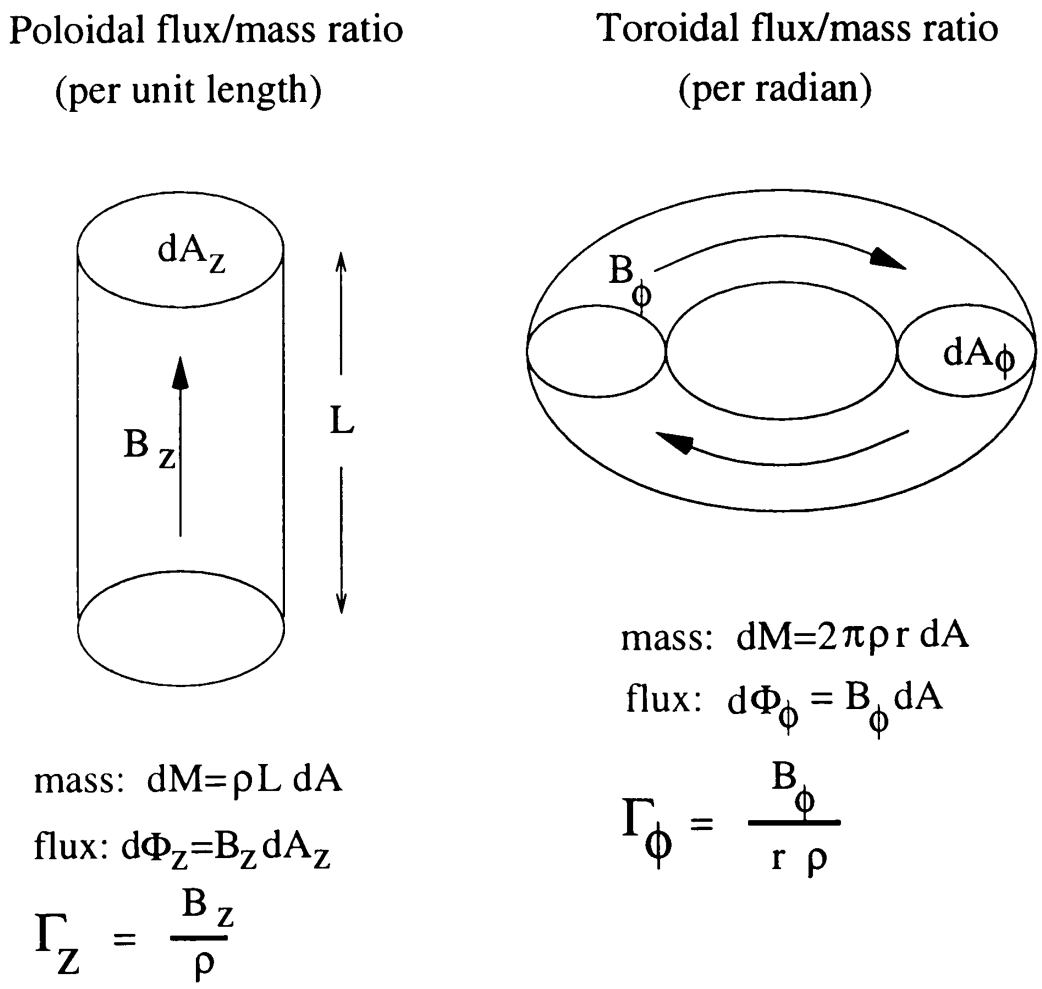

Figure 5.2: Toroidal and poloidal flux-to-mass ratios. These flux-to-mass ratios were considered as constant in Fiege & Pudritz (2000*a*), but can be functions of magnetic flux in general. Figure credit: Figure 2, Helical fields and filamentary molecular clouds - I, J. D. Fiege and R. E. Pudritz, *Monthly Notices of the Royal Astronomical Society*, Volume 11, Issue 1, Fiege & Pudritz (2000*a*).

parison to the exact numerical MHD solutions in order to understand what the effects of magnetic fields were.

Isothermal models were found to have $m \to m_{vir}$ asymptotically as expected from the virial analysis, since no equilibrium solutions existed with $m > m_{vir}$. Purely poloidal magnetic fields radially extended the filament core, and it was noted that the density in such solutions tends to drop off steeply in the outer envelope. These density profiles were steeper at large r than the Ostriker solution's r^{-4} behaviour. Purely toroidal magnetic fields, on the other hand, tended to radially extend the core, which then gradually fell with increasing radius, following a more shallow asymptotic power law. Solutions with purely toroidal magnetic fields are non-physical because such a field cannot be formed by any amount of twisting the magnetic field. By including flux-freezing, the field topology does not change.

Pressure truncation was modeled by a concentration parameter C, which was dependent on the filament radius R_S scaled by its core radius r_0. A Monte Carlo search of the Γ_z, Γ_ϕ, C space proceeded to create filaments modeled by random combinations of these parameters. These models were then constrained by the virial parameters m/m_{vir}, $P_S/\langle P \rangle$, and the ratio of magnetic to kinetic energy densities X. The ratio $X = M/K$ was of order unity as Fiege & Pudritz (2000*a*) argued by observations which indicated the magnetic and kinetic energy densities were in approximate equipartition (Myers & Goodman 1988*a*,*b*). This meant that $X = \langle v_A^2 \rangle / 3\langle \sigma^2 \rangle \approx \mathcal{O}[1]$ for self-gravitating magnetized clouds supported by Alfvénic turbulence. The main outcomes of these constrained models from the Monte Carlo search were that Γ_z was better constrained for both equations of state than Γ_ϕ, and the constrained range of both Γ_z and Γ_ϕ were larger for the logatropic versus isothermal equations of state.

Observationally constrained isothermal filaments were generally axially dominated by poloidal magnetic fields while the outer envelope was dominated by toroidal magnetic fields. Such isothermal density profiles scaled as $\rho \sim r^{-1.8}$ to r^{-2}. Constrained filaments following a logatropic equation of state exhibited a wider range in the power law index as the density

scaled as $\rho \sim r^{-1}$ to $r^{-1.8}$. The density of these filaments fall off more rapidly in their core than their outer envelope.

5.2 B211 in the Taurus Molecular Cloud

Palmeirim et al. (2013) presented their observations from the Herschel Gould Belt survey (HGBS) of the B211/L1495 region of the Taurus molecular cloud (TMC). B211 is a star forming filament with features known as "striations" that extend perpendicular to B211. Typical ISM pressures are in the range $P_S \sim 2 - 5 \times 10^4\,\mathrm{K\,cm^{-3}}$ (Palmeirim et al. 2013, and references therein). Stars form in the densest part of filaments when their mass per unit length (m) exceeds the critical value as

$$m > m_{crit} = \frac{2\sigma^2}{G}. \tag{5.5}$$

The B211 filament exceeds this critical line mass and so it is gravitationally unstable, whereas surrounding striations do not exceed the critical line mass.

Polarization vectors aligned perpendicular to the length of the filament, and were parallel to the length of the striations. They studied the column density profile of the B211 filament and found that the density behaved as $\rho \sim r^{-2.0\pm0.4}$ at large radii based on a fit to the Plummer density profile. The Plummer profile features an inner dense, flat portion prior to a power-law behavior at large radii described by

$$\rho_P = \frac{\rho_c}{[1 + (r/R_{flat})^2]}^{p/2}, \tag{5.6}$$

(Palmeirim et al. 2013, and references therein) where ρ_c is the central filament density, R_{flat} is the radius of the flat portion, and p is the power-law exponent. The radial density behavior is notably more shallow than the isothermal, non-magnetized, nonrotating filaments found

by Ostriker (1964). Such behaviour of the density profile is more similar to the behaviour of the Fiege & Pudritz (2000*a*) model for isothermal, nonrotating, molecular filaments threaded by helical magnetic fields.

An analysis of the dust temperature profile showed a dip toward the filament centre, which suggested that B211 is not strictly isothermal. A better model to account for the dust temperature profile was that of a polytropic EOS $P \propto \rho^{\gamma}, \gamma \leq 1$ described by Kawachi & Hanawa (1998) such that the outer density profile of a collapsing cylinder approaches the power law $\rho \propto r^{-\frac{2}{2-\gamma}}$. Palmeirim et al. (2013) estimated the polytropic index γ, and best fit to the dust temperature profile by $T(r) \propto \rho_P(r)^{\gamma-1}$. They found a best fit of $\gamma = 0.97 \pm 0.01 < 1$, which corresponded to $\rho \propto r^{-1.96 \pm 0.02}$ for not-strictly isothermal cylinders.

An estimate of B211's critical line mass is approximately $m_{crit} \approx 54\,\mathrm{M}_{\odot}\,\mathrm{pc}^{-1}$, which is the condition where the filament is unstable to radial contraction and fragments into cores. Observations confirm the existence of prestellar cores and protostars along B211's length, so its linear mass must be in excess of m_{crit}.

Polarization of background stars suggest that the Taurus structure is linked with the magnetic field. By the Chandrasekhar-Fermi method, the magnetic field strength was estimated at $B \sim 25\,\mu$G in the B211 region, and contains magnetically subcritical striations.

Chapter 6

Virial Analysis for Rotating, Magnetized Filaments

Fiege & Pudritz (2000*a*) derives a useful form the scalar virial equation for pressure-truncated, stationary filamentary cloud threaded by helical magnetic fields. In the case of molecular tornadoes, the addition of the rotational energy component modifies this analysis. As a comparison to the virial equation derived by Fiege & Pudritz (2000*a*), a similar analysis is performed to better understand the effect of rotation on filaments. A similar notation to Fiege & Pudritz (2000*a*) is used in this analysis to preserve continuity; that is, quantities with the subscript S denote quantities at the filament surface, while those in calligraphic notation are quantities per-unit-length.

The scalar virial equilibrium equation is given in general by

$$0 = 2\mathcal{K} + \mathcal{W} + \mathcal{M}, \tag{6.1}$$

where $\mathcal{K}$ is the total kinetic energy per-unit-length, $\mathcal{W}$ is the gravitational energy per-unit-length, and $\mathcal{M}$ is the total sum of the magnetic quantities per-unit-length. Molecular tornadoes are non-self-gravitating (Sofue 2007), and this is demonstrated in more detail later

in this work (see Section 7.2.3). For a rotating filament where self-gravity is negligible, Equation 6.1 becomes

$$0 = 2\mathcal{K} + \mathcal{M}. \tag{6.2}$$

If $\mathcal{K}$ includes the turbulent, thermal, and rotational kinetic energies then the total kinetic energy is given by

$$\begin{aligned} \mathcal{K} &= \mathcal{K}_{in} + \mathcal{K}_{out} + \mathcal{K}_{rot} \\ &= \frac{3}{2} m\sigma^2 - \frac{3}{2} P_S \mathcal{V} + \frac{1}{2} \mathcal{I}\Omega^2, \end{aligned} \tag{6.3}$$

where solid body rotation is assumed. The kinetic energy for a rotating, uniform cylinder is described by

$$\begin{aligned} \mathcal{K}_{rot} &= \frac{1}{2} \mathcal{I}\Omega^2 \\ &= \frac{\alpha}{4} m v_\phi^2, \end{aligned} \tag{6.4}$$

where $\mathcal{I}$ is the rotational inertia of a uniform cylinder spinning along its long axis, Ω is the angular frequency of rotation, m is the mass per-unit-length, the rotational speed at the cylinder surface is given by v_ϕ, and α is a constant of order unity. The total kinetic energy (Equation 6.3), including the negative term for surface pressure, can be rewritten as

$$\mathcal{K} = m\left(\frac{3}{2}\sigma^2 + \frac{\alpha}{4} v_\phi^2\right) - \frac{3}{2} P_S \mathcal{V}. \tag{6.5}$$

With the kinetic energy written this way, the non-self-gravitating virial equation (Equation 6.2) becomes

$$0 = m\left(3\sigma^2 + \frac{\alpha}{2} v_\phi^2\right) - 3P_S \mathcal{V} + \mathcal{M}, \tag{6.6}$$

or

$$
\begin{aligned}
0 &= 3(\langle P\rangle - P_S)\mathcal{V} + \frac{\alpha}{2} m v_\phi^2 + \mathcal{M} \\
&= 2(\mathcal{K}_{in} - \mathcal{K}_{out}) + \mathcal{K}_{rot} + \mathcal{M},
\end{aligned}
\tag{6.7}
$$

where the terms with angled brackets denote quantities within the filament such that $\langle P\rangle V = \langle \rho\sigma^2\rangle V = \langle M\sigma^2\rangle$ (Fiege & Pudritz 2000*a*). Additionally, the kinetic energy components $\mathcal{K}_{out} = (3/2)P_S\mathcal{V}$, $\mathcal{K}_{in} = (3/2)\langle P\rangle\mathcal{V}$, and the rotational kinetic energy (Equation 6.4) were used. By defining a so-called "rotational pressure"

$$
P_{rot} \equiv \frac{\alpha}{6}\langle\rho\rangle v_\phi^2 \tag{6.8}
$$

then Equation 6.4 becomes

$$
\mathcal{K}_{rot} = \frac{3}{2} P_{rot}\mathcal{V}. \tag{6.9}
$$

After some algebraic manipulation, the virial equation can then be written as

$$
\frac{P_S}{\langle P\rangle + P_{rot}} = 1 + \frac{\mathcal{M}}{2(\mathcal{K}_{in} + \mathcal{K}_{rot})} = \frac{\mathcal{K}_{out}}{\mathcal{K}_{in} + \mathcal{K}_{rot}}, \tag{6.10}
$$

which is a useful form for understanding the properties of molecular tornadoes.

In the models that are investigated in Chapter 7, self-gravity is maintained to investigate how prevalent it is relevant to the other virial terms involved. Thus, a different virial formulation is used for analysis, which is useful to determine which component of the helical magnetic field is dominant (see Section 7.2.3). By keeping self-gravity in the virial equation, it can be expressed as

$$
\frac{\mathcal{M}}{|\mathcal{W}|} = -2\left(\frac{\mathcal{K}_{rot}}{|\mathcal{W}|} + \frac{\mathcal{K}_\sigma}{|\mathcal{W}|} - \frac{|\mathcal{K}_P|}{|\mathcal{W}|}\right) - 1, \tag{6.11}
$$

where rotation term in both Equations 6.10 and 6.11 are denoted by $\mathcal{K}_{rot}$, while $\mathcal{K}_{in} = \mathcal{K}_\sigma$, and $\mathcal{K}_{out} = \mathcal{K}_P$. Equation 6.11 explicitly demonstrates the dominant magnetic field

component such that $\mathcal{M}/|\mathcal{W}| < 0$ is toroidally dominant, and $\mathcal{M}/|\mathcal{W}| > 0$ is poloidally dominated (Fiege & Pudritz 2000*a*). After an observationally constrained virial analysis in Chapter 7 however, Equation 6.10 is recovered and expressed as

$$\frac{|\mathcal{K}_P|}{\mathcal{M}} = \frac{\mathcal{K}_{rot} + \mathcal{K}_\sigma}{\mathcal{M}} + \frac{1}{2}, \tag{6.12}$$

so the dominant magnetic field component is more obviously seen. Equation 6.11 is easily comparable with the virial relation from Fiege & Pudritz (2000*a*), whereas Equation 6.12 is a more suitable description for molecular tornadoes where self-gravity is unimportant.

Chapter 7

Magnetohydrodynamic Models of Molecular Tornadoes

This chapter is a modified version of "Magnetohydrodynamic Models of Molecular Tornadoes" by Au K. and Fiege J.D. published in *The Astrophysical Journal* on July 11$^{\text{th}}$, 2017. In subsequent chapters the references to this chapter and the citation Au & Fiege (2017) are used interchangeably.

Abstract

Recent observations near the Galactic Centre have found several molecular filaments displaying striking helically-wound morphology, which are collectively known as "molecular tornadoes." We investigate the equilibrium structure of these molecular tornadoes by formulating a magnetohydrodynamic model of a rotating, helically magnetized filament. A special analytical solution is derived where centrifugal forces balance exactly with toroidal magnetic stress. From the physics of torsional Alfvén waves, we derive a constraint that links the toroidal flux-to-mass ratio and the pitch angle of the helical field to the rotation laws, which we find to be an important component in describing molecular tornado structure.

The models are compared to the Ostriker solution for isothermal, non-magnetic, nonrotating filaments. We find that neither the analytic model nor the Alfvén wave model suffer from unphysical density inversions noted by other authors. A Monte Carlo exploration of our parameter space is constrained by observational measurements of the Pigtail Molecular Cloud (Pigtail), Double Helix Nebula (DHN), and Galactic Centre molecular Tornado (GCT). Observable properties such as the velocity dispersion, filament radius, linear mass, and surface pressure can be used to derive three dimensionless constraints for our dimensionless models of these three objects. A virial analysis of these constrained models is studied for these three molecular tornadoes. We find that self-gravity is relatively unimportant, whereas magnetic fields, and external pressure play a dominant role in the confinement and equilibrium radial structure of these objects.

7.1 Introduction

The Pigtail Molecular Cloud (Pigtail) is an intriguing molecular filament that resides close to the Galactic midplane within the Central Molecular Zone (CMZ). It exhibits a helical structure that was first noticed by Matsumura et al. (2012) from CO $J = 1 - 0$ data observed by the Nobeyama Radio Observatory 45 m radio telescope. The Pigtail helix has a $\sim$ 15 pc pitch that traces at least two rounds of a helix in ^{12}CO, extending to an angular size of $\sim 0.15^\circ \times 0.15^\circ$ and corresponding to a spatial size of $\sim 20 \times 20\,\mathrm{pc}^2$ with a mass of $(2-6) \times 10^5\,M_\odot$ (Matsumura et al. 2012).

The proposed mechanism that triggers the helical morphology of the Pigtail is similar to that of two other molecular tornadoes known as the "Double Helix Nebula" (DHN) and the "Galactic Center molecular Tornado" (GCT) (Matsumura et al. 2012). A vertical magnetic tube that extends into the Galactic halo is twisted into its helical form. The driver of this twisting motion is hypothesized to be due to the shearing of inner (x_1) and outer (x_2) cloud

orbits. In this scenario, the vertical magnetic tube is caught between two cloud orbits with different velocities, and the velocity shear twists the magnetic tube. With enough twisting, this torsional Alfvén wave causes the magnetic tube to undergo a kink ($m = 1$) instability (Jackson 1975, Matsumura et al. 2012), which winds it into its observed corkscrew-like morphology. Matsumura et al. (2012) estimate the Pigtail's magnetic field to be on the order of 1 mG. Matsumura et al. (2012) support this formation scenario due to observations of the SiO/^{13}CO ratio that are indicative of the shock between the cloud orbit interaction and of other molecular gas.

Another molecular tornado was found approximately 100 pc from the Galactic Centre (GC) in the infrared by the Spitzer Space Telescope by Morris et al. (2006). They called it the "Double Helix Nebula" (DHN) because of its apparently intertwined double helix structure. The DHN is observed to wind at least 1.25 complete rounds that stretch approximately 25 pc in length with its long axis parallel the Galaxy's rotation axis. Morris et al. (2006) propose that the DHN is a magnetohydrodynamic (MHD) torsional Alfvén wave propagating away from the Galactic disk, driven by the circumnuclear disk (CND). Morris et al. (2006) estimated the magnetic field strength to be $B = 0.1-1$ mG, depending on the assumed proton density in the region. Unlike the Pigtail Molecular Cloud, the presence of two intertwining strands of the DHN suggest that the twisted field due to the torsional wave has triggered an $m = 2$ instability (Jackson 1975, Morris et al. 2006).

Sofue (2007) first reported on the GCT, which was also observed in CO with the Nobeyama Radio Observatory. The GCT extends 170 pc vertically from the Galactic plane and was measured to rotate at a velocity of $\sim 30\,\mathrm{km\,s^{-1}}$ with an estimated mass of $M \sim 1.2 \times 10^6\,M_\odot$. Sofue (2007) note that the GCT, or at least part of it, consists of two helical strands like the DHN. Interestingly, the authors suggest that the GCT is not gravitationally bound, but that there must be an external force or pressure to keep the filament bound. They suggest that the most plausible mechanism confining the GCT against centrifugal force is the magnetic

tension due to a toroidally wrapped field with $B \sim 0.4\,\mathrm{mG}$. The GCT was proposed to arise from the same mechanism as that of the DHN – that a torsional Alfvén wave, driven by the epicyclic rotation of a cloud orbiting the Galactic Centre, twists a magnetic flux tube, which then undergoes an $m = 2$ MHD instability (Sofue 2007).

There has not yet been a detailed theoretical/numerical study on the structure of molecular tornadoes. In this paper, we consider the equilibrium structure of uniformly and differentially rotating, isothermal, self-gravitating and non-self-gravitating, cylinders threaded by somewhat general helical magnetic fields, analogous to the stationary filaments studied by Fiege & Pudritz (2000*a*,*b*). In our equilibrium models, we also take into account the propagation of torsional Alfvén waves. A simple analytical model is developed, followed by more general analytical models, and the latter are constrained using the limited observational constraints that are available (Morris et al. 2006, Sofue 2007, Matsumura et al. 2012). Our models provide the equilibrium structure needed to study the instabilities described by Matsumura et al. (2012), Sofue (2007), and Morris et al. (2006) that are believed to trigger the coiling of a twisted magnetic tube, which we will explore in a future paper. An especially interesting question that we will address in future work is that of why some molecular tornadoes appear to exhibit an $m = 1$ mode of instability, while others appear to be dominated by the $m = 2$ mode. Additionally, the equilibrium models developed here, and in our forthcoming stability calculations, will enable us to predict sub-millimetre polarization maps, to hopefully further constrain our models in the future, when such maps become available.

Hansen et al. (1976) provided a theoretical study of the equilibrium and stability of uniformly rotating, isothermal, and infinitely long gas cylinders of finite radius. They noted an interesting feature, in which the density fluctuates non-monotonically as a function of radius. These fluctuations can be seen in Figure 1 of Hansen et al. (1976), where they were referred to as "density inversions." Density inversions were also found by Recchi et al. (2014), who studied the equilibrium of uniformly and differentially rotating, nonmagnetic,

pressure truncated filaments. Hansen et al. (1976) suggested that density inversions are due to a battle between gravitational, centrifugal, and pressure gradient forces in maintaining the filament in equilibrium, and Recchi et al. (2014) proposed that such density profiles must be truncated by an external pressure before any density inversion occurs, because they would otherwise not be physically representative of observed filaments. We adopt this viewpoint in our helically magnetized models, which we truncate whenever the density is seen to increase with radius.

Kaur et al. (2006) presented their findings on differentially rotating, self-gravitating filaments, and have incorporated the effects of a helical magnetic field. They took into account the isothermal and logatropic equations of state, combined with constant velocity, and constant angular momentum rotation laws. The magnetic field in their model is proportional to the square root of the density of the filament. We also examine isothermal models, but with rotation laws that follow a power law in radius, as well as rotation laws that follow a power law in magnetic flux. Physics of torsional Alfvén waves are taken into account in our models, which has not been incorporated in the models of Kaur et al. (2006). The assumption of a torsional Alfvén wave couples the toroidal magnetic field $B_\phi(r)$ to the rotation law $\Omega(r)$ (see Section 7.2.2). Thus, the physics of torsional Alfvén waves provides a realistic constraint on the model, and results in interesting insights into the physics of molecular tornadoes.

Our model of molecular tornadoes begins with the equations of steady state MHD (Section 7.2). A special analytical solution is presented in Section 7.2.1. This closed form solution is not general, but it is interesting and does provide some insight into the physics of molecular tornadoes. Various differential rotation laws are described in Section 7.2.2 including a constraint due to torsional Alfvén waves. We conduct a virial analysis introduced in Section 7.2.3. Section 7.2.4 describes MHD stability conditions, which can be used to estimate the rotation rate. Our numerical method is presented in Section 7.2.5, and the method for constraining our models by observed quantities is included in Section 7.2.6. Results are shown

in Section 7.3, discussed in Section 7.4, and summarized in Section 7.5.

7.2 Theory

We assume ideal MHD, as described by the four ideal MHD equations in steady state – the continuity equation, Cauchy momentum equation, Faraday's Law, and the isothermal equation of state, respectively given by

$$\boldsymbol{\nabla} \cdot (\rho \boldsymbol{v}) = 0, \tag{7.1a}$$

$$\rho(\boldsymbol{v} \cdot \boldsymbol{\nabla})\boldsymbol{v} = -\boldsymbol{\nabla} P - \rho \boldsymbol{\nabla} \Phi + \frac{(\boldsymbol{\nabla} \times \boldsymbol{B}) \times \boldsymbol{B}}{4\pi}, \tag{7.1b}$$

$$\boldsymbol{\nabla} \times (\boldsymbol{v} \times \boldsymbol{B}) = 0, \text{ and} \tag{7.1c}$$

$$P = \sigma^2 \rho, \tag{7.1d}$$

where ρ is the density, $\boldsymbol{v}$ is the velocity, P is the pressure, $\boldsymbol{B}$ is the magnetic field, Φ is the gravitational potential, and σ is the velocity dispersion. We consider the velocity dispersion to contain both thermal and nonthermal contributions: $\sigma = \sqrt{\sigma_{thermal}^2 + \sigma_{nonthermal}^2}$.

For convenience, we define a set of dimensionless quantities, written here with an overscript tilde, where the physical quantities are scaled according to the following scaling laws:

$$\rho = \rho_0 \tilde{\rho}, \tag{7.2a}$$

$$r = \frac{\sigma}{\sqrt{4\pi G \rho_0}} \tilde{r}, \tag{7.2b}$$

$$P = \sigma^2 \rho_0 \tilde{P}, \tag{7.2c}$$

$$B = \sigma \sqrt{\rho_0} \tilde{B}, \tag{7.2d}$$

$$\Phi = \sigma^2 \tilde{\Phi}, \tag{7.2e}$$

$$g = \sqrt{4\pi G\rho_0}\sigma\tilde{g}, \tag{7.2f}$$

$$m = \frac{\sigma^2}{4\pi G}\tilde{m}, \tag{7.2g}$$

$$v_\phi = \sigma\tilde{v}_\phi, \tag{7.2h}$$

and

$$\Omega = \Omega_0\tilde{\Omega} = \sqrt{4\pi G\rho_0}\tilde{\Omega}. \tag{7.2i}$$

In these scaling relations, G is the universal gravitational constant, g is the gravitational field, m is the linear mass, v_ϕ is the rotational speed, and Ω is the rotational frequency. The subscript 0 denotes the quantities at the filament's radial core ($r = 0$). It should be noted that all physical quantities, except σ, are considered functions of r. *Hereafter, the overscript tilde notation is dropped, except where otherwise noted, since model quantities are presented in dimensionless form for most of the paper.*

By assuming cylindrical symmetry (r, ϕ, z) and rotational motion only, the velocity and magnetic field take the form

$$\boldsymbol{v} = v_\phi(r)\,\hat{\phi}, \tag{7.3a}$$

and

$$\boldsymbol{B} = B_\phi(r)\,\hat{\phi} + B_z(r)\,\hat{z}. \tag{7.3b}$$

Using the assumption of Equation 7.3, the only non-trivial terms of Equation 7.1 are in the $\hat{r}$ direction. Both the continuity equation and Faraday's law are satisfied automatically under the assumption of Equation 7.3, while the Cauchy momentum Equation simplifies to

$$0 = -\frac{\mathrm{d}P}{\mathrm{d}r} - \rho\frac{\mathrm{d}\Phi}{\mathrm{d}r} + \rho\frac{v_\phi^2}{r} - \frac{B_\phi^2}{4\pi r} - \frac{\partial}{\partial r}\left(\frac{B_\phi^2 + B_z^2}{8\pi}\right). \tag{7.4}$$

We introduce the magnetic flux-to-mass ratios formulated by Fiege & Pudritz (2000*a*). The

toroidal and poloidal magnetic flux-to-mass ratios are defined by

$$\Gamma_\phi = \frac{B_\phi}{r\rho}, \tag{7.5a}$$

and

$$\Gamma_z = \frac{B_z}{\rho}, \tag{7.5b}$$

respectively. The flux-to-mass ratios are free functions of the magnetic flux Φ_M in the context of perfect MHD due to Ferraro's law of isorotation (Ferraro 1937), but flux $\Phi_M(r)$ is a function of r in cylindrical symmetry. Fiege & Pudritz (2000*a*) assumed that both Γ_z and Γ_ϕ were constant. However, we consider the possibility that these functions might vary as a function of Φ_M, or equivalently r.

In addition to the equations of MHD, the effects of gravity also need to be taken into account. The gravitational field, $g(r) := -\partial\Phi(r)/\partial r$, is described by Poisson's equation for gravity, which becomes

$$\frac{\mathrm{d}g}{\mathrm{d}r} = -\frac{g}{r} - \rho. \tag{7.6}$$

Having defined g, Equation 7.4 can be expressed as

$$\frac{\mathrm{d}\rho}{\mathrm{d}r} = \frac{\rho g + \rho\Omega^2 r - \frac{1}{2\pi} r\rho^2\Gamma_\phi^2 - \frac{1}{8\pi} r^2\rho^2 \frac{\partial}{\partial r}\Gamma_\phi^2 - \frac{1}{8\pi}\rho^2 \frac{\partial}{\partial r}\Gamma_z^2}{1 + \frac{1}{4\pi} r^2\rho\Gamma_\phi^2 + \frac{1}{4\pi}\rho\Gamma_z^2}. \tag{7.7}$$

It is not generally possible to solve this equation analytically except under special assumptions. For most of the work presented in the paper, we apply numerical methods to solve Equation 7.7, taking into account the physics of torsional Alfvén waves (see Section 7.2.2), which leads to the numerical solutions presented in Section 7.3. However, we first present one special solution that can be solved analytically.

7.2.1 Analytic Solution: Rotational Balance with Toroidal Magnetic Stress

In this section, we derive a special analytical solution for the case where centrifugal forces exactly balance magnetic stresses from the toroidal field. We acknowledge that this solution is very specific, and therefore lacks the generality of the numerical solutions presented later in this paper. All quantities are presented in dimensionless form, where we have dropped the overscript tilde notation.

Various simplifying terms and assumptions are introduced so that the momentum equation (Equation 7.4) is simplified, which leads to an interesting analytical solution. We first introduce a "total" pressure defined by

$$P_{tot} = P + \frac{B_\phi^2 + B_z^2}{8\pi}. \tag{7.8}$$

Our analytical solution requires that the centrifugal force balances exactly with the inward toroidal magnetic stress, so that

$$\rho v_\phi^2 - \frac{B_\phi^2}{4\pi} = 0. \tag{7.9}$$

We further assume that the ratio of pressure and total magnetic pressure is constant:

$$\beta = P\left(\frac{B_\phi^2}{8\pi} + \frac{B_z^2}{8\pi}\right)^{-1} = constant. \tag{7.10}$$

We define

$$\beta_z := \frac{P}{P_{mag,z}}, \tag{7.11a}$$

and

$$\beta_\phi := \frac{P}{P_{mag,\phi}}, \tag{7.11b}$$

where β_z and β_z are also constant, so that Equation 7.10 can be written as

$$\beta = \left(\frac{1}{\beta_z} + \frac{1}{\beta_\phi}\right)^{-1}. \tag{7.12}$$

Using the definition of β_ϕ in Equation 7.9, and the definitions of σ from Equation 7.1d, it is straightforward to show that

$$\begin{aligned} 0 &= \rho v_\phi^2 - 2P_{mag,\phi} \\ \rho v_\phi^2 &= 2\frac{P}{\beta_\phi} \\ \frac{P}{\rho} &= \frac{\beta_\phi}{2} v_\phi^2 \\ \sigma^2 &= \frac{\beta_\phi}{2} v_\phi^2 \end{aligned} \tag{7.13}$$

$$v_\phi = \sqrt{\frac{2\sigma^2}{\beta_\phi}} = constant. \tag{7.14}$$

Equation 7.14 implies that the velocity field is highly sheared at $r = 0$, which violates the usual boundary condition $v_\phi(0) = 0$. Thus our special solution may not be physical very close to the axis $r = 0$. Interestingly, Kaur et al. (2006) have also considered constant v_ϕ models.

The total pressure is then given by the sum of the gas pressure (possibly including non-thermal contributions) and the magnetic partial pressures according to

$$P_{tot} = P + P_{mag,z} + P_{mag,\phi} = P\left(1 + \frac{1}{\beta_z} + \frac{1}{\beta_\phi}\right). \tag{7.15}$$

Furthermore, we define an *effective* sound speed given by

$$\sigma_{eff}^2 := \left(1 + \frac{1}{\beta_z} + \frac{1}{\beta_\phi}\right)\sigma^2, \tag{7.16}$$

where dimensional units are restored for this equation only, so that we can *redefine* the

dimensionless gravitational potential

$$\tilde{\Phi} := \frac{\Phi}{\sigma_{eff}^2}, \tag{7.17}$$

which is used to express Poisson's equation for gravity in dimensionless form. Once again dropping the tilde notation, by assuming that centrifugal force and toroidal magnetic stresses exactly balance (Equation 7.9), and incorporating Equations 7.15 and 7.17, Equation 7.4 becomes

$$0 = \frac{\partial}{\partial r} \log \rho + \frac{\partial}{\partial r} \Phi, \tag{7.18}$$

which can be integrated to find a solution for ρ so that Poisson's equation can be written as

$$\nabla^2 \Phi = \mathrm{e}^{-\Phi}, \tag{7.19}$$

where r_0 is redefined as

$$r_0 = \frac{\sigma_{eff}}{\sqrt{4\pi G \rho_0}}. \tag{7.20}$$

Equation 7.19 was solved in cylindrical symmetry by Ostriker (1964) in his study of nonrotating, nonmagnetic, isothermal filaments. Restoring dimensions, we therefore obtain an analogous solution for a rotating, magnetic filament:

$$\rho = \frac{\rho_0}{\left(1 + \frac{r^2}{8 r_0^2}\right)^2}, \tag{7.21a}$$

and

$$v_\phi = \sqrt{\frac{2\sigma^2}{\beta_\phi}}, \tag{7.21b}$$

where

$$r_0^2 = \frac{\sigma^2 (1 + \beta_z^{-1} + \beta_\phi^{-1})}{4\pi G \rho_0}. \tag{7.21c}$$

Thus, our analytic solution is a rescaling of the Ostriker solution, where the core radius r_0 is modified by the magnetic field. The filament rotates with constant velocity. The density inversions noted by Hansen et al. (1976) and Recchi et al. (2014) are absent from this special solution.

Nagasawa (1987) studied the stability of nonrotating isothermal cylinders threaded by a constant, trivial axial magnetic field. The lack of magnetic stresses from such a constant magnetic field do not modify the equilibrium structure from the Ostriker solution. In contrast, the analytical solution presented above has a radial scale modified by both axial and toroidal magnetic stresses. The solutions we explore throughout the rest of this work include non-trivial magnetic stresses.

7.2.2 Differential Rotation

The special solution presented in Section 7.2.1 represents a finely tuned special case, which we now generalize. Rotation plays an important role in the morphology of molecular tornadoes as seen in observations (Morris et al. 2006, Sofue 2007, Matsumura et al. 2012) and past work on rotating filaments (Hansen et al. 1976, Recchi et al. 2014). It is useful to examine several possible rotation laws in order to accurately describe and understand the physics of molecular tornadoes.

Angular Frequency as a Power Law

We consider a rotation law where Ω scales with the radius r according to a power law with index α:

$$\Omega = \Omega_0 \left(\frac{r}{r_0} \right)^{\alpha}. \tag{7.22}$$

Keplerian rotation and solid body rotation are considered to be limiting cases. We show below that this assumption constrains α to the range $-1 \leq \alpha \leq 0$, where $\alpha = 0$ is the case for solid body rotation. For clarity, we note that the $\alpha = -1$ index would be more accurately described as "Keplerian-like" where gas orbits a line mass in the absence of pressure gradients.

Keplerian Rotation

Poisson's equation and the divergence theorem are used to find the following relationship for g in terms of r:

$$\begin{aligned} \nabla^2 \Phi &= 4\pi G\rho \\ \int \boldsymbol{\nabla} \cdot \boldsymbol{\nabla}\Phi \, \mathrm{d}V &= \int 4\pi G\rho \, \mathrm{d}V \\ \oint \boldsymbol{\nabla}\Phi \cdot \, \mathrm{d}\boldsymbol{S} &= 4\pi G M(r) \\ -2\pi g r L &= 4\pi G M(r) \\ |g| &= \frac{2GM}{rL} \end{aligned} \tag{7.23}$$

where M is the filament mass and L is its length. By introducing the linear mass $m = M/L$, equating the angular acceleration and gravitational acceleration implies that

$$\Omega = \frac{v_\phi}{r} = \frac{\sqrt{2Gm(r)}}{r}. \tag{7.24}$$

Thus we find that Keplerian rotation is just a special case of the radial power law (Equation 7.22) with $\alpha = -1$.

Rotational Frequency as a Free Function of Magnetic Field Lines

We follow the methods introduced by Mouschovias (1976) and Tomisaka et al. (1988*b*) to describe the rotational frequency as a function the magnetic flux Φ_M, so that $v_\phi = \Omega(\Phi_M)r$.

Assuming Γ_z is constant, we find that

$$\begin{aligned} \Gamma_z &= \frac{\partial \Phi_M}{\partial M} \\ &= \frac{\partial \Phi_M}{\partial r}\left(\frac{\partial M}{\partial r}\right)^{-1} \\ \frac{\partial \Phi_M}{\partial r} &= \Gamma_z \frac{\partial M}{\partial r} \end{aligned} \tag{7.25}$$

$$\frac{\partial \Phi_M}{\partial r} = 2\pi \Gamma_z \rho r. \tag{7.26}$$

The angular frequency Ω is solved numerically from $\partial \Phi_M / \partial r$ along with other quantities mentioned later in Section 7.2.5. The rotational frequency is then assumed to follow a power law

$$\Omega(\Phi_M) = \Omega_0 \Phi_M^{\alpha_M}. \tag{7.27}$$

The lower limit on α_M is determined by the proportionality relations: $v_\phi \propto \Omega r \propto \Phi_M^{\alpha_M} r$ and $\Phi_M \propto B_z r^2 \propto r^2$, so that $v_\phi \propto r^{2\alpha_M+1}$. For $2\alpha_M + 1 > 0$, this indicates that $\alpha_M > -1/2$. For the sake of interest, we also analyze $\alpha_M \geq -1$ to understand how α_M affects the behaviour of the radial density.

Torsional Alfvén Waves

Appendix 7.7 derives equations for small amplitude oscillatory torsional Alfvén waves. Here, we present an analogous derivation for the wave front of a large amplitude torsional Alfvén wave, which is important for the numerical solutions presented in Section 7.3. In both Appendix 7.7 and this large amplitude scenario, we assume that the unperturbed rotation velocity and magnetic fields are described by

$$\boldsymbol{B}_0 = B_{z,0}\, \hat{z}, \tag{7.28a}$$

$$\boldsymbol{v}_0 = 0, \tag{7.28b}$$

$$\boldsymbol{B}_1 = B_{\phi,1}(z,t)\,\hat{\phi}, \tag{7.28c}$$

and

$$\boldsymbol{v}_1 = v_{\phi,1}(z,t)\,\hat{\phi}. \tag{7.28d}$$

From Equation 7.28 and the MHD equations (Equations 4.1, 4.11, 4.12,and 4.13), the continuity equation (Equation 4.1)

$$\partial_t \rho = 0, \tag{7.29a}$$

from the Cauchy momentum equation (Equation 4.12)

$$\rho \partial_t (v_\phi) = \frac{1}{4\pi} B_z \partial_z B_\phi, \tag{7.29b}$$

and from Faraday's law (Equation 4.11)

$$\partial_t B_\phi = B_z \partial_z v_\phi, \tag{7.29c}$$

$$\partial_t B_z = 0. \tag{7.29d}$$

Equation 7.29a says that the density ρ is constant in time, and Equation 7.29d says B_z is also constant in time (even if this was not already assumed). By taking the time derivative of Equation 7.29c,

$$\partial_t^2 B_\phi = B_z \partial_z (\partial_t v_\phi). \tag{7.29e}$$

Inserting the expression for $\partial_t v_\phi$ from Equation 7.29b into Equation 7.29e yields

$$\partial_t^2 B_\phi = v_A^2 \partial_z^2 B_\phi, \tag{7.30}$$

which is the general wave equation describing transverse perturbations propagating along the flux tube at the Alfvén speed (Jackson 1975)

$$v_A = \frac{B_0}{\sqrt{4\pi\rho_0}}. \tag{7.31}$$

A similar derivation also produces an analogous wave equation in terms of the rotational speed

$$\partial_t^2 v_\phi = v_A^2 \partial_z^2 v_\phi, \tag{7.32}$$

where the time derivative of Equation 7.29b is taken instead of the time derivative of Equation 7.29c.

Consider an Alfvén wave propagating locally along the flux tube, where the rotation velocity and magnetic fields are finite amplitude perturbations. Furthermore, B_z and ρ are constant in z and t. If an initially stationary flux tube starts to rotate at its base at time $t = 0$, the perturbation travels a distance $v_A \mathrm{d}t$ in time $\mathrm{d}t$, displacing the flux tube by distance $v_\phi \mathrm{d}t$. As the wave propagates along the flux tube, a toroidal magnetic field B_ϕ is generated. Consequently, Faraday's Law reduces to

$$\frac{\mathrm{d}B_\phi}{\mathrm{d}t} = B_z \frac{\mathrm{d}v_\phi}{\mathrm{d}z}. \tag{7.33}$$

The interface ($z = 0$) of the propagating wavefront separates the conditions above ($z > 0$) and below ($z < 0$) the wavefront. Above the wavefront interface, B_z is constant, and $B_\phi = 0$. Below the interface, the magnetic field has been perturbed and exhibits a toroidal component B_ϕ, and rotates at v_ϕ. A torsional Alfvén wave propagates along a magnetic flux tube at the Alfvén speed $v_A = \mathrm{d}z/\mathrm{d}t$. By integrating Faraday's Law (Equation 7.33), substituting

dt from v_A, and introducing the aforementioned bounds, we obtain

$$\int_{B_\phi}^{0} \mathrm{d}B_\phi = \frac{B_z}{v_A} \int_{v_\phi}^{0} \mathrm{d}v_\phi, \tag{7.34}$$

and follow through with the integration. Thus the field angle θ is perturbed according to

$$\tan\theta := \frac{B_\phi}{B_z} = \frac{v_\phi}{v_A}. \tag{7.35}$$

We use the flux-to-mass ratios (Equation 7.5a and Equation 7.5b) in Equation 7.35, as well as the Alfvén speed (v_A) to find

$$\Gamma_\phi = \sqrt{\frac{4\pi}{\rho}}\Omega, \tag{7.36}$$

where $\Gamma_\phi = \Gamma_\phi(r)$, in general.

7.2.3 Virial Analysis

The work by Sofue (2007) suggests that the GCT may not be bound by self-gravity. By extension, it may be possible that other molecular tornadoes may not require significant self-gravity to hold together. It is helpful to conduct a virial analysis in order to investigate the relative energies associated with various physical properties such as self-gravity, external pressures, magnetic fields, turbulence, and rotation.

Following Fiege & Pudritz (2000*a*), the virial equation that describes our models is given by

$$2\mathcal{K} + \mathcal{M} + \mathcal{W} = 0, \tag{7.37}$$

where script characters denote quantities per-unit-length; thus $\mathcal{K}$ is the total kinetic energy per unit length, $\mathcal{M}$ is the magnetic energy per unit length, and $\mathcal{W}$ is the gravitational energy per unit length. The total kinetic energy contains the rotational kinetic energy $\mathcal{K}_{rot}$, surface

pressure term $\mathcal{K}_P$, and internal turbulence $\mathcal{K}_\sigma$ so that

$$\mathcal{K} = \mathcal{K}_{rot} + \mathcal{K}_P + \mathcal{K}_\sigma. \tag{7.38}$$

The rotational kinetic energy is given by $\mathcal{K}_{rot} = (1/2)\mathcal{I}\Omega^2$, where $\mathcal{I}$ is the rotational inertia per unit length of a cylindrical filament spinning along its vertical axis. Energy associated with external pressure is given by $\mathcal{K}_P = -(3/2)P_S\mathcal{V}$ where $\mathcal{V} = \pi r_S^2$ is the cross-sectional area of the filament. The energy due to internal turbulence is given by $\mathcal{K}_\sigma = (3/2)m\sigma^2$. Gravitational energy is described by $\mathcal{W} = -m^2G$, which is valid for any equation of state, magnetic field, and internal structure (Fiege & Pudritz 2000*a*). Rearranging Equation 7.37 and normalizing by $|\mathcal{W}|$ yields

$$\frac{\mathcal{M}}{|\mathcal{W}|} = -2\left(\frac{\mathcal{K}_{rot}}{|\mathcal{W}|} + \frac{\mathcal{K}_\sigma}{|\mathcal{W}|} - \frac{|\mathcal{K}_P|}{|\mathcal{W}|}\right) - 1, \tag{7.39}$$

which is useful to find the relative magnetic energy components scaled by the gravitational energy. Determining the relative energies of these properties allows us to gain insight into which ones are particularly important for molecular tornadoes. Equation 7.39 makes it clear how terms contribute to the sign of $\mathcal{M}/|\mathcal{W}|$, which determines the dominating component of the magnetic field (Fiege & Pudritz 2000*a*). For $\mathcal{M}/|\mathcal{W}| < 0$, the toroidal component is dominant in pinching the filament, while $\mathcal{M}/|\mathcal{W}| > 0$ implies net support by the poloidal field. The numerical results in Section 7.3 are examined with the help of Equation 7.39.

7.2.4 Guidelines for Stability

Shafranov (1956) investigated the stability criterion for MHD instabilities. Unlike our equilibrium model for molecular tornadoes, the filaments discussed by Shafranov (1956) do not include rotation, self-gravity, nor are they truncated by external pressure. Nevertheless,

Shafranov (1956) provides a guideline for the stability analysis to be performed on our equilibrium model of molecular tornadoes, which will be presented in a future paper.

In the case where there is no B_z external to the cylinder, the condition for instability is

$$\frac{B_{\phi S}}{B_z} = \frac{v_{\phi S}}{v_A} > \left[\frac{1}{k^2}\left(1 - \frac{m^2}{m + kK_{m-1}(k)/K_m(k)}\right)\left(k\frac{I_{m-1}(k)}{I_m(k)}\right)\right]^{1/2} \tag{7.40}$$

(Shafranov 1956), where the magnetic field pitch angle relationship (Equation 7.35) at the cylinder surface is used, and I_m and K_m are modified Bessel functions of the first and second kind, respectively. In the case where there is no B_z external to the cylinder, the $m = 0$ (sausage), $m = 1$ (kink), and $m = 2$ modes are unstable when

$$\frac{B_{\phi S}}{B_z} = \frac{v_{\phi S}}{v_A} > \sqrt{2}, \tag{7.41a}$$

$$\frac{B_{\phi S}}{B_z} = \frac{v_{\phi S}}{v_A} > 1, \tag{7.41b}$$

and

$$\frac{B_{\phi S}}{B_z} = \frac{v_{\phi S}}{v_A} \gtrsim \frac{1}{0.26} \approx 3.85, \tag{7.41c}$$

respectively. Equivalently, the stability conditions above can be expressed in terms of the rotational period $P = 2\pi/\Omega_S$, and an Alfvén crossing time $\tau_A := \lambda/v_A$ that describes the time it takes for an Alfvén wave to propagate across one wavelength or pitch λ. The stability conditions in Equation 7.41 for $m = 0, 1,$ and 2, respectively, are expressed as

$$P < \frac{2\pi}{\sqrt{2}}\frac{r_S}{\lambda}\tau_A, \tag{7.42a}$$

$$P < 2\pi\frac{r_S}{\lambda}\tau_A, \tag{7.42b}$$

and

$$P \lesssim 2\pi(0.26)\frac{r_S}{\lambda}\tau_A. \tag{7.42c}$$

Equation 7.41 suggests that filaments that are stable against $m = 1$ instabilities are also stable against $m = 2$ instabilities. In other words, filaments that spin faster may still be stable against $m = 2$, but not $m = 1$ instabilities. It may also help to understand the stability conditions based on the axis ratio r_S/λ, as expressed in Equation 7.42. For a given v_ϕ/v_A, increasing the axis ratio will first stabilize against $m = 2$ instabilities before stabilizing against $m = 1$ instabilities. It will be interesting to see how these stability conditions described by Shafranov (1956) will compare to our molecular tornado models. Although Shafranov (1956)'s models are not exactly like those described in this paper, these stability relations are a useful guideline. In particular, Equation 7.41 is used to estimate the angular frequency of our equilibrium models in Section 7.2.6 as it sets a lower bound for the angular frequency required for the observed instability to occur. For example, the minimum rotation rate required for a filament to undergo a kink instability would be $\Omega_S > \sqrt{2}v_A/r_S$, according to Equation 7.41b. In other words, a molecular tornado observed with a kink instability must have been spinning at $\Omega_S > \sqrt{2}v_A/r_S$ for the instability to trigger.

7.2.5 Squashing Transformation

To efficiently calculate a wide range of r, and to better study the large r asymptotic behaviour of our equations, we employ a convenient "squashing" transformation to more easily numerically integrate out to large r. The squashing transformation transforms the dimensionless radius r into a dimensionless quantity ξ defined by $\xi \equiv \ln(r)$. The radial differential operators therefore transform according to

$$\frac{\mathrm{d}}{\mathrm{d}r} = \frac{1}{r}\frac{\mathrm{d}}{\mathrm{d}\xi}, \tag{7.43a}$$

and

$$\frac{\mathrm{d}^2}{\mathrm{d}r^2} = \frac{1}{r^2}\left(\frac{\mathrm{d}^2}{\mathrm{d}\xi^2} - \frac{\mathrm{d}}{\mathrm{d}\xi}\right). \tag{7.43b}$$

The equations for $g(r) = -\partial\Phi(r)/\partial r$, $\mathrm{d}g/\mathrm{d}r$ (Equation 7.6), and $\mathrm{d}\rho/\mathrm{d}r$ (Equation 7.7) are trivially transformed to equivalent equations using ξ as the independent variable, which is what we solve numerically.

In the case of Equation 7.36, where B_ϕ is due to a torsional Alfvén wave, it is useful to further simplify Equation 7.7. If Γ_z is constant, then Equation 7.7 can be expressed explicitly in terms of the dimensionless quantities Ω, and $\mathrm{d}\Omega/\mathrm{d}\xi$ by using the flux-to-mass ratios (Equation 7.5) along with the expression above for Ω (Equation 7.36). Algebraic simplification results in the expression

$$\frac{\mathrm{d}\rho}{\mathrm{d}\xi} = \frac{\rho g r - \Omega\rho r^2(\Omega + \frac{\mathrm{d}\Omega}{\mathrm{d}\xi})}{1 + \frac{1}{2}\Omega^2 r^2 + \frac{\rho}{4\pi}\Gamma_z^2}, \tag{7.44}$$

where we have used Equation 7.36 to write Γ_ϕ in terms of Ω.

7.2.6 Dimensionless Quantities: Comparing Observations with Numerical Models

Observations of molecular tornadoes measure some useful global quantities that can be used to constrain our solutions to Equation 7.44. We denote quantities at the surface of the filament with the subscript S, the radius from the filament axis to its surface r_S, surface pressure P_S, linear mass m_S, and rotational frequency Ω_S. These observables are written in terms of the dimensionless quantities of our model in the same manner as the scaling laws of Equation 7.2. Thus, there are five unknowns in the scaling laws: $\tilde{r}_S$, $\tilde{P}_S$, $\tilde{m}_S$, $\tilde{\Omega}_S$, and ρ_0. The readily observable (or at least somewhat observationally constrained) quantities are σ, r_S, m_S, and P_S. The central density ρ_0 cannot be easily obtained observationally, which also

makes r_0 difficult to obtain directly. Thus, we use the definition of r_0 to eliminate ρ_0 from the equations. This reduces the scaling laws for $\tilde{r}_S$, $\tilde{P}_S$, $\tilde{m}_S$, $\tilde{\Omega}_S$, and ρ_0 to three equations that describe combinations of the dimensionless quantities on the left side, in terms of observables on the right:

$$\tilde{r}_S^2 \tilde{P}_S = \frac{4\pi G}{\sigma^4} r_S^2 P_S, \tag{7.45a}$$

$$\tilde{m}_S = \frac{4\pi G}{\sigma^2} m_S, \tag{7.45b}$$

and

$$\frac{\tilde{\Omega}_S^2}{\tilde{P}_S} = \frac{\sigma^2}{4\pi G} \frac{\Omega_S^2}{P_S}. \tag{7.45c}$$

The surface pressure can be reasonably constrained from estimates of the isothermal equation of state, as well as from the dynamics and surface density of stars (Swinbank et al. 2011, Rathborne et al. 2014). Swinbank et al. (2011) and Rathborne et al. (2014) suggest that $P_S/k \gtrsim 10^7\,\mathrm{K\,cm^{-3}}$, and can possibly be as high as $\sim 10^8\,\mathrm{K\,cm^{-3}}$. The velocity dispersion for molecular clouds in the CMZ are roughly $\sigma \sim 15\,\mathrm{km\,s^{-1}}$ (Rathborne et al. 2014). The angular frequency of the filament in equilibrium is estimated from the Shafranov stability relations of Equation 7.41 as well as from the rotation mechanism, where possible.

Pigtail, DHN, and GCT

Our exploration focusses on the Pigtail to constrain our models. Equation 7.45 shows that there are five parameters that are necessary to constrain our dimensionless models by observations, namely $\tilde{r}_S$, $\tilde{P}_S$, $\tilde{m}_S$, $\tilde{\Omega}_S$, and σ. Most of these parameters were derived by observations of the Pigtail. The only exception was for rotation, which was not detected due to resolution limitations (Matsumura et al. 2012). The Pigtail's velocity dispersion is $\sigma = 13.2\,\mathrm{km\,s^{-1}}$, and $n(H_2) = 10^{3.5\pm0.25}\,\mathrm{cm^{-3}}$ (σ and $n(H_2)$ provided via private communica-

tions with Dr. Tomoharu Oka, Keio University; see also Matsumura et al. (2012)). Assuming hydrogen abundance $X = 0.7 \pm 0.05$, we estimate via the isothermal equation of state that $P_S/k = (2 \pm 1) \times 10^8\,\mathrm{K\,cm^{-3}}$. A direct measurement of the rope of the Pigtail from the figures of Matsumura et al. (2012) suggests that its radius is between $2 - 4\,\mathrm{pc}$. The pressure and velocity dispersion are assumed to be constant, and so it may be reasonable that the volume of the Pigtail rope between equilibrium and its present form is conserved. Thus, the radius of the filament in equilibrium r_S and the radius of the filament when the Pigtail has undergone instability r'_S, are related by the pitch angle via $r_S = r'_S \cos(\theta)$. The rotation speed of the equilibrium filament can be estimated either by considering that the flux tube is spun up by the shearing of two cloud orbits (Matsumura et al. 2012) or by the stability calculations of Shafranov (1956) mentioned in Section 7.2.4. In this case, we opt for the shearing mechanism described by (Matsumura et al. 2012) to derive the rotation frequency as the Shafranov stability conditions have underlying assumptions that differ from our models. Although, using the $m = 1$ stability criterion (Equation 7.41b) with the equilibrium radius and Alfvén speed $v_A \sim 35\,\mathrm{km\,s^{-1}}$ (Matsumura et al. 2012) produces a very close estimate (well within one order of magnitude) of the angular frequency to that derived by considering the shearing mechanism. These parameters result in dimensionless constraints

$$0.61 \lesssim \tilde{r}_S^2 \tilde{P}_S \lesssim 7.32, \tag{7.46a}$$

$$1.73 \lesssim \tilde{m}_S \lesssim 14.63, \tag{7.46b}$$

and

$$0.96 \lesssim \frac{\tilde{\Omega}_S^2}{\tilde{P}_S} \lesssim 11.52. \tag{7.46c}$$

There is more uncertainty in the physical parameters of the DHN and GCT, however. In particular, σ, Ω_S, and P_S are unclear. Generally, molecular clouds of the CMZ exhibit

$\sigma \sim 15$ km s^{-1} (Rathborne et al. 2014) which is similar to the Pigtail's velocity dispersion. For the DHN and GCT, we consider 10^7 K cm$^{-3} \lesssim P_S \lesssim 10^8$ K cm^{-3} (Rathborne et al. 2014) as a conservative estimate of the surrounding pressure. This range is slightly lower than the value that we have calculated for the Pigtail, and this discrepancy may be due to the density of the Pigtail, which could be lower than $n(H_2) = 10^{3.5\pm0.25}\,\mathrm{cm}^{-3}$ (Matsumura et al. 2012) on its surface, and/or a hydrogen abundance larger than $X = 0.7$. Our analysis focusses primarily on the Pigtail because observational measurements for the Pigtail have been more conclusive. Still, we attempt to carry out our analysis with the DHN and GCT, but the results should be taken with more caution.

CO observations have revealed two molecular counterparts that are likely associated with the DHN at radial velocities of ~ -35 km s^{-1} and 0 km s^{-1} having lengths $\sim 150\,\mathrm{pc}$, and masses of $0.8 \times 10^4\,M_\odot$ and $3.3 \times 10^4\,M_\odot$, respectively (Torii et al. 2014, Enokiya et al. 2014). The equilibrium radius of the DHN filament is conservatively estimated to fall between the narrowest strand width and the overall structure width $\sim 3.5\,\mathrm{pc}$ (Morris et al. 2006). The CND rotation is the proposed mechanism which drives the DHN. We assume that the CND rotation lies in the range $70 - 110\,\mathrm{km\,s}^{-1}$ (Morris et al. 2006, Enokiya et al. 2014). Alternatively, with r_S and $v_A = 10^3\,\mathrm{km\,s}^{-1}$ (Morris et al. 2006), an estimate of the angular frequency can be made via the $m = 2$ Shafranov stability relation of Equation 7.41c. We opt to use the angular frequency determined from the CND rotation for the analysis however, since there are assumptions made in Equation 7.41c that differ from our models (see Section 7.2.4). Regardless, the general qualitative conclusions drawn from either method of determining the rotation are similar (see Section 7.4.3). These parameters along with the pressure estimate from Swinbank et al. (2011) and Rathborne et al. (2014), correspond to

$$2 \times 10^{-4} \lesssim \tilde{r}_S^2 \tilde{P}_S \lesssim 0.27, \tag{7.47a}$$

$$0.08 \lesssim \tilde{m}_S \lesssim 0.32, \tag{7.47b}$$

and

$$80 \lesssim \frac{\tilde{\Omega}_S^2}{\tilde{P}_S} \lesssim 3 \times 10^5. \tag{7.47c}$$

Assuming $\sigma = 15$ km s^{-1}, and provided that the GCT has a density of $\rho \sim 2.7 \times 10^{-21}$ g cm^{-3} (Sofue 2007), the isothermal equation of state suggests an internal pressure of 4.4×10^7 K cm^{-3}. As a rough guideline, this is within the bounds of the external pressure that we consider. Sofue (2007) draws the similarity between the DHN and GCT that they both exhibit two strands wound in a double helix configuration, and postulates that they arise from a similar mechanism. Thus, we assume that the radius of the GCT is approximately $7-20$ pc wide, as estimated from the current radius of the GCT, and the size of the molecular cloud it may have originated from (Sofue 2007). The GCT's angular frequency is estimated from the Shafranov (1956) instability condition (Equation 7.41c). We acknowledge that the Shafranov conditions of Equation 7.41 describe minimum bounds for instability, and that the rotation does not have an upper bound. Realistically however, there must be an upper rotation limit otherwise the filament would be unstable and the filament would not remain intact. Even if the GCT were rotating faster than the rate described by Equation 7.41c, it should not be much faster before undergoing instability. Thus, we conservatively estimate limits on the angular frequency resulting from Equation 7.41c by multiplying by a factor of 0.5 to 2. These parameters correspond to

$$0.11 \lesssim \tilde{r}_S^2 \tilde{P}_S \lesssim 8.71, \tag{7.48a}$$

$$1.48 \lesssim \tilde{m}_S \lesssim 12.04, \tag{7.48b}$$

and

$$1.70 \lesssim \frac{\tilde{\Omega}_S^2}{\tilde{P}_S} \lesssim 2 \times 10^3. \tag{7.48c}$$

Most of the dimensionless constraints of Equations 7.46, 7.47, and 7.48 are based on absolute minimum and maximum bounds of the observed measurements, except where otherwise noted. These quantities are chosen to conservatively estimate the bounds of Equation 7.45 for each molecular tornado, in an attempt to account for the uncertainty in the observations (particularly with uncertainties associated with the DHN, and GCT).

7.3 Results

Results of numerically solving Equations 7.7 and 7.44, along with $\mathrm{d}\Phi/\mathrm{d}\xi$ and $\mathrm{d}g/\mathrm{d}\xi$, and the rotation laws described in Section 7.2.2 are presented in this section. The density ρ is calculated from the general form of the Cauchy momentum equation (Equation 7.7) for models excluding the Alfvén wave constraint (Equation 7.36). Equation 7.44 was derived under the constraint of Equation 7.36. The radial profile of ρ changes due to different rotation laws (Equations 7.22, and 7.27), magnetic fields, and self-gravity. These profiles are compared to the Ostriker solution, Equation 7.21, for isothermal, nonrotating, nonmagnetic, self-gravitating cylinders as a benchmark. At large radii, the Ostriker solution behaves as $\rho \sim r^{-4}$.

In our exploration, we are free to explore many different filament models. We have the flexibility to include or exclude self-gravity, choose between various rotation laws and their respective power law indices (see Section 7.2.2), and define the allowed range of r, Ω_0, Γ_z, and Γ_ϕ. While all of these models are interesting to explore, the most physically relevant models make use of the magnetic field angle constraint from torsional Alfvén waves, presented in Section 7.2.2. However, we also explore models that exclude this magnetic field constraint for comparison.

Numerical integration was performed with MATLAB's ode45, which is a Runge-Kutta 4-5 integrator. In a few cases where stiffness was detected, we used MATLAB's ode23s,

which is a low order method based on the Rosenbrock formula, and efficiently solves rapidly changing problems. We integrate over the range $r_{min} \leq r \leq r_{max}$, where the lower and upper limits to the dimensionless radius are $r_{min} = 10^{-6}$ and $r_{max} = 10^{6}$, respectively. If Ω follows the power law rotation given by Equation 7.22, then Ω_0, Γ_z, and Γ_ϕ are free parameters. In this case, Ω_0, Γ_z, and Γ_ϕ are each randomly chosen over the intervals

$$0 \leq \Omega_0 \leq 12, \tag{7.49a}$$

$$10^{-3} \leq \Gamma_z \leq 100, \tag{7.49b}$$

and

$$0 \leq \Gamma_\phi \leq 100. \tag{7.49c}$$

The limits of Equation 7.49 are conservatively chosen, with the limits of Γ_ϕ and Γ_z extended beyond that of Fiege & Pudritz (2000*a*) to account for the environment of the Galactic Centre. Each random set of Ω_0, Γ_z, and Γ_ϕ define a particular untruncated filament model. Otherwise if Ω follows a power law of magnetic flux (Equation 7.27), then Γ_z, and Γ_ϕ are free, randomly chosen over the same interval is in Equation 7.49, and define a unique density profile. The initial conditions at r_{min} are

$$\rho_0 = 1, \tag{7.50a}$$

$$\Phi_0 = 0, \tag{7.50b}$$

$$g_0 = 0, \tag{7.50c}$$

$$\Phi_{M,0} = \Gamma_z \pi r_{min}^2 \rho_0, \tag{7.50d}$$

and

$$m_0 = \pi \rho_0 r_{min}^2. \tag{7.50e}$$

The reader is reminded that all quantities in our numerical calculations are dimensionless.

Theoretical density profiles from solving Equation 7.7 (and 7.44) are shown in Figures 7.1 and 7.2. We halt the integration if a density inversion is encountered ($\mathrm{d}\rho/\mathrm{d}r > 0$), as recommended by Recchi et al. (2014). This condition also limits the density so that $\rho(r) \leq \rho_0$ everywhere. Some density profiles may be asymptotically constant at large radii, so these profiles were noted accordingly, but were allowed to integrate over the full range of r. For models including self-gravity, constant angular frequency, constant flux-to-mass ratios, and excluding the torsional Alfvén wave condition, changing Γ_z changes the asymptotic density value that is reached at large radii only by a small amount. This asymptotic value of ρ at large radii can be approximated from Equation 7.7, which reveals that

$$\rho \approx 2\pi \left(\frac{\Omega_0}{\Gamma_\phi} \right)^2. \tag{7.51}$$

Truncation pressures were chosen randomly, with half chosen from a uniform distribution, and half chosen from a logarithmic distribution. This choice allows us to sample a wide range of possible external pressures that a filament may reside in. The logarithmic distribution allows the truncation values to span the entire range of r, which is particularly useful for probing the low density tail that most density profiles exhibit at large r. The uniformly distributed truncation values better sample where observationally constrained models are more likely to reside (discussed further below; see Figure 7.5 as well). Solutions that exhibit density inversions are halted at the first density inversion, then further truncation pressures are chosen along the truncated density profile with the aforementioned distribution. At each point, a number of important parameters (ρ, P_S, Ω_S, Γ_ϕ, Γ_z, etc.) are evaluated. In total, we sample approximately 10^4 random combinations of the model parameters (Equation 7.49),

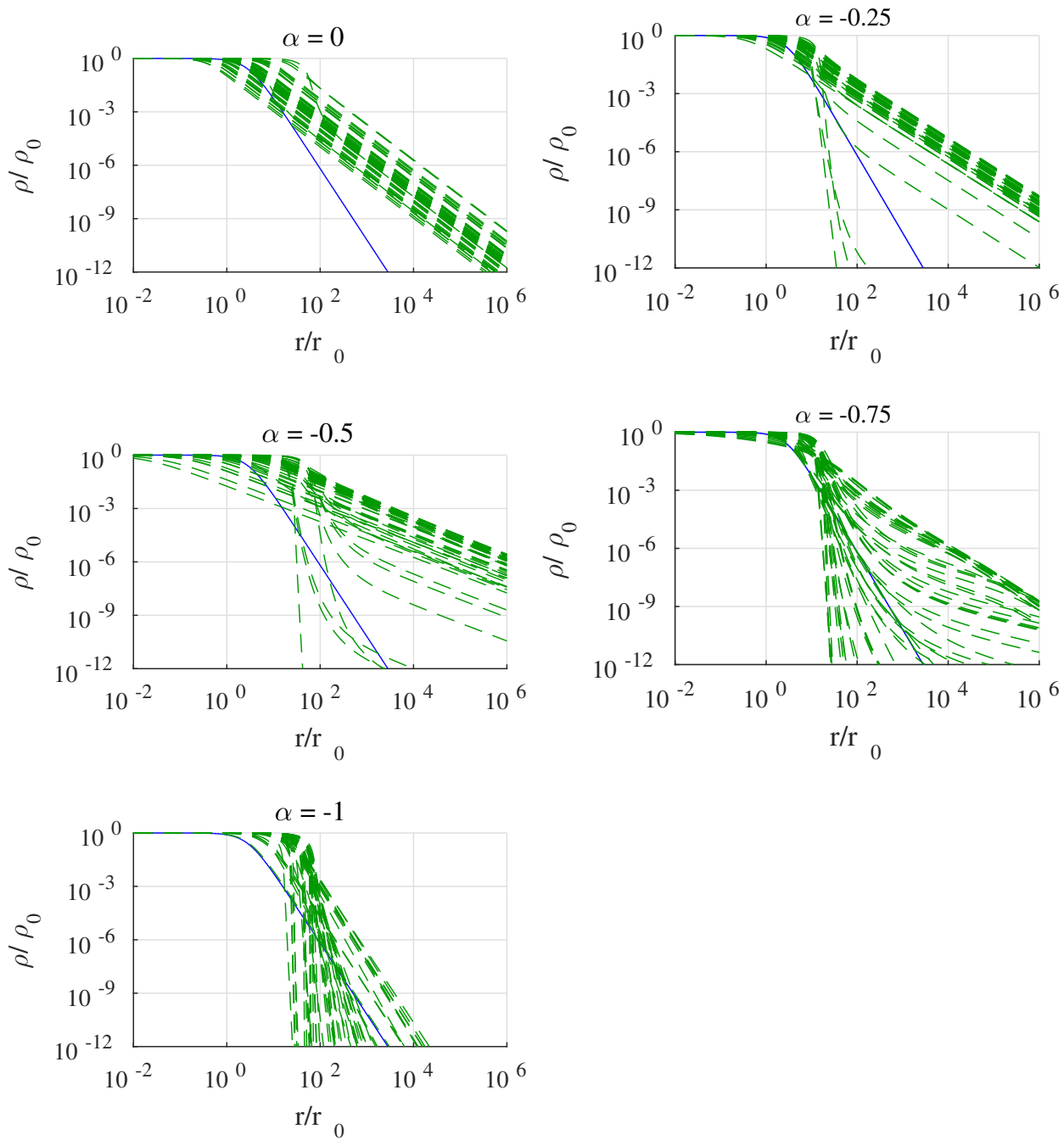

Figure 7.1: **Density profiles for filaments obeying the rotation law $\mathbf{\Omega = \Omega_0(r/r_0)^\alpha}$ and the torsional Alfvén wave constraint**. Green, dashed lines are theoretical density profiles. The Ostriker solution is the solid blue line for all plots, henceforth. Notice that as the power law index becomes more negative, solutions that behave as $\rho \sim r^{-4}$ or steeper occur more frequently. In each plot, there are 50 density profiles. It should be noted that each plot is magnified for clarity and the integration is from $r_{min} \leq r \leq r_{max}$.

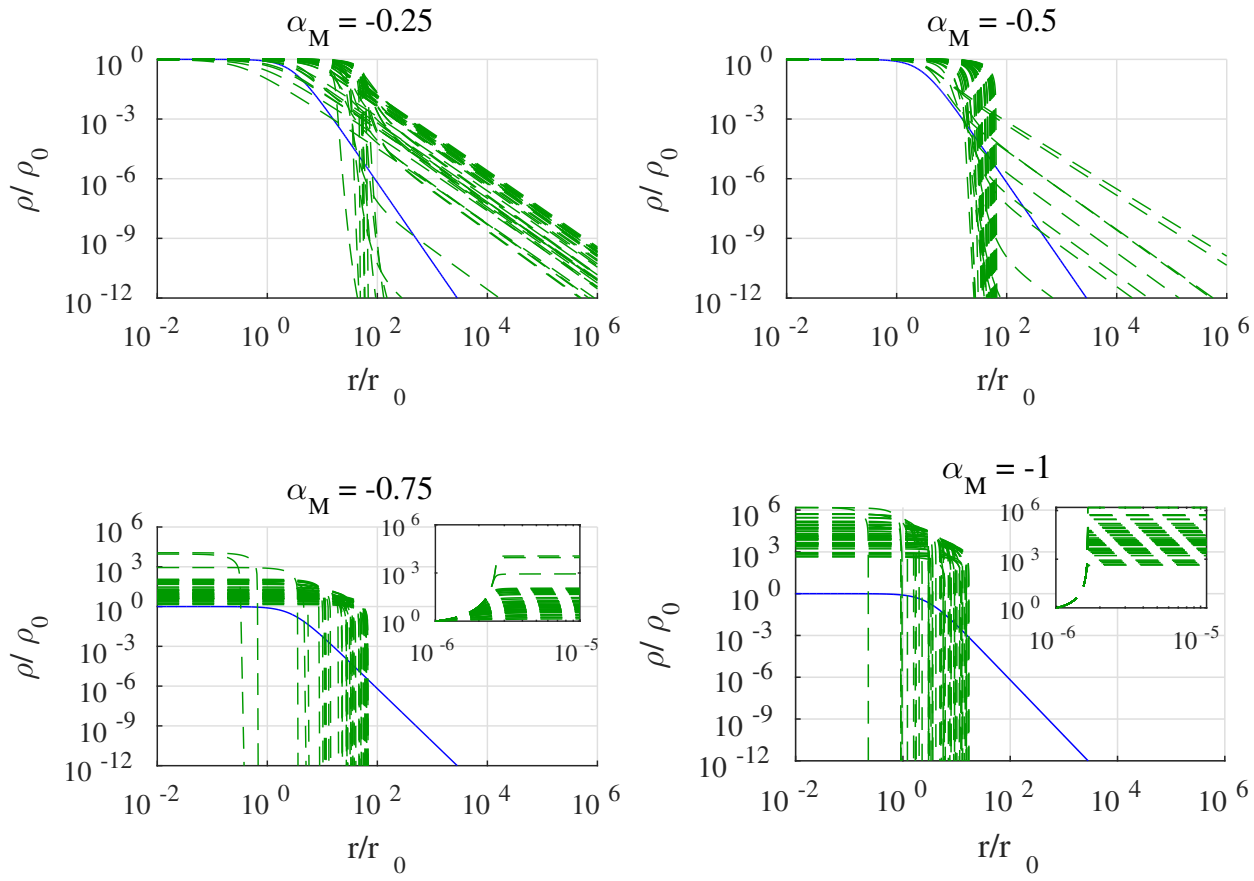

Figure 7.2: **Density profiles for filaments obeying the rotation law $\Omega = \Omega_0 \Phi_M^{\alpha_M}$ and the torsional Alfvén wave constraint**. Green, dashed lines are theoretical density profiles. Notice that as the power law index becomes more negative, solutions can become steeper. In each plot, there are 50 density profiles. It should be noted that each plot is magnified for clarity and the integration is from $r_{min} \leq r \leq r_{max}$. The inset has the same axis quantities as the host plot, and show the boundary condition $\rho(r_{min})/\rho_0 = 1$. The extreme density inversions shown in the inset are indeed part of the solutions, which we note are unphysical density inversions, and therefore excluded as feasible models. These extreme density inversions are due to Ω behaving as r^{-1} or steeper, so there is extreme rotation near the origin. The $\alpha_M = -0.75$ and -1 plots are included in this figure for the sake of interest only.

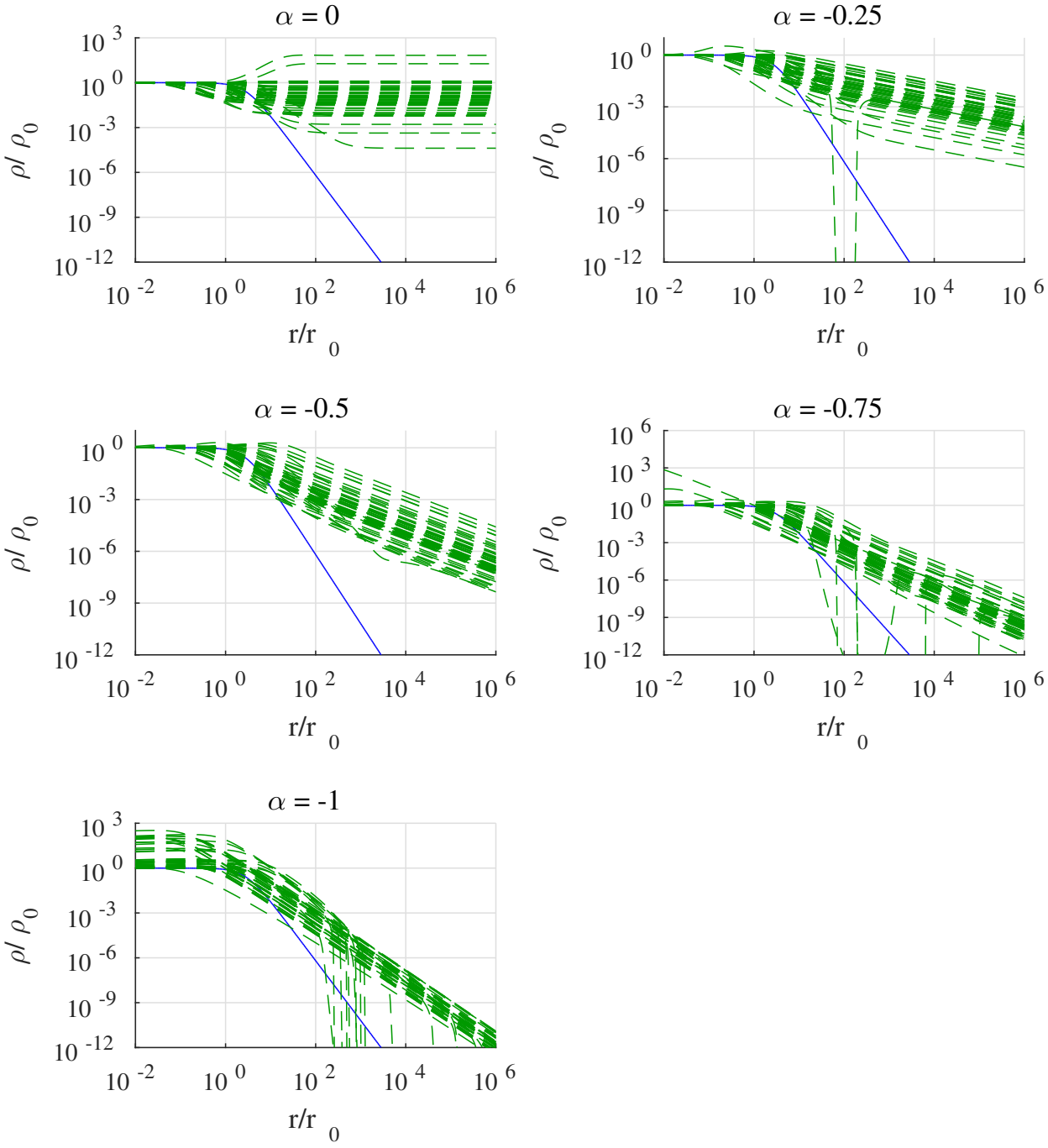

Figure 7.3: **Density profiles for filaments obeying the rotation law $\mathbf{\Omega = \Omega_0(r/r_0)^\alpha}$ without the torsional Alfvén wave constraint**. Green, dashed lines are theoretical density profiles. Notice that as the power law index becomes more negative, solutions that behave as $\rho \sim r^{-4}$ or steeper occur more frequently. In each plot, there are 50 density profiles. It should be noted that each plot is magnified for clarity and the integration is from $r_{min} \leq r \leq r_{max}$.

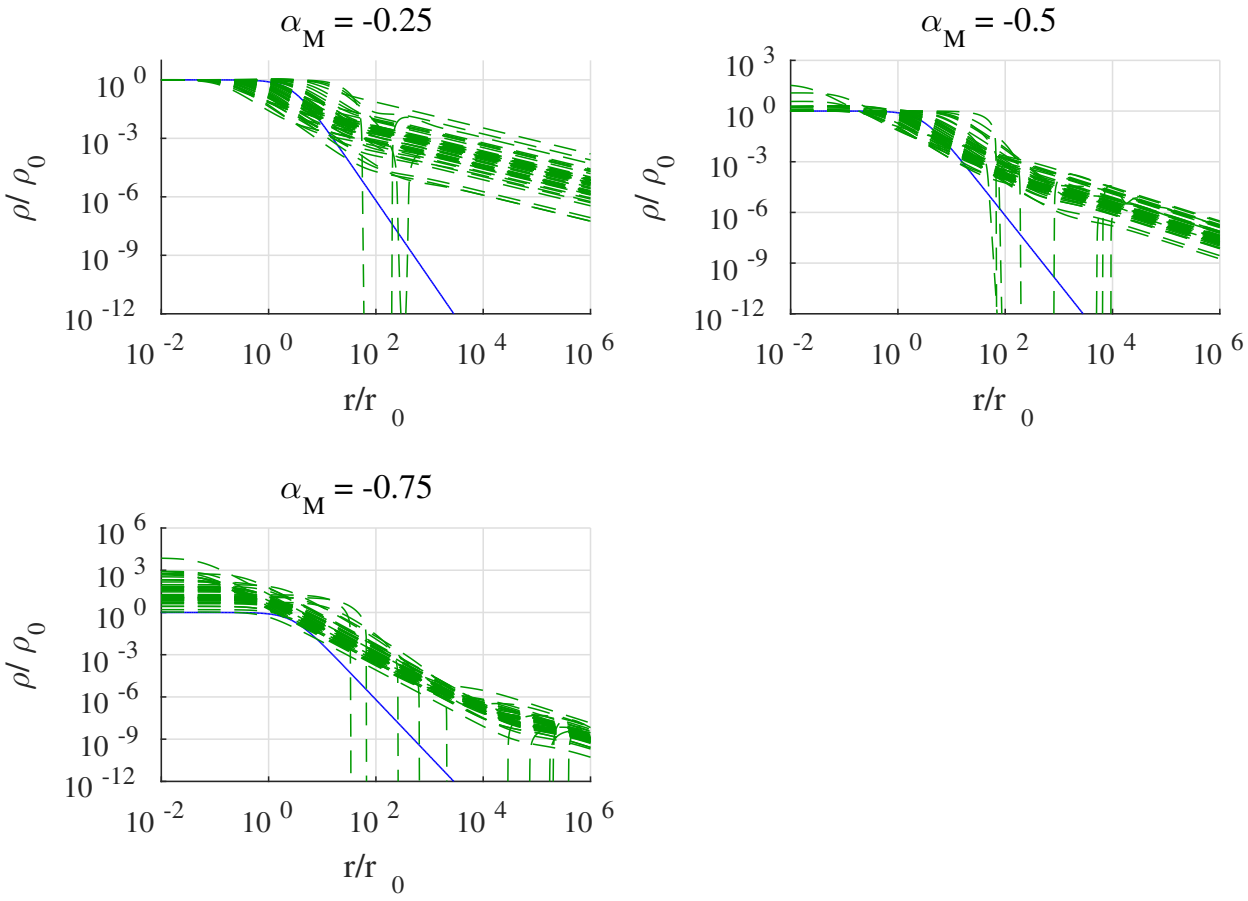

Figure 7.4: **Density profiles for filaments obeying the rotation law $\boldsymbol{\Omega = \Omega_0 \Phi_M^{\alpha_M}}$ without the torsional Alfvén wave constraint.** Green, dashed lines are theoretical density profiles. Notice that as the power law index becomes more negative, solutions can become steeper. In each plot, there are 50 density profiles. It should be noted that each plot is magnified for clarity and the integration is from $r_{min} \leq r \leq r_{max}$. The extreme density inversions are indeed part of the solutions, which we note are unphysical density inversions, and therefore excluded as feasible models. These extreme density inversions are due to Ω behaving as r^{-1} or steeper, so there is extreme rotation near the origin. The $\alpha_M = -0.75$ plot is included in this figure for the sake of interest only.

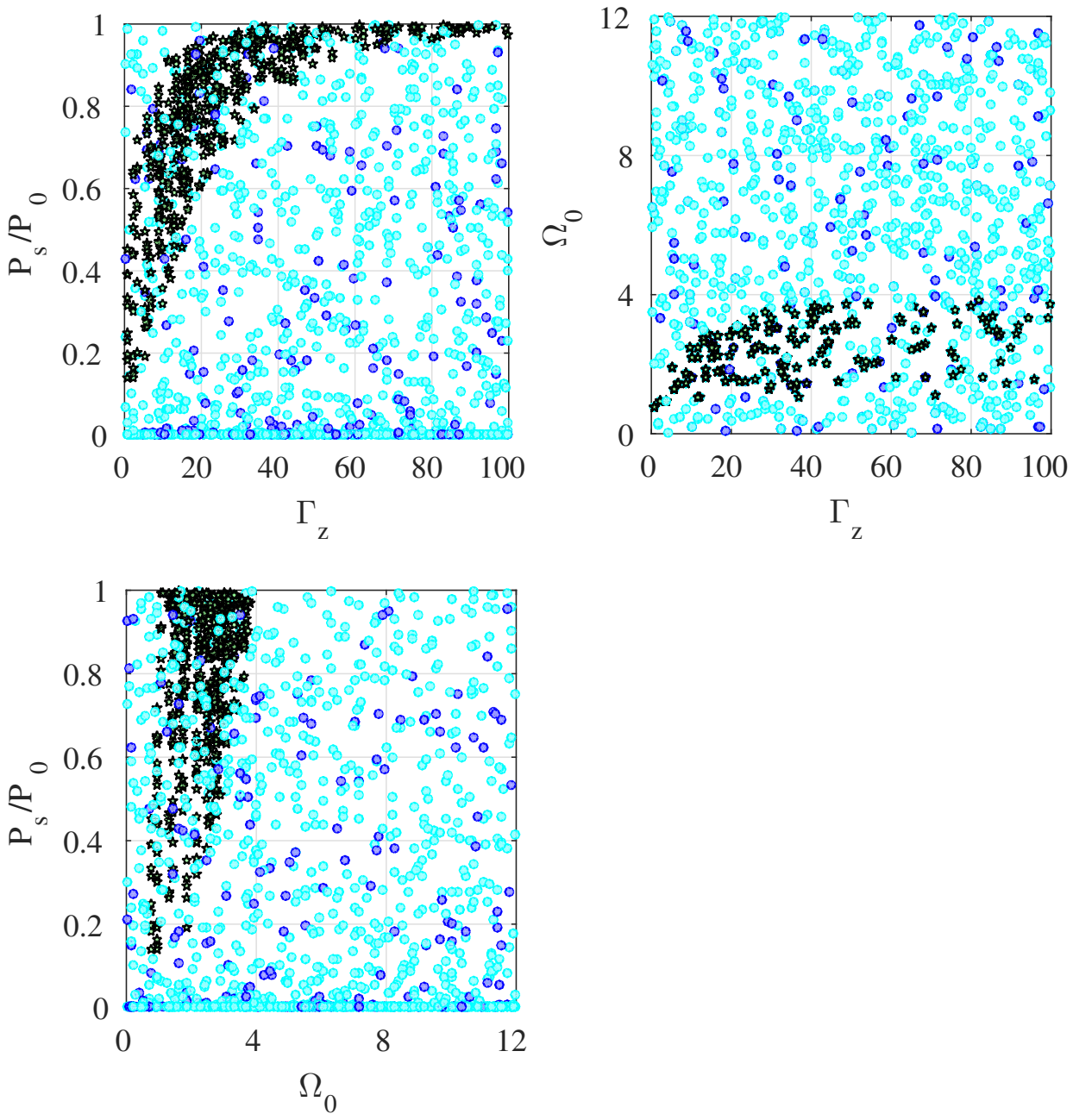

Figure 7.5: **Observationally constrained solutions**. Scatter plots of the self-gravitating, field-angle constrained, power law rotation (Equation 7.22) with $\alpha = -0.25$ model parameter space for the Pigtail. Green stars with black borders indicate where observations reside in the parameter space, cyan dots indicate models that self-truncate ($\mathrm{d}\rho/\mathrm{d}r < 0$), and blue dots indicate models where the density reaches asymptotically constant values ($\mathrm{d}\rho/\mathrm{d}r = 0$).

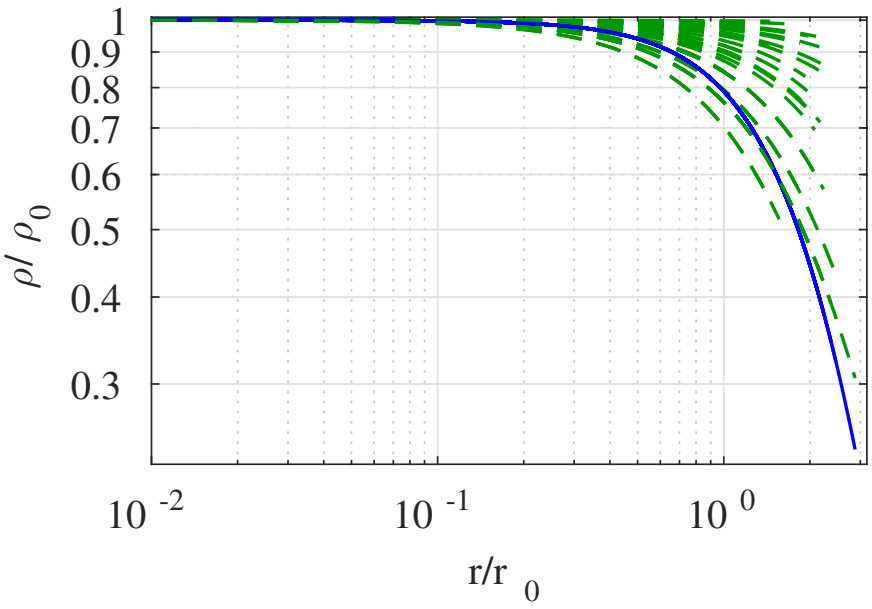

Figure 7.6: **A sample of density profiles (green dashed lines) corresponding to the green stars in the scatter plots of Figure 7.5.** Solutions begin at $r/r_0 = 10^{-6}$ and are pressure truncated around $r/r_0 = 10^0$. This figure suggests that external pressure is important in the description molecular tornado structure.

each describing a unique density profile for a particular rotation law. Additionally, each external truncation pressure characterizes a unique filament model. Since there are approximately 10^4 external pressures, we explore approximately 10^8 models for a given rotation law.

The parameters evaluated at each truncation pressure (ρ, P_S, Ω_S, Γ_ϕ, Γ_z, etc.) are used to constrain the parameter space where observed molecular filaments reside, according to the constraints of Equation 7.45. By converting the observed parameters into dimensionless quantities via Equation 7.45 (shown explicitly in Section 7.2.6), we plot where real filaments reside in the dimensionless parameter space (see Figures 7.5 and 7.6). The density profiles are also categorized based on their general behaviour or special characteristics. For example, some theoretical density profiles feature inversions (see Figure 7.7), some reach a constant density (at large radii), and some increase above ρ_0 (see Figures 7.2 and 7.8).

Having constrained the models within observational bounds, they can then be used to

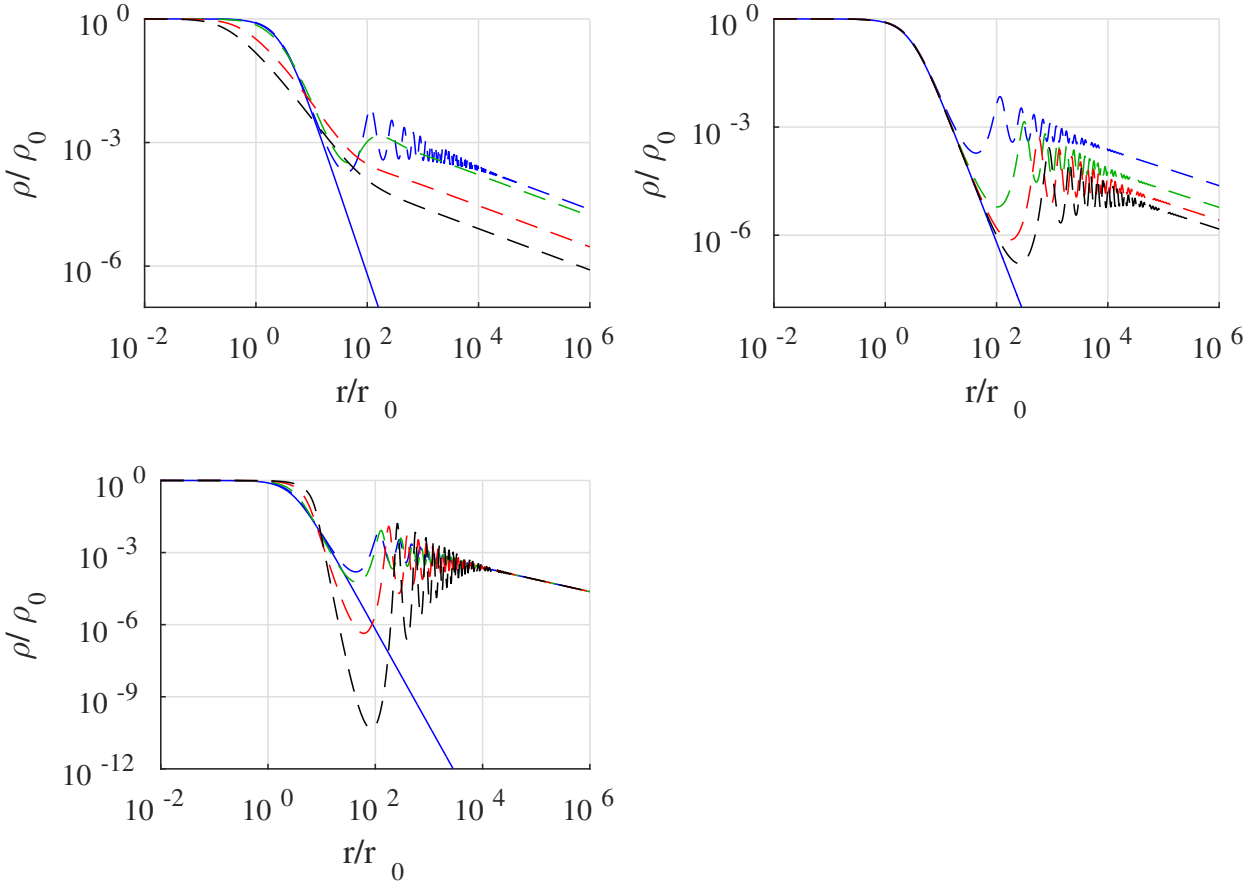

Figure 7.7: **Density inversions for self-gravitating, radial power law rotating (Equation 7.22), $\alpha = -0.25$ model without the torsional Alfvén wave constraint of Equation 7.36**. Constant parameters are set to $\Gamma_z = 1$, $\Gamma_\phi = \pi/50$, and $\Omega_0 = \pi/25$. Changing parameters are ordered as the dashed blue, green, red, and black lines, respectively: **(Left)** $\Gamma_\phi = \pi/100, \pi/2, 2\pi, 4\pi$; **(Centre)** $\Omega_0 = \pi/25, \pi/50, \pi/75, \pi/100$; **(Right)** $\Gamma_z = \pi/2, \pi, 2\pi, 3\pi$. It should be noted that each plot is magnified for clarity and the integration is indeed from $r_{min} \leq r \leq r_{max}$. Notice that as Γ_ϕ increases, the density profile becomes more pinched, and the inversions smooth out. As Ω_0 decreases, the inversions begin at lower densities. A larger Γ_z causes the inversions to increase in amplitude. Such density inversions are unrealistic, and the density profiles shown here are not truncated for the purpose of illustration only.

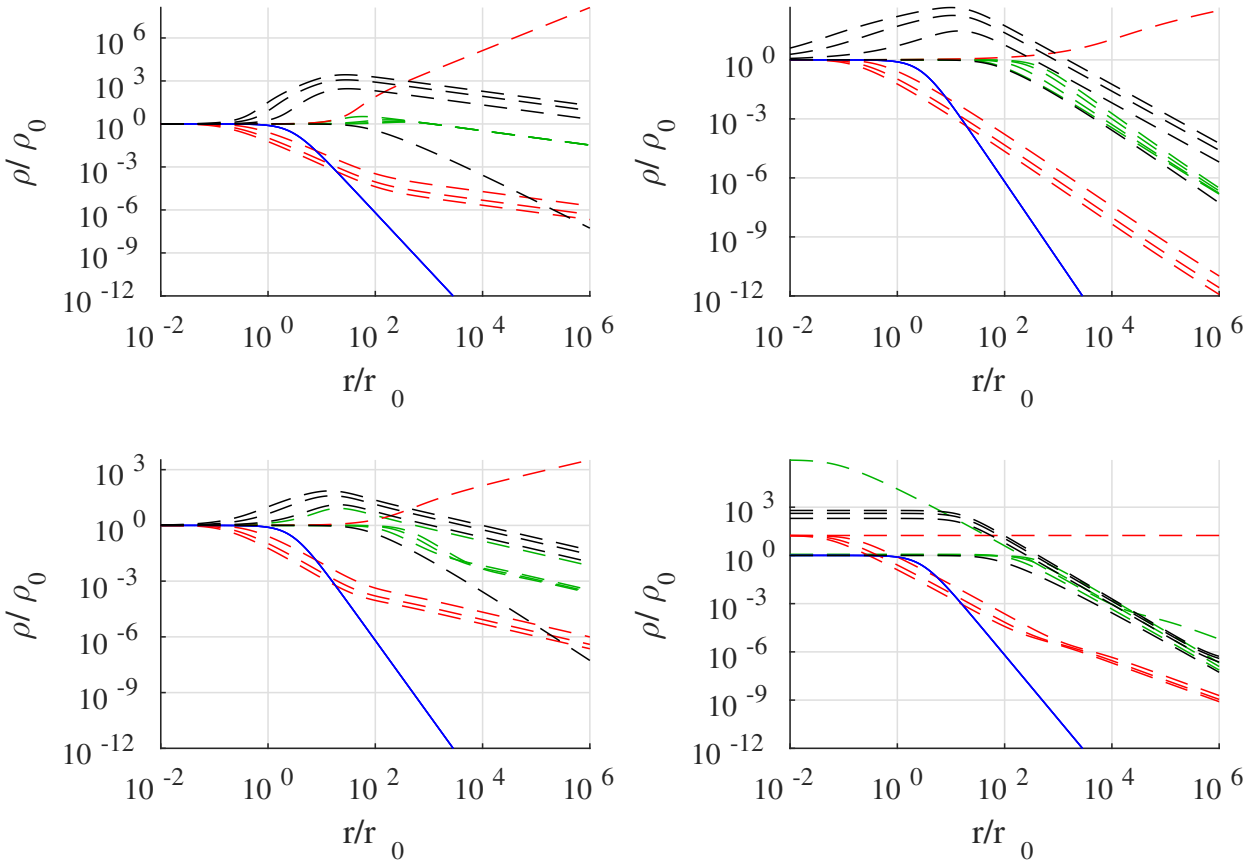

Figure 7.8: **Sample of changing model parameters excluding self-gravity and the torsional Alfvén wave condition**. All plots have parameters set such that the dashed line colours corresponding to parameters that change linearly (step size of 4) in the range $\Omega_0 = [0, 3]$, $\Gamma_z = [10^{-3}, 25]$, and $\Gamma_\phi = [0, 25]$. Green lines correspond to changes in Γ_z, red lines to Γ_ϕ, and black lines to Ω_0. If a parameter is constant then they are set to: $\Gamma_z = 1$, $\Gamma_\phi = \pi/50$, and $\Omega_0 = \pi/25$. For a set of coloured profiles, as Γ_z is increasing, the density profiles extend radially. As Γ_ϕ is increasing, the density profiles pinch (decrease in density overall). As Ω_0 increases, the overall density increases. **(Top Row)** Rotation law follows the radial power law (Equation 7.22). **(Top Left)** $\alpha = -0.25$. **(Top Right)** $\alpha = -0.75$. **(Bottom Row)** Rotation law follows the flux power law (Equation 7.27). **(Bottom Left)** $\alpha_M = -0.25$. **(Bottom Right)** $\alpha_M = -0.75$. It should be noted that each plot is magnified for clarity and the integration is indeed from $r_{min} \leq r \leq r_{max}$. The boundary condition $\rho(r_{min})/\rho_0 = 1$ is always met. In the case of $\alpha_M = -0.75$, ρ increases rapidly at $r/r_0 << 1$ due to unrealistic, extreme rotation near the origin, which is outside of the plot frame. All profiles which exceed ρ_0 are rejected from analysis and are considered unphysical models. These density profiles are not truncated for the purpose of illustration only.

analyze the virial equation (Equation 7.39). The result of this is shown in Figure 7.9 for self-gravitating models following the radial power law (Equation 7.22) with the torsional Alfvén wave condition (Equation 7.36), constrained by the Pigtail. Within observational constraints, our analysis shows that the magnetic-to-gravitational energy ratio is

$$-10^5 \lesssim \frac{\mathcal{M}}{|\mathcal{W}|} \lesssim 0, \tag{7.52}$$

and the ratio of the surface pressure term to gravitational energy is

$$10^0 \lesssim \frac{|\mathcal{K}_P|}{|\mathcal{W}|} \lesssim 10^3. \tag{7.53}$$

Comparing the surface pressure term to the magnetic energy reveals that

$$|\mathcal{M}| > |\mathcal{K}_P|$$

for most self-gravitating models with Equation 7.36 within observational constraints of the Pigtail as shown in Figure 7.10. These results are discussed further in Section 7.4.3.

7.4 Discussion

In this section, we discuss the results presented in Section 7.3. We compare the behaviour of our models when varying different parameters, to the Ostriker solution. Models that exclude torsional Alfvén wave physics (Equation 7.36) in Section 7.4.1 are first discussed, and in Section 7.4.2 we discuss models that include the constraints of torsional Alfvén waves. The results of our virial analysis are discussed in Section 7.4.3.

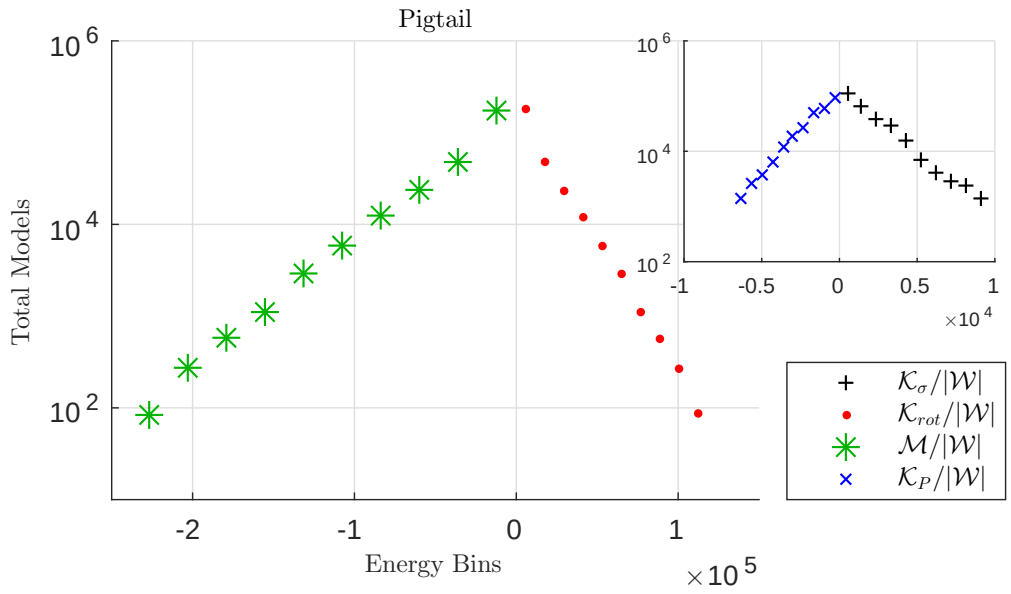

Figure 7.9: **Relative energies of observationally constrained models including self-gravity, power law rotation ($\Omega = \Omega_0(r/r_0)^{-0.25}$), and the torsional Alfvén wave condition.** Observational constraints are based on measurements of the Pigtail. The energy terms are taken from Equation 7.39. Notice that the pressure and magnetic stresses, in particular, play an important role in the equilibrium filament structure. The inset has the same axis labels as the host plot.

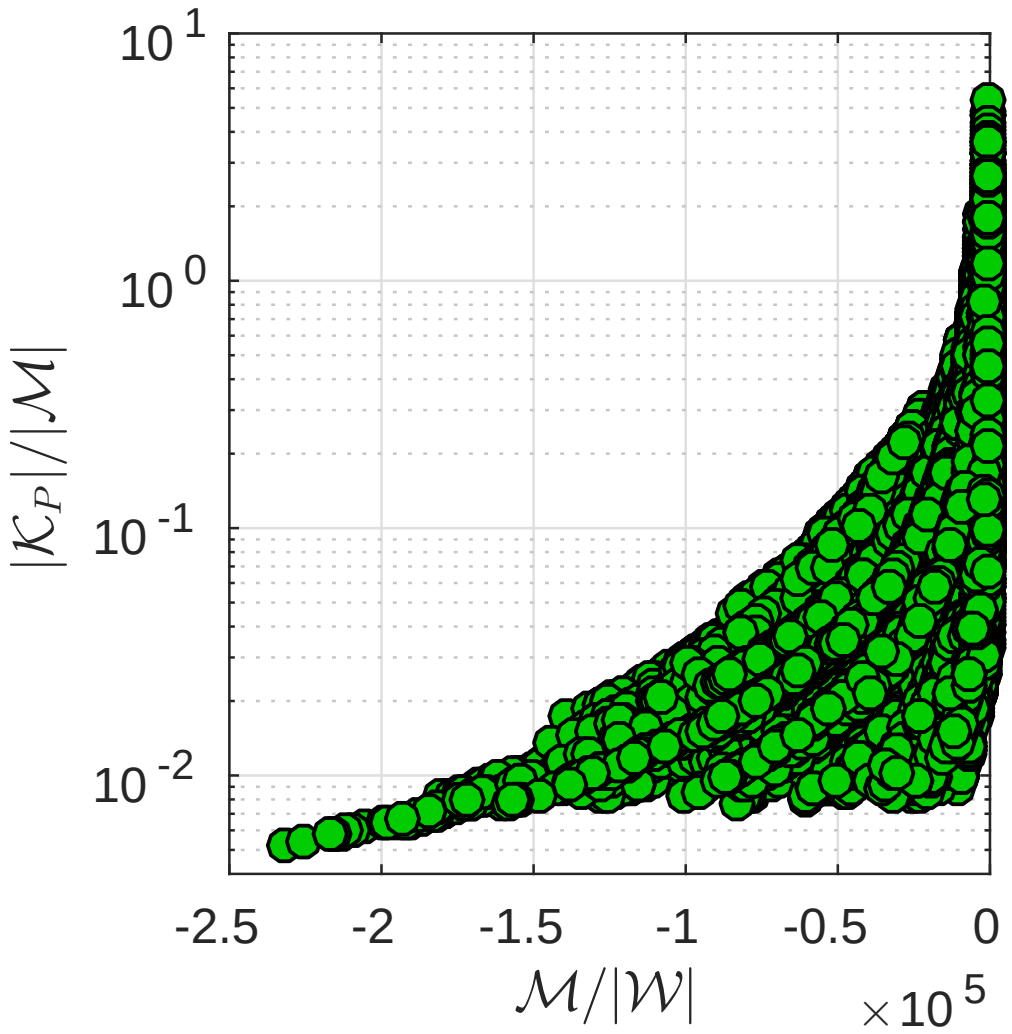

Figure 7.10: A semi-logarithmic plot of $|\mathcal{K}_P|/|\mathcal{M}|$ against $\mathcal{M}/|\mathcal{W}|$ shows that most self-gravitating models that include the torsional Alfvén wave condition (Equation 7.36) within observational constraints exhibit $|\mathcal{M}| > |\mathcal{K}_P|$. Quantities here are the same as those found in Figure 7.9.

7.4.1 Excluding the Torsional Alfvén Wave Condition

Not surprisingly, the effect of self-gravity is to keep the filament together against the centrifugal force. In the absence of significant self-gravity, ρ often tends to increase with radius and may exceed ρ_0 due to rotation, which is not realistic for a filament that eventually merges with the ISM. Several solutions of this type can be seen in Figures 7.2 and 7.8. Typically, this behaviour is associated with strong rotation and weak toroidal magnetic fields. However, if magnetic stresses are strong enough, and/or rotation slows within a reasonable radius, then the density profile may decrease. Empirically, if a power law in radius (Equation 7.22) is followed (see Figure 7.8), then a greater Γ_ϕ/Ω_0 ratio tends to keep $\rho < \rho_0$ and $\mathrm{d}\rho/\mathrm{d}r < 0$. The effect of Γ_z does not seem to be as significant compared to Γ_ϕ and Ω_0, unless Γ_z is large. These features can be seen in Figure 7.8.

If the flux power law of rotation (Equation 7.27) is followed (see Figure 7.8) with self-gravity neglected, then the value of α_M seems to have a dominating effect on the behaviour of $\rho(r)$. There are density profiles where $\rho > \rho_0$, regardless of the value of α_M. A larger portion of these models exceed ρ_0 as α_M becomes steeper. All of these models, except where $\Gamma_\phi = 0$, decrease in density as r becomes large. The Γ_ϕ/Ω_0 ratio has a similar effect as in the models that follow Equation 7.22. See Figure 7.8 for the associated density profiles.

Density Inversions

Density inversions are found in some models where $\rho(r) < \rho_0$ (for all r), but curiously only if self-gravity is included, and the field angle constraint in Equation 7.36 is excluded. An important difference between our models, and the models of Hansen et al. (1976) and Recchi et al. (2014) is the inclusion of magnetic fields. Even without the constraint of torsional Alfvén waves (Equation 7.36), if there are constant poloidal and toroidal magnetic fields, then density inversions can still be observed as long as Γ_ϕ is weak.

It is easier to see the effects due to $\Omega_0 = \Omega(r)$, Γ_ϕ, and Γ_z, by first assuming that they are

constant. The effect of increasing Γ_ϕ is to dampen the density inversions (see Figure 7.7). As Ω_0 increases, the entire density profile along with the inversions, shifts to greater densities, and the inversion amplitude decreases slightly. The effect of increasing Γ_z is that the density inversions tend to occur at larger radii as if each inversion was shifted over, and with larger amplitude. The toroidal flux-to-mass ratio Γ_ϕ seems to have a more noticeable effect on the behaviour of ρ than Γ_z. Generally, Γ_ϕ and Γ_z behave as Fiege & Pudritz (2000*a*) describe – Γ_z tends to support/radially extend the filament compared to the Ostriker solution, while Γ_ϕ pinches the filament. These effects can still be seen even with density inversions occurring (see Figure 7.7).

Density inversions exist in solutions where the rotation follows the radial power law of Equation 7.22 (see Figure 7.7), and for those that follow the flux power law of Equation 7.27. At large radii, the density decreases like a power law for $-1 \leq \alpha < 0$. The general behaviour of the density inversions for both rotation laws is similar. There *is* a subtle difference in that the inversions following the flux power law seem to exhibit a smaller frequency and features are stretched over a slightly larger radius than those that follow Equation 7.22. While a particular model may exhibit density inversions, it is only realistic if it is pressure truncated before any inversions are observed.

7.4.2 Including the Torsional Alfvén Wave Condition

Self-gravitating filaments following the radial power law of Equation 7.22 all have density profiles that decrease with radius (see Figure 7.1). A steeper power law index tends to cause a steeper decline in density, as seen in Figure 7.1. A large Γ_z/Ω_0 ratio tends to produce steeper solutions initially, but then achieve an asymptotically constant ($\mathrm{d}\rho/\mathrm{d}r \approx 0$) value of ρ at large radii. As α decreases, asymptotic solutions can be seen with smaller Γ_z/Ω_0 ratios. Non-self-gravitating filaments following the same rotation law generally have solutions that are not asymptotic. As α becomes progressively steeper, the density profiles tend to become

more shallow. At $\alpha = -1$, all profiles are truly asymptotically constant at $\rho = \rho_0$. All profiles decrease when $\alpha > -1$.

Models that are self-gravitating and rotate according to the flux power law (Equation 7.27) have decreasing density when $\alpha_M = -0.25$, but more negative values have profiles that were deemed unrealistic because $\rho > \rho_0$ at some point(s) (see Figure 7.2). All profiles begin to decrease at a sufficiently large radius, but the density inversion, where $\mathrm{d}\rho/\mathrm{d}r > 0$, becomes more pronounced as α_M becomes more negative. The existence of this extreme density inversion persists even after numerous tests of the numerical integration. Thus, we deem these models to be physically unrealistic and exclude them. As α_M becomes more negative, the profiles following the flux power law for rotation (Equation 7.27) have a greater frequency of asymptotic solutions where there is a relatively large Γ_z/Ω_0 ratio. The ratio of Γ_z/Ω_0 does not need to be as large to observe asymptotic solutions as α_M decreases. Non-self-gravitating filaments following the same rotation law do not have asymptotic solutions at $\alpha_M = -0.25$, and the density profiles decrease with the radius. Density profiles with $\alpha_M \lesssim -0.50$ were deemed unrealistic due to density inversions that increase the density above ρ_0 at some point(s). This $\alpha_M \approx -0.50$ boundary coincides with the limit of α_M that was stated in Section 7.2.2. More negative values of α_M cause Ω to behave as r^{-1} or steeper, and the filament rotates extremely rapidly near the origin. These models are deemed unrealistic.

Generally, by including the physics of Alfvén waves through the description in Section 7.2.2, we see that the density profiles are better behaved in the sense that the density profiles usually do not increase above ρ_0, the density falls off with the radius, and there are no density inversions. Interestingly, every model that follows the radial power law rotation of Equation 7.22 exhibit $\rho(r) \leq \rho_0$ (or are at least asymptotically constant at $\rho = \rho_0$ when $\alpha = -1$ for non-self-gravitating models), in both self-gravitating and non-self-gravitating cases regardless of any $\alpha < 0$. Furthermore, by including the Alfvén wave constraint (Equation 7.36), every

model that follows the flux power law rotation of Equation 7.27 also exhibit $\rho(r) \leq \rho_0$ in both self-gravitating and non-self-gravitating cases, as long as $\alpha_M > -1/2$. This suggests that the inclusion of Alfvén wave physics is an important factor in the description of molecular tornadoes.

7.4.3 Is Self-Gravity Important?

Self-gravity, magnetic fields, and external pressure have a significant influence on constricting the density profile in our models. On the other hand, rotation, and turbulence tend to increase the density with radius. Interestingly, the observationally constrained models (see Figure 7.10) indicate via Equation 7.39 that, for all models, $\mathcal{M}/|\mathcal{W}| < 0$. This is not surprising since we have noticed the pinching effect that magnetic fields have on density profiles (see Section 7.4.1, Figure 7.8), and the magnetic-squeezing/twisting mechanism that is proposed by Morris et al. (2006), Sofue (2007), Matsumura et al. (2012).

Having found the relative energies via our virial analysis (see Section 7.3), $\mathcal{W}$ is compared to $\mathcal{M}$ and $\mathcal{K}_P$, which are the quantities that can help keep the filament structure bound, to see which terms are particularly important. An example of these comparisons is shown in Figure 7.9 for the self-gravitating model with the torsional Alfvén wave constraint of Equation 7.36, and radial power law of Equation 7.22 with $\alpha = -0.25$. The magnetic energy ratio with gravitational energy within observational constraints is found to be $-10^5 \lesssim \mathcal{M}/|\mathcal{W}| \lesssim 0$, which suggests that the magnetic field may be much more important than self-gravity. Furthermore, the ratio of the surface pressure to gravitational energy across all self-gravitating models within observational constraints is $10^0 \lesssim |\mathcal{K}_P|/|\mathcal{W}| \lesssim 10^3$, which further indicates that these molecular tornadoes are only weakly self-gravitating. It is also found that $|\mathcal{M}| > |\mathcal{K}_P|$ for most models within observational constraints, as shown in Figure 7.10. Thus, the toroidal magnetic field confinement is more important than the surface pressure, and both are more important than self-gravity. This result is similar to the interpretation

by Sofue (2007), who considered the magnetic tension to be a significant component, and did not focus on the external pressure. Knowing this, the approximation $\mathcal{W} \approx 0$ may be justified. If the toroidal magnetic stress is dominant, Equation 7.39 may best be rewritten as

$$\frac{|\mathcal{K}_P|}{\mathcal{M}} = \frac{\mathcal{K}_{rot} + \mathcal{K}_\sigma}{\mathcal{M}} + \frac{1}{2}, \tag{7.54}$$

where it is easier to see that if $\mathcal{M} < 0$ then $(\mathcal{K}_{rot} + \mathcal{K}_\sigma) < -\mathcal{M}/2$, and if $\mathcal{M} > 0$ then $(\mathcal{K}_{rot} + \mathcal{K}_\sigma) > -\mathcal{M}/2$. It was also found that $|\mathcal{M}| > |\mathcal{K}_P|$, and since models follow $\mathcal{M} < 0$, this means that $(1/2)|\mathcal{M}| < (\mathcal{K}_{rot} + \mathcal{K}_\sigma) < (3/2)|\mathcal{M}|$.

A similar analysis of the DHN and GCT is shown in Figure 7.11. All observationally constrained models of the GCT are dominated by the toroidal magnetic stress component, and the vast majority of models are magnetically dominated over the pressure. This lends support for the magnetic squeezing model by Sofue (2007). Analysis suggests that the dominant component of the DHN is not clear – pressure or magnetic stresses may dominate. Comparison between $|\mathcal{M}|$ and $|\mathcal{K}_P|$ for the DHN reveals that more of the constrained models are magnetically dominated, though the dominating component cannot be conclusively determined. This uncertainty is likely due to estimating Ω_S By the torsional Alfvén wave condition (Equation 7.36), and as seen in Figures 7.9 and 7.11, rotation and the toroidal magnetic stress are directly proportional. A more accurate method of estimating the equilibrium filament radius would help constrain Ω_S, and therefore, determine whether magnetic or pressure terms dominate. If the rotation had instead been estimated by the Shafranov condition (Equation 7.41c), then a much faster rotation would have been resulted. This would increase $|\mathcal{K}_{rot}|$, and would then require a much stronger $|\mathcal{M}|$ to satisfy the virial relation. Thus, the DHN would convincingly be magnetically dominated. It is highly suggestive, however, that both the DHN and GCT are weakly self-gravitating, like the Pigtail Molecular Cloud. We do not analyze the results of the DHN and GCT in detail as the observational

constraints carry significant uncertainty associated with observational measurements.

7.5 Summary

Molecular tornadoes are fascinating objects that reside in the extreme environment of the CMZ. We study equilibrium MHD models of molecular tornadoes and introduce different rotation laws (see Section 7.2.2), reasonably general helical magnetic fields (Equations 7.5 and 7.7), external pressures, and consider an isothermal equation of state.

1. The physics of torsional Alfvén waves was introduced in Section 7.2.2, which led to a constraint on the magnetic field components (Equation 7.35), and between Γ_ϕ and Ω (Equation 7.36). This constraint leads to solutions that are generally more well-behaved than solutions excluding the torsional Alfvén wave condition – in the sense that their density profiles do not increase indefinitely, and there are no density inversions. We conclude that including torsional Alfvén wave physics is an important component in a realistic model of molecular tornado structure.

2. A special analytical solution, where centrifugal forces balanced exactly with toroidal magnetic stresses, was explored. The solution also assumes that the ratio between the pressure (from the isothermal equation of state) and the magnetic stresses, is constant (Equation 7.10, and 7.11). These assumptions leads to solutions that are rescaled versions of the Ostriker solution, with constant rotational velocity of the filament (Equation 7.21).

3. A Monte Carlo analysis of our models was conducted to explore the associated parameter space. Our models are constrained by limited observable constraints via Equation 7.45. We focus our analysis on the Pigtail Molecular Cloud whose observational properties are more conclusively measured. Our analysis suggests that external pressures

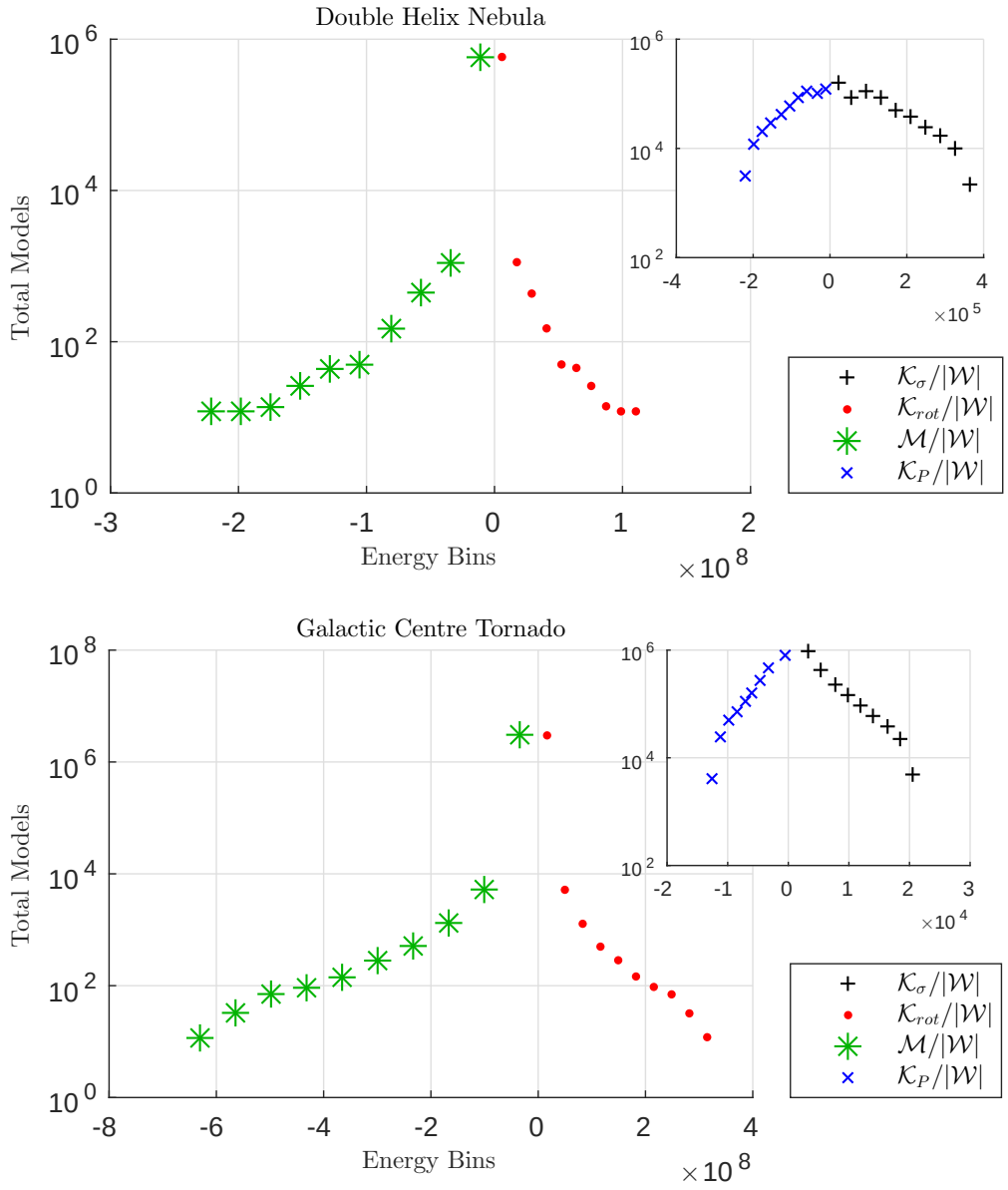

Figure 7.11: DHN (top) and GCT (bottom) histograms analogous to Figure 7.9.

are important in its equilibrium structure (see Figure 7.10).

4. We performed a study of the virial theorem and found that, within observational constraints for the Pigtail,

$$-10^5 \lesssim \frac{\mathcal{M}}{|\mathcal{W}|} \lesssim 0,$$
$$10^0 \lesssim \frac{|\mathcal{K}_P|}{|\mathcal{W}|} \lesssim 10^3,$$

and

$$|\mathcal{M}| > |\mathcal{K}_P|.$$

Thus, the confinement of magnetic fields dominates external pressure, which dominates self-gravity. We conclude that self-gravity is relatively unimportant in the equilibrium structure of molecular tornadoes. The relatively large values of $\mathcal{M}/|\mathcal{W}|$ and $|\mathcal{K}_P|/|\mathcal{W}|$ are due to the weakness of self-gravity. Since $\mathcal{M}/|\mathcal{W}| < 0$, the magnetic field is dominated by the toroidal component, which lends support for the proposed magnetic-squeezing/twisting mechanism of molecular tornadoes.

5. We performed the same analysis for the DHN and GCT as we did for the Pigtail, but the conclusions we draw should be taken with more caution for these objects. Our analysis seems to suggest, however, that the GCT is dominated by the toroidal magnetic stress, whereas the DHN may be dominated by the pressure and/or magnetic stress. Self-gravity is relatively unimportant in these molecular tornadoes as well.

7.6 Acknowledgements

K.A. would like to acknowledge Tomoharu Oka, Mark Morris, and Yoshiaki Sofue for their insights and interpretations on the Pigtail Molecular Cloud, DHN, and GCT, respectively. J.D.F. acknowledges the support of a Discovery Grant from the National Sciences and En-

gineering Research Council of Canada.

7.7 Appendix

We assume a torsional Alfvén wave of the form $B_\phi = B_{\phi,0}\mathrm{e}^{-i(kz-\omega t)}$ and $v_\phi = v_{\phi,0}\mathrm{e}^{-i(kz-\omega t)}$, where $B_{\phi,0}$ and $v_{\phi,0}$ are the corresponding amplitudes, k is the wave number, and ω is the angular frequency of the perturbation. Notice that the differential operators ∂_t and $\boldsymbol{\nabla}$ become $\partial_t \rightarrow i\omega$ and $\boldsymbol{\nabla} \rightarrow -ik\hat{z}$ when they act on the perturbed terms. By linearizing Faraday's Law, it becomes

$$\omega B_\phi = -kB_z v_\phi. \tag{7.55}$$

Since the perturbations are small, it can be shown from the wave equation (Equation 7.30) that

$$v_A^2 = \frac{\omega^2}{k^2}, \tag{7.56}$$

so Equation 7.55 can be simplified to

$$\frac{B_{\phi,1}}{B_{z,0}} = \frac{v_{\phi,1}}{v_A}, \tag{7.57}$$

which is identical to Equation 7.35. Thus, the torsional Alfvén wave condition (Equation 7.36) follows.

Chapter 8

Phase Diagrams of Self-Gravitating, Nonmagnetic, Rotating Cylinders

The existence of solutions displaying density inversions in Hansen et al. (1976), Recchi et al. (2014), Au & Fiege (2017) is surprising and unexpected since such density profiles are not observed in reality (Palmeirim et al. 2013, for example). Solutions that ultimately lead to an inversion may still be valid and describe real molecular filaments as long as the external pressure truncates the radial density profile at a radius smaller than the radius of the first inversion (Recchi et al. 2014, Au & Fiege 2017). Au & Fiege (2017) presented solutions with density inversions observed for certain ranges of the parameter space. Here, we present a set of "phase diagrams" for self-gravitating, nonmagnetized rotating filaments to more completely explore and better understand this phenomenon.

Density inversions are observed in the Au & Fiege (2017) solutions, which included those with very weak magnetic fields, and relatively slow rotation. An interesting result from Au & Fiege (2017) is that solutions did not exhibit density inversions when a torsional Alfvén wave condition was included in their models. This torsional Alfvén wave condition related the pitch angle of a helical magnetic field with the ratio of toroidal and poloidal

components of the magnetic field, and with the ratio of rotational and Alfvén speeds. Such a condition is important for describing real molecular tornadoes – molecular filaments with helical morphology in the Galactic Centre (Morris et al. 2006, Sofue 2007, Matsumura et al. 2012, Au & Fiege 2017). Strictly isothermal models were considered in the exploration by Au & Fiege (2017). The equation of state (EOS) is now relaxed, the magnetic fields are now absent, and the torsional Alfvén wave condition is removed in order to explore the most simple solution space behavior for rotating, self-gravitating cylinders.

The polytropic EOS behaves as $P \propto \rho^{\gamma}$, where γ is the *polytrope exponent*, which is related to the *polytrope index* $n = 1/(\gamma - 1)$. An isothermal EOS is characterized by $P = \sigma^2 \rho$, which corresponds to $\gamma = 1$. An isothermal EOS is often used for molecular clouds (McKee & Holliman 1999), although it may be considered "hard" relative to some other EOSs. In reality, the effects of turbulence tend to soften the effective EOS (Fiege & Pudritz 2000*a*, and references therein). For example, MHD turbulence varies the internal pressure within a fixed volume. Pure molecular cloud support by internal turbulent pressure is described by the EOS $P \propto \rho^{1/2}$ (McKee & Zweibel 1995). An adiabatic index of $\gamma = 3/2$ may be more appropriate when the turbulent pressure changes adiabatically (McKee & Zweibel 1995). The softest EOS in the literature is that of the logatropic EOS (McLaughlin & Pudritz 1996, Fiege & Pudritz 2000*a*).

8.1 Theory

Much of the mathematical framework of our models was established by Au & Fiege (2017), and we remain consistent with their notation and formulation. This work is performed in the same dimensionless quantities as in Au & Fiege (2017). Hereafter, all quantities are assumed to be dimensionless unless ambiguity should arise, in which case dimensionless quantities are explicitly represented by an overscript tilde. Our models assume cylindrical

geometry described by the (r, ϕ, z) set of coordinates.

8.1.1 Rotation

Differential rotation in the form of a radial power law is considered. The angular frequency of rotation Ω is described by

$$\Omega = \Omega_0 \left(\frac{r}{r_0} \right)^{\alpha}, \tag{8.1}$$

where the r is the radius, and α is the power law index. The subscript 0 notation denotes quantities at the filament's radial core ($r = 0$). The power law index is limited by the case of solid body rotation $\alpha = 0$ and a "Keplerian-like" limit that behaves as $\alpha = -1$, such that $-1 \leq \alpha \leq 0$. This rotation law was also used in Au & Fiege (2017).

8.1.2 Incorporating Different Equations of State

The MHD models of molecular tornadoes considered by Au & Fiege (2017) had an isothermal EOS, which combined both thermal and nonthermal components such that

$$P = \sigma^2 \rho, \tag{8.2}$$

where P is the pressure, ρ is the density, and $\sigma = \sqrt{\sigma^2_{thermal} + \sigma^2_{nonthermal}}$ is the constant total velocity dispersion.

We now consider other equations of state such as the polytrope EOS from Fiege & Pudritz (2000*a*) and apply it to the framework formulated by Au & Fiege (2017). The polytrope EOS is given by

$$\frac{P}{P_0} = \left(\frac{\rho}{\rho_0} \right)^{\gamma}, \tag{8.3}$$

where P is the pressure. Under the same assumptions as Au & Fiege (2017), the MHD equations with a polytrope EOS (Equation 8.3) result in a general expression for the radial

density:

$$\frac{\mathrm{d}\rho}{\mathrm{d}r} = \frac{\rho g + \rho\Omega^2 r - \frac{1}{2\pi} r\rho^2\Gamma_\phi^2 - \frac{1}{8\pi} r^2\rho^2 \frac{\partial}{\partial r}\Gamma_\phi^2 - \frac{1}{8\pi}\rho^2\frac{\partial}{\partial r}\Gamma_z^2}{\gamma\rho^{\gamma-1} + \frac{1}{4\pi} r^2\rho\Gamma_\phi^2 + \frac{1}{4\pi}\rho\Gamma_z^2}, \tag{8.4}$$

where the gravitational field is defined by $g(r) := -\partial\Phi(r)/\partial r$, and $\Phi(r)$ is the gravitational potential as described by Poisson's equation for gravity, $\Gamma_z = B_z/\rho$ is the poloidal flux-to-mass ratio with poloidal magnetic field B_z, and $\Gamma_\phi = B_\phi/r\rho$ is the toroidal flux-to-mass with toroidal magnetic field B_ϕ.

The logatrope EOS is characterized by

$$\frac{P}{P_0} = 1 + A\log\left(\frac{\rho}{\rho_0}\right), \tag{8.5}$$

(McLaughlin & Pudritz 1996, Fiege & Pudritz 2000*a*) where A is a constant. McLaughlin & Pudritz (1996) found $A \simeq 0.2$ for molecular cloud cores, which Fiege & Pudritz (2000*a*) assumed for their logatropic molecular filaments. We also adopt $A \simeq 0.2$ in our self-gravitating, nonmagnetic rotating cylinder model. Following a similar derivation to obtain Equation 8.4, the radial density for the polytrope is given by:

$$\frac{\mathrm{d}\rho}{\mathrm{d}r} = \frac{\rho g + \rho\Omega^2 r - \frac{1}{2\pi} r\rho^2\Gamma_\phi^2 - \frac{1}{8\pi} r^2\rho^2 \frac{\partial}{\partial r}\Gamma_\phi^2 - \frac{1}{8\pi}\rho^2\frac{\partial}{\partial r}\Gamma_z^2}{A\rho^{-1} + \frac{1}{4\pi} r^2\rho\Gamma_\phi^2 + \frac{1}{4\pi}\rho\Gamma_z^2}, \tag{8.6}$$

Since magnetic fields are absent in this analysis, Equations 8.4 and 8.6 can be trivially simplified further, but the form is currently shown as is for generality and to draw comparison with the isothermal case in Au & Fiege (2017). From Equation 8.4, it is more easily seen that the logatrope case in Equation 8.6 is similar to the specific case when $\gamma = 0$.

8.2 Computational Methods

Numerically computed solutions are integrated with ode45 in MATLAB, a Runge-Kutta 4-5 integrator. The initial values in computing solutions to $\mathrm{d}\rho/\mathrm{d}r$ cannot begin precisely at $r = 0$ given the numerical nature of the problem. To account for this error, a tolerance of $10^{-6}\rho_0$ is included to discern solutions that may have increasing densities (density inversions) above ρ_0 and those that do not rather than strictly ρ_0.

Density inversion events can be accurately triggered when the power law index $\alpha_r := \mathrm{d}\log(\rho)/\mathrm{d}\log(r) > 0$, where $\rho \sim r^{\alpha_r}$. A zero-crossing of α_r from negative to positive values is clear evidence of a density inversion.

A "squashing" transformation outlined in Au & Fiege (2017) transforms the dimensionless radius to another dimensionless quantity by $\xi \equiv \ln(r)$. This transformation is useful in computing solutions out to large values of radius.

It is also useful to distinguish between solutions that self-truncate, and those that do not. This criterion is met when the density goes to zero. Self-truncating solutions are triggered by the "events" function of ode45 when the density reaches zero from positive density. Although negative densities are unphysical, they can be *numerically* calculated for the purpose of accurately detecting self-truncating solutions when the density encounters a zero crossing. Solutions to the polytrope radial density described by Equation 8.4 are imaginary when the integration continues to negative density values due to the polytrope exponent γ, which can be fractional. In other words, raising a negative quantity (ρ in this case) to a fractional exponent (γ) results in an imaginary quantity. This is problematic since a self-truncating solution is detected by the "events" function when the density transitions from positive to negative, not to imaginary quantities. To resolve this problem and detect the zero density crossing, the fractional power of negative densities were calculated by $-|\rho|^{\gamma-1}$ in place of $\rho^{\gamma-1}$, which retains the sign of ρ, but still computes a real value. This is a numerical

trick that accurately finds the truncation radius without affecting the truncated solution.

For hard EOSs, the density can change rapidly – self-truncating discontinuously at the filament surface (discussed further in Section 8.4). Rapidly changing solutions can be difficult to numerically integrate so numerical integration of Equation 8.4 was done in terms of pressure ($\mathrm{d}P/\mathrm{d}r$), which is continuous across the filament boundary and does not change as rapidly as ρ does. Via the EOS, P can be transformed back to ρ for analysis. This technique is particularly useful for hard EOSs that steeply truncate as shown in the incompressible limit phase diagram in Section 8.3 and discussed in Section 8.4.

8.3 Results

Both the rotational power law index α and the polytrope exponent γ are varied in this exploration. Given the variation in the polytrope exponent, a conservative range $0 \leq \gamma \leq 2$ is considered for somewhat more realistic EOSs. The solutions for $\gamma = 0$ are mapped to the logatropic EOS, which is similar to the $\gamma = 0$ limit. These are highlighted in a separate column of the solution space in Figure 8.1. Solutions approaching the incompressible limit ($\gamma \gg 1$) are also investigated for interest and shown in Figure 8.2. Additionally, the rotational radial power law index described by Au & Fiege (2017) is varied in the range $-1 \leq \alpha \leq 0$ as described by the bounds in Section 8.1.1. Au & Fiege (2017) already observed density inversions in their solutions with the axial angular frequency Ω_0 on the order of $\sim 10^{-2}$. This is used as a guideline to test a range of Ω_0 values and in analyzing the varying rotational power law index and polytrope index space of solutions.

The solution space to the MHD equations is presented as a function of varying α, γ, and Ω_0. In total there are five distinguishing categories of solutions corresponding to five different colours in Figures 8.1 and 8.2. This colour correspondence is as follows:

1. Black: density inversions above the central density i.e. $\rho(r) > \rho_0$, $\alpha_r > 0$, $\rho(r) \neq 0$;

2. Red: density inversions below the central density that self-truncate i.e. $\rho(r) < \rho_0$, $\alpha_r > 0$, $\rho = 0$;

3. Green: density inversions below the central density that do not self-truncate i.e. $\rho(r) < \rho_0$, $\alpha_r > 0$, $\rho(r) \neq 0$;

4. Blue: no density inversions below the central density and self-truncate i.e. $\rho(r) < \rho_0$, $\alpha_r < 0$, $\rho = 0$; and

5. White: no density inversions below the central density and do not self-truncate i.e. $\rho(r) < \rho_0$, $\alpha_r < 0$, $\rho(r) \neq 0$.

The analysis is conducted in the range $10^{-6} \leq r \leq 10^6$. It is worth noting that the behaviour of these theoretical solutions beyond $r = 10^6$ are not considered. For example, perhaps some solutions that exhibit no density inversions in the $10^{-6} \leq r \leq 10^6$, but have density inversions at $r > 10^6$. For all practical purposes however, $10^{-6} \leq r \leq 10^6$ is a sufficiently large range for this study. More realistically, the density and pressure at such large radii would be very low and there is always some finite amount of external pressure, which would lead to truncation anyway.

8.4 Discussion

When there is no rotation, there are two "phases" seen in Figure 8.1. The first type of solution seen are solutions with no density inversions observed and do not self-truncate, which correspond to the white region. The second type seen are solutions also with no density inversions observed, but *do* self-truncate indicated by the blue region. These two regions are separated by $\gamma \gtrsim 1$, which is approximately the isothermal EOS. This is not surprising since the nonrotating, nonmagnetized, isothermal cylinder solutions of Ostriker (1964) do not self-truncate. A similar solution space is also apparent for slowly rotating

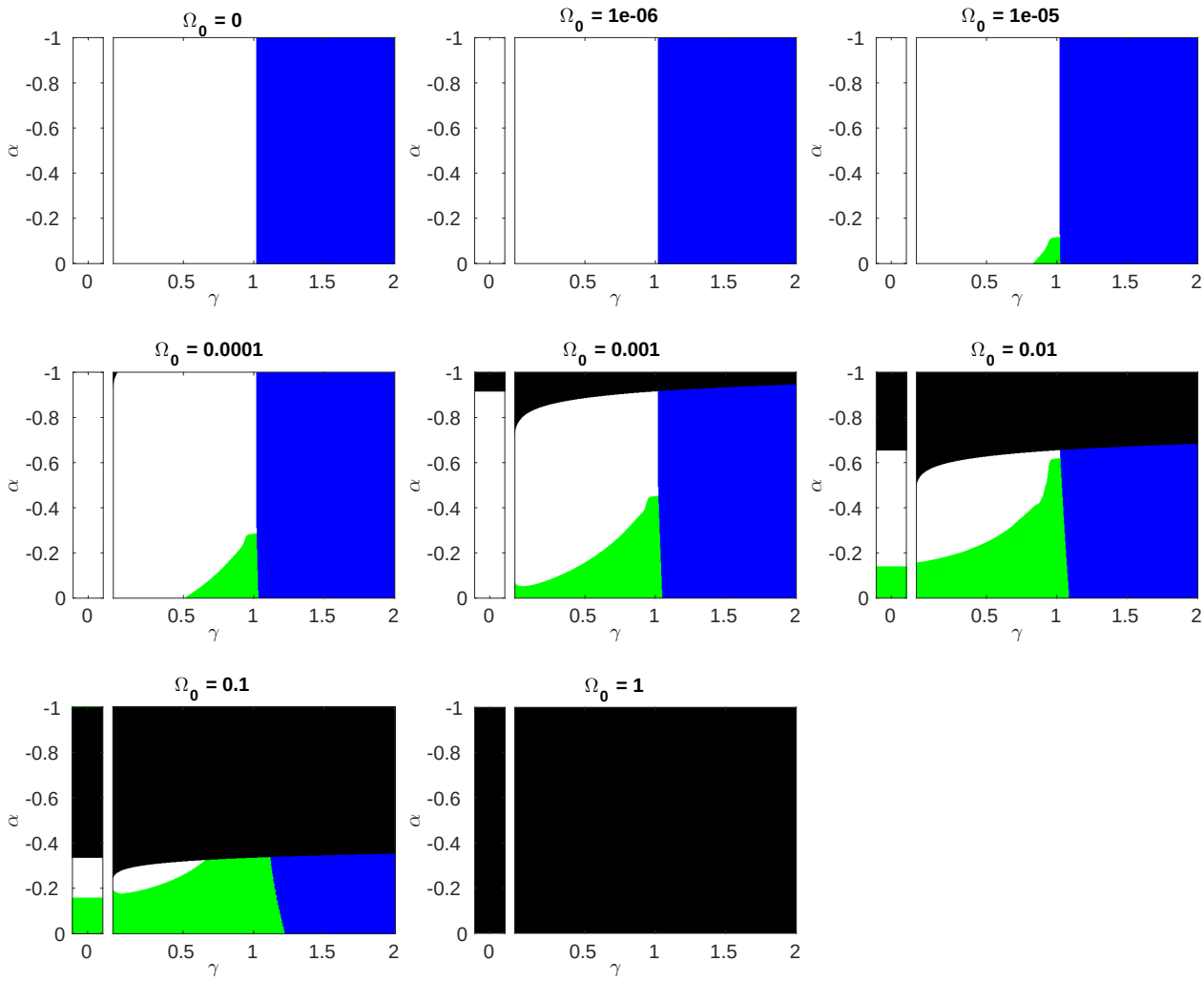

Figure 8.1: Solution space of nonmagnetized, rotating self-gravitating cylinders between polytropic index $0 \leq \gamma \leq 2$. Solution colour correspondance is as follows: **Black**: inversions above ρ_0; **Red**: self-truncating with inversions below ρ_0; **Green**: non-self-truncating with inversions below ρ_0; **Blue**: self-truncating with no inversions; **White**: non-self-truncating with no inversions.

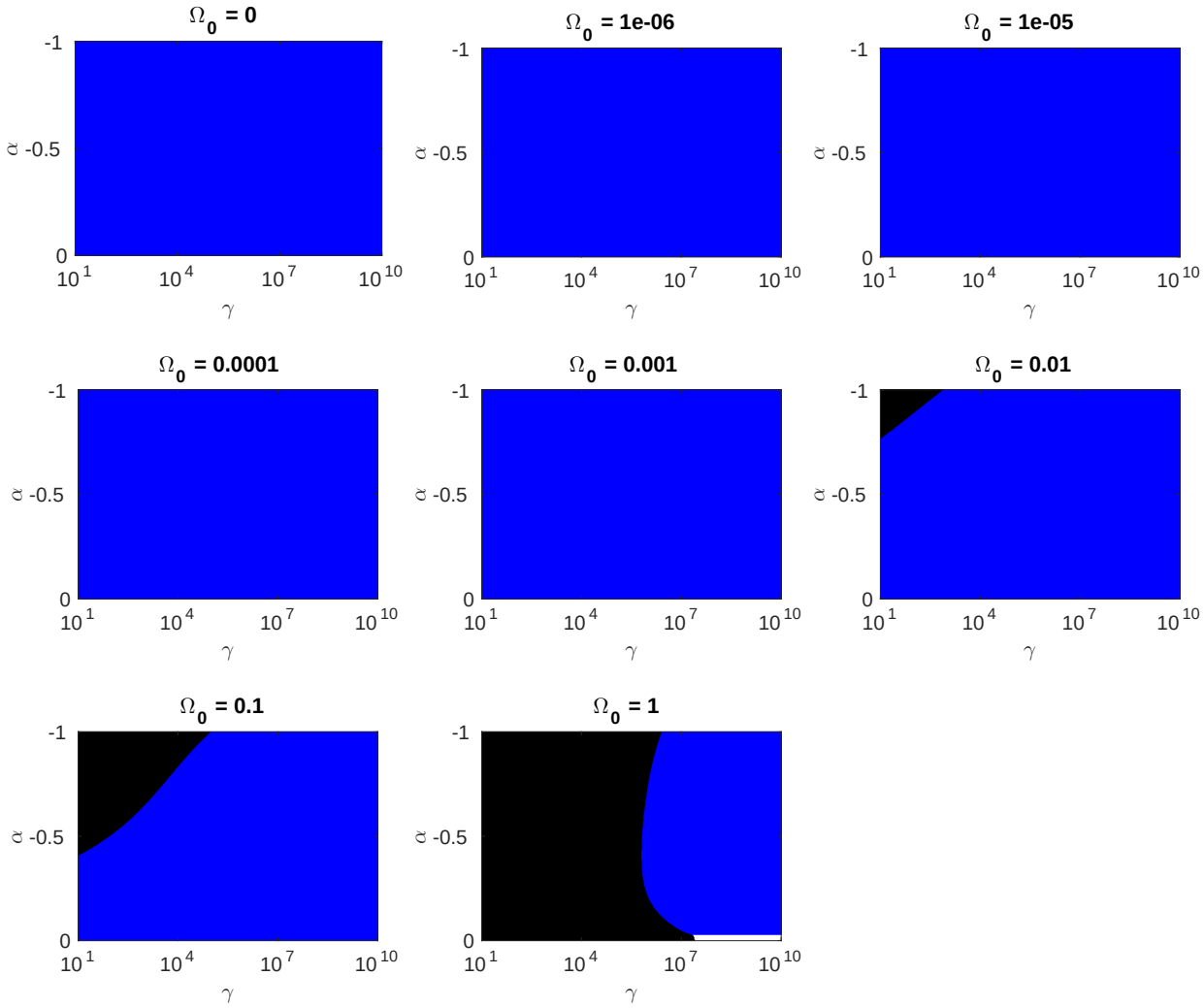

Figure 8.2: Solution space of nonmagnetized, rotating selfgravitating cylinders in the limit of $\gamma \gg 1$. Colour correspondance is the same as Figure 8.1. The patch of white in the $\Omega_0 = 1$ panel near $\alpha \gtrsim 0$ and $10^7 \lesssim \gamma \leq 10^{10}$ is an artifact where $\rho_0 \leq \rho(r) \leq \rho_0 + 10^{-6}\rho_0$ for the integrated range (see Section 8.4).

filaments in the uppermost right panel of Figure 8.1, where $\Omega_0 = 10^{-6}$. As the cylinder begins to rotate more quickly, however, a new type of solution is introduced as seen in the $\Omega_0 = 10^{-5}$ panel of Figure 8.1. These new solutions are indicated by the colour green and correspond to solutions that exhibit density inversions below the core density and do not self-truncate. Interestingly, such solutions first appear around the isothermal polytrope exponent. By $\Omega_0 = 10^{-4}$, the uppermost left corner of the solution space where $\alpha \simeq 1$ and $\gamma \gtrsim 0$ reveals solutions that observe density inversions that increase above the central density. Such solutions have not been observed (if not rarely occurring) in molecular filaments. It would seem that rotation dominates self-gravity more easily in softer EOSs. Furthermore, self-truncating solutions with no density inversions (indicated by blue) begin to recede in the solution space in the sense that at smaller magnitude α, these solutions are confined to larger magnitude γ. Building rotation speed, non-self-truncating solutions with density inversions below the central density, and solutions with inversions above the central density begin to encompass a larger portion of the solution space – expanding to include a larger range of α and γ at the expense of those solutions that exhibit no density inversions and do not self-truncate, and those with no density inversions and do self-truncate. In other words, as rotation increases, a larger portion of the solution space contains density inversions. By $\Omega_0 = 1$, the entire solution space is dominated by rotation and the cylinders always increase in density above the central density.

As α approaches zero, solutions are separated into those solutions with no density inversions and self-truncate ($\gamma \gtrsim 1$), and do not self-truncate ($\gamma \lesssim 1$). With increasing rotation, solutions with inversions above the central density are first encountered followed by those solutions that do not have inversions. Near the isothermal polytrope exponent though, this margin narrows with those solutions that have density inversions and are not self-truncating. There is also a slight curve in the phase of solutions that increase above the central density, with a wider range of α toward softer EOSs. Firstly, a steep α index implies that

axial rotation of the cylinder is very high, causing density inversions. Secondly, the density characterized by a softer EOS is more easily influenced by other physical conditions such as rotation.

By increasing γ, solutions generally go from those that do not self-truncate to those that do. In the absence (or near absence) of rotation, self-truncating solutions first occur around $\gamma \approx 1.001$. The transition from non-self-truncating to self-truncating solutions can be explained directly from the polytropic EOS (Equation 8.3). A harder EOS implies that a slight change in density increases the pressure significantly, while a change in density of a softer EOS will have a much smaller effect on the pressure. This is also true even if there is no rotation.

The limit of $\gamma \gg 1$ approaches the case for an incompressible cylinder shown in the solution of Figure 8.2. It is seen from the figure panels that the incompressible limit only contains solutions with no density inversions and self-truncation. The solutions where density inversions increase above the central density due to rotation, as seen in the relatively smaller values of γ in Figure 8.1, eventually disappear from the space of solutions. It should be noted that there is an artifact that appears in the $\Omega_0 = 1$ panel of Figure 8.2. This artifact is due to the density increasing above ρ_0, but staying below the $\rho_0 + 10^{-6}\rho_0$ threshold for those solutions that appear black in the phase diagrams of Figure 8.2. These solutions are not detected to have density inversions since they are always increasing such that $\alpha_r > 0$ and they do not self-truncate since the density lies between ρ_0 and $\rho_0 + 10^{-6}\rho_0$. Thus, these density profiles meet the criteria for those solutions that have no density inversions and do not self-truncate, even though they do not behave as $\alpha_r < 0$ as such self-gravitating density profiles should. These solutions with $\gamma \gg 1$ are not realistic in terms of real filaments, but are interesting to explore because they compliment the stability study of incompressible cylinders by Chandrasekhar & Fermi (1953*b*).

Like the polytrope solution space, logatrope solutions exhibit density inversions where

the peak density in the inversion may exceed the central density with increasing α and rotational frequency. Likewise, a wider range of α exhibits density inversions that do not self-truncate with increasing rotation. An important difference to observe is that logatrope solutions never self-truncate according to this analysis, which is likely attributed to it being a very soft EOS.

It is worth mentioning that solutions with density inversions below the central density that self-truncate (coloured red) are not found in any of the phase diagrams. This is due to the strict criterion for self-truncation – that the solutions must reach zero density to qualify as a self-truncating solution. For those solutions that do not self-truncate, there are often cases where first inversion reaches the lowest density out of subsequent inversions (Au & Fiege 2017, Figure 5 for example). If the first inversion reaches zero density then this is where self-truncation occurs, and subsequent inversions would not be observed. Thus, these solutions would qualify as self-truncating solutions without density inversions.

This solution space exploration is complimentary to a study like that of Au & Fiege (2017) in modelling cylindrical models of molecular filaments. Constructing phase diagrams helps to further confine the possible parameter space where solutions for realistic filaments may exist. In particular, it may help to identify or bound the polytrope exponent and the EOS of molecular filaments provided that the rotation can be modelled or measured to determine the rotational radial power law index. Solutions that rotate at a very fast rate must be excluded from such models. Furthermore, there are solutions exhibiting density inversions below the central density that must be pressure truncated in order to be realistic (Recchi et al. 2014, Au & Fiege 2017). In addition to observational constraints (Au & Fiege 2017), the models which are realistic can further be constrained.

8.5 Conclusion

We found numerical solutions for self-gravitating, nonmagnetized rotating cylinders, in order to study the phenomenon of density inversions for a variety of rotation laws, rotation speeds, and EOSs. Such a solution space exploration is useful for constraining rotation laws, speeds, and EOSs, since density inversions have not been observed in nature. The rotational radial power law index α was varied along with the polytrope exponent γ where the logatrope EOS is taken as an analog of the $\gamma = 0$ case. Of particular interest are those solutions that exhibit density inversions, but five different types of solution behaviours were found and classified:

1. density inversions above the central density;
2. density inversions below the central density that self-truncate;
3. density inversions below the central density that do not self-truncate;
4. no density inversions below the central density, with self-truncation;
5. no density inversions below the central density, without self-truncation.

It was found that solutions with density inversions below the central density appear most often at polytrope exponents near the isothermal EOS. A greater portion of solutions exhibit density inversions (both above and below the central density) with increasing rotation.

Chapter 9

Discussion and Concluding Remarks

Magnetohydrodynamic models of molecular tornadoes were explored in Chapter 7. This is a comprehensive study that incorporates a considerable extent of physically realistic conditions and parameters that included differential rotation in the form of two different rotation laws, generally helical magnetic field configurations, a realistic torsional Alfvén wave constraint, and external pressure truncation. A Monte Carlo exploration provides a thorough exploration of the model parameter space, which is constrained by the observed properties of three molecular tornadoes using three dimensionless constraints. Relative energies of kinetic, self-gravity, and magnetic components are analyzed via a virial analysis to determine the dominating components of these observationally constrained models. Despite the thoroughness of this investigation, there remain improvements that can be made to the analysis. Most notably, the detection and measurement of filamentary rotation in these molecular tornadoes would further constrain the parameter space. This exploration is limited by the observations for this new class of objects and rotation measurements have not yet been conducted. Without a measurement of rotation, the rotation speed can only be speculated either by the proposed shearing mechanism or by the Shafranov conditions, which do not precisely describe the physics of molecular tornadoes. With such a measurement, the Shafra-

nov conditions imply that there may be some contribution from the rotation as to what type of MHD instabilities are observed. Hopefully this work motivates improved observations of these objects in the future.

Beyond the current study of these equilibrium models is an analysis of the instabilities. A stability analysis would explore nonaxisymmetric instabilities such as the $m = 0, 1, 2$ modes observed in molecular tornadoes. An interesting question to address is: *which mode of instability is dominant?* The Shafranov conditions suggest that $m = 1$ instabilities should be observed at slower rotation speeds than $m = 2$ instabilities. Does this mean that there is a preference for $m = 1$ instabilities even when $m = 2$ instabilities are possible? Perhaps the Shafranov conditions do not apply to molecular tornadoes and the instablity conditions do not proceed in such an order. The equilibrium models studied here can be used as the foundation for such a stability analysis.

Solutions of self-gravitating, nonmagnetized rotating filaments are studied in Chapter 8. This analysis is complimentary to the study in Chapter 7 because it gives an idea as to how the various solutions of the MHD equations behave. Notably, the isothermal EOS produces a relatively larger portion of solutions with density inversions below the core density for varying power law indices of the radial rotation power law. This is notable especially if real filaments are approximately isothermal. The possibility exists that, without external pressures, perhaps filaments *would* observe density inversions, although this is purely speculative. It is important to note that this exploration would change dramatically by including the confining effects of magnetic fields. As evident in Chapter 7, observationally constrained models are able to spin much faster than $\Omega_0 = 1$.

9.1 Concluding Remarks

This work presents the first theoretical and numerical studies of molecular tornadoes through the framework of MHD. Not only is this work applicable to the equilibrium of molecular tornadoes that observe MHD instabilities, but molecular filaments in general that may not exhibit a helically-wound structure. The model presented in this study is novel as there has not yet been a theoretical filamentary model that incorporates the combined physics of differential rotation, helical magnetic fields, external pressure, and torsional Alfvén wave physics. Self-gravity is not important in the objects. It is found that these objects are highly pressure and magnetically dominated, particularly by the toroidal magnetic field. The torsional Alfvén wave condition is found to be an important description in the equilibrium structure of rotating filaments threaded by magnetic fields. Not only is this the first study to incorporate these effects, but it is the first to consider such filamentary models in the extreme environment in the CMZ by incorporating high external pressures via truncation.

Phase diagrams for self-gravitating, nonmagnetized, rotating cylinders are constructed in order to better understand their behaviour. Rotation is modeled by a radial power law. The polytrope and logatrope equations of state are considered. Phase diagrams are constructed in the parameter space of varying rotational radial power law index, polytrope exponent, and core rotational frequency. Five solution types are distinguished from each other: 1. density inversions above the central density; 2. density inversions below the central that self-truncate; 3. density inversions below the central density that do not self-truncate; 4. no density inversions below the central density that self-truncate; and 5. no density inversions below the central density that do not self-truncate. Solutions with density inversions are proportionally more concentrated around the isothermal EOS. A greater proportion of solutions exhibit density inversions when the axial rotational frequency increases.

This observationally constrained equilibrium study sets the foundation for further sta-

bility analysis to understand the MHD instabilities involved in forming realistic molecular tornadoes. The phase diagrams can be used to constrain the rotational speed and EOS for realistic filaments.

References

Ackermann, M., Ajello, M., Allafort, A., Baldini, L., Ballet, J., Barbiellini, G., Baring, M. G., Bastieri, D., Bechtol, K., Bellazzini, R., Blandford, R. D., Bloom, E. D., Bonamente, E., Borgland, A. W., Bottacini, E., Brandt, T. J., Bregeon, J., Brigida, M., Bruel, P., Buehler, R., Busetto, G., Buson, S., Caliandro, G. A., Cameron, R. A., Caraveo, P. A., Casandjian, J. M., Cecchi, C., Çelik, Ö., Charles, E., Chaty, S., Chaves, R. C. G., Chekhtman, A., Cheung, C. C., Chiang, J., Chiaro, G., Cillis, A. N., Ciprini, S., Claus, R., Cohen-Tanugi, J., Cominsky, L. R., Conrad, J., Corbel, S., Cutini, S., D'Ammando, F., de Angelis, A., de Palma, F., Dermer, C. D., do Couto e Silva, E., Drell, P. S., Drlica-Wagner, A., Falletti, L., Favuzzi, C., Ferrara, E. C., Franckowiak, A., Fukazawa, Y., Funk, S., Fusco, P., Gargano, F., Germani, S., Giglietto, N., Giommi, P., Giordano, F., Giroletti, M., Glanzman, T., Godfrey, G., Grenier, I. A., Grondin, M.-H., Grove, J. E., Guiriec, S., Hadasch, D., Hanabata, Y., Harding, A. K., Hayashida, M., Hayashi, K., Hays, E., Hewitt, J. W., Hill, A. B., Hughes, R. E., Jackson, M. S., Jogler, T., Jóhannesson, G., Johnson, A. S., Kamae, T., Kataoka, J., Katsuta, J., Knödlseder, J., Kuss, M., Lande, J., Larsson, S., Latronico, L., Lemoine-Goumard, M., Longo, F., Loparco, F., Lovellette, M. N., Lubrano, P., Madejski, G. M., Massaro, F., Mayer, M., Mazziotta, M. N., McEnery, J. E., Mehault, J., Michelson, P. F., Mignani, R. P., Mitthumsiri, W., Mizuno, T., Moiseev, A. A., Monzani, M. E., Morselli, A., Moskalenko, I. V., Murgia, S., Nakamori, T., Nemmen, R., Nuss, E., Ohno, M., Ohsugi, T., Omodei, N., Orienti, M., Orlando, E., Ormes, J. F.,

Paneque, D., Perkins, J. S., Pesce-Rollins, M., Piron, F., Pivato, G., Rainò, S., Rando, R., Razzano, M., Razzaque, S., Reimer, A., Reimer, O., Ritz, S., Romoli, C., Sánchez-Conde, M., Schulz, A., Sgrò, C., Simeon, P. E., Siskind, E. J., Smith, D. A., Spandre, G., Spinelli, P., Stecker, F. W., Strong, A. W., Suson, D. J., Tajima, H., Takahashi, H., Takahashi, T., Tanaka, T., Thayer, J. G., Thayer, J. B., Thompson, D. J., Thorsett, S. E., Tibaldo, L., Tibolla, O., Tinivella, M., Troja, E., Uchiyama, Y., Usher, T. L., Vandenbroucke, J., Vasileiou, V., Vianello, G., Vitale, V., Waite, A. P., Werner, M., Winer, B. L., Wood, K. S., Wood, M., Yamazaki, R., Yang, Z. & Zimmer, S. (2013), 'Detection of the Characteristic Pion-Decay Signature in Supernova Remnants', *Science* **339**, 807–811.

Alves, J. F., Lada, C. J. & Lada, E. A. (2001), 'Internal structure of a cold dark molecular cloud inferred from the extinction of background starlight', *Nature* **409**, 159–161.

Alves, J., Lada, C. J., Lada, E. A., Kenyon, S. J. & Phelps, R. (1998), 'Dust Extinction and Molecular Cloud Structure: L977', *The Astrophysical Journal* **506**, 292–305.

Ao, Y., Henkel, C., Menten, K. M., Requena-Torres, M. A., Stanke, T., Mauersberger, R., Aalto, S., Mühle, S. & Mangum, J. (2013), 'The thermal state of molecular clouds in the Galactic center: evidence for non-photon-driven heating', *Astronomy & Astrophysics* **550**, A135.

Au, K. & Fiege, J. D. (2017), 'Magnetohydrodynamic Models of Molecular Tornadoes', *The Astrophysical Journal* **843**, 107.

Bally, J., Stark, A. A., Wilson, R. W. & Henkel, C. (1987), 'Galactic center molecular clouds. I - Spatial and spatial-velocity maps', *The Astrophysical Journal Supplement Series* **65**, 13–82.

Bally, J., Stark, A. A., Wilson, R. W. & Henkel, C. (1988), 'Galactic center molecular clouds. II - Distribution and kinematics', *The Astrophysical Journal* **324**, 223–247.

Beck, R. (2003), 'Magnetic fields in the Milky Way and other spiral galaxies', *ArXiv Astrophysics e-prints* .

Blitz, L. & Shu, F. H. (1980), 'The origin and lifetime of giant molecular cloud complexes', *The Astrophysical Journal* **238**, 148–157.

Bodenheimer, P. H. (2011), *Principles of Star Formation*.

Bolatto, A. D., Leroy, A. K., Rosolowsky, E., Walter, F. & Blitz, L. (2008), 'The Resolved Properties of Extragalactic Giant Molecular Clouds', *The Astrophysical Journal* **686**, 948–965.

Chandrasekhar, S. & Fermi, E. (1953*a*), 'Magnetic Fields in Spiral Arms.', *The Astrophysical Journal* **118**, 113.

Chandrasekhar, S. & Fermi, E. (1953*b*), 'Problems of Gravitational Stability in the Presence of a Magnetic Field.', *The Astrophysical Journal* **118**, 116.

Chuss, D. T., Davidson, J. A., Dotson, J. L., Dowell, C. D., Hildebrand, R. H., Novak, G. & Vaillancourt, J. E. (2003), 'Magnetic Fields in Cool Clouds within the Central 50 Parsecs of the Galaxy', *The Astrophysical Journal* **599**, 1116–1128.

Crutcher, R., Heiles, C. & Troland, T. (2003), Observations of Interstellar Magnetic Fields, *in* E. Falgarone & T. Passot, eds, 'Turbulence and Magnetic Fields in Astrophysics', Vol. 614 of *Lecture Notes in Physics, Berlin Springer Verlag*, pp. 155–181.

Crutcher, R. M. (1994), Observations of Magnetic Fields in Molecular Cloud Cores, *in* D. P. Clemens & R. Barvainis, eds, 'Clouds, Cores, and Low Mass Stars', Vol. 65 of *Astronomical Society of the Pacific Conference Series*, p. 87.

Crutcher, R. M. (2001), Observations of Magnetic Fields in Molecular Cloud Cores, *in* T. Montmerle & P. André, eds, 'From Darkness to Light: Origin and Evolution of Young Stellar Clusters', Vol. 243 of *Astronomical Society of the Pacific Conference Series*, p. 27.

Crutcher, R. M., Wandelt, B., Heiles, C., Falgarone, E. & Troland, T. H. (2010), 'Magnetic Fields in Interstellar Clouds from Zeeman Observations: Inference of Total Field Strengths by Bayesian Analysis', *The Astrophysical Journal* **725**, 466–479.

Davis, Jr., L. & Greenstein, J. L. (1951), 'The Polarization of Starlight by Aligned Dust Grains.', *The Astrophysical Journal* **114**, 206.

Draine, B. T. (2011), *Physics of the Interstellar and Intergalactic Medium*, Princeton University Press.

Elmegreen, B. G. (1979), 'Magnetic diffusion and ionization fractions in dense molecular clouds - The role of charged grains', *The Astrophysical Journal* **232**, 729–739.

Enokiya, R., Torii, K., Schultheis, M., Asahina, Y., Matsumoto, R., Furuhashi, E., Nakamura, K., Dobashi, K., Yoshiike, S., Sato, J., Furukawa, N., Moribe, N., Ohama, A., Sano, H., Okamoto, R., Mori, Y., Hanaoka, N., Nishimura, A., Hayakawa, T., Okuda, T., Yamamoto, H., Kawamura, A., Mizuno, N., Onishi, T., Morris, M. R. & Fukui, Y. (2014), 'Discovery of Possible Molecular Counterparts to the Infrared Double Helix Nebula in the Galactic Center', *The Astrophysical Journal* **780**, 72.

Federrath, C. (2016), 'On the universality of interstellar filaments: theory meets simulations and observations', *Monthly Notices of the Royal Astronomical Society* **457**(1), 375–388. **URL:** *+ http://dx.doi.org/10.1093/mnras/stv2880*

Federrath, C., Rathborne, J. M., Longmore, S. N., Kruijssen, J. M. D., Bally, J., Contreras, Y., Crocker, R. M., Garay, G., Jackson, J. M., Testi, L. & Walsh, A. J. (2016), 'The

Link between Turbulence, Magnetic Fields, Filaments, and Star Formation in the Central Molecular Zone Cloud G0.253+0.016', *The Astrophysical Journal* **832**, 143.

Ferraro, V. C. A. (1937), 'The non-uniform rotation of the Sun and its magnetic field', *Monthly Notices of the Royal Astronomical Society* **97**, 458.

Ferrière, K. (2009), 'Interstellar magnetic fields in the Galactic center region', *Astronomy & Astrophysics* **505**, 1183–1198.

Fiege, J. D. & Pudritz, R. E. (2000*a*), 'Helical fields and filamentary molecular clouds - I', *Monthly Notices of the Royal Astronomical Society* **311**, 85–104.

Fiege, J. D. & Pudritz, R. E. (2000*b*), 'Helical fields and filamentary molecular clouds - II. Axisymmetric stability and fragmentation', *Monthly Notices of the Royal Astronomical Society* **311**, 105–119.

Fleck, Jr., R. C. (1980), 'Turbulence and the stability of molecular clouds', *The Astrophysical Journal* **242**, 1019–1022.

Franzmann, E. L. & Fiege, J. D. (2017), 'PolCat: Modelling submillimetre polarization of molecular cloud cores using successive parametrized coordinate transformations', *Monthly Notices of the Royal Astronomical Society* **466**, 4592–4613.

Gold, T. (1952), 'The alignment of galactic dust', *Monthly Notices of the Royal Astronomical Society* **112**, 215.

Goldreich, P. & Kwan, J. (1974), 'Molecular Clouds', *The Astrophysical Journal* **189**, 441–454.

Goodman, A. A., Crutcher, R. M., Heiles, C., Myers, P. C. & Troland, T. H. (1989), 'Measurement of magnetic field strength in the dark cloud Barnard 1', *The Astrophysical Journal Letters* **338**, L61–L64.

Guesten, R., Walmsley, C. M., Ungerechts, H. & Churchwell, E. (1985), 'Temperature determinations in molecular clouds of the galactic center', *Astronomy & Astrophysics* **142**, 381–387.

Güsten, R. (1989), Gas and Dust in the Inner Few Degrees of the Galaxy (review), *in* M. Morris, ed., 'The Center of the Galaxy', Vol. 136 of *IAU Symposium*, p. 89.

Güsten, R. & Downes, D. (1980), 'Formaldehyde in the galactic center region - Interpretation', *Astronomy & Astrophysics* **87**, 6–19.

Güsten, R., Walmsley, C. M. & Pauls, T. (1981), 'Ammonia in the neighbourhood of the galactic center', *Astronomy & Astrophysics* **103**, 197–206.

Hansen, C. J., Aizenman, M. L. & Ross, R. L. (1976), 'The Equilibrium and Stability of Uniformly Rotating, Isothermal Gas Cylinders', *The Astrophysical Journal* **207**, 736–744.

Heitsch, F. & Li, P. S. (2004), 'Theoretical expectations for magnetic field measurements in molecular cloud cores', *ArXiv Astrophysics e-prints* .

Henshaw, J. D., Longmore, S. N., Kruijssen, J. M. D., Davies, B., Bally, J., Barnes, A., Battersby, C., Burton, M., Cunningham, M. R., Dale, J. E., Ginsburg, A., Immer, K., Jones, P. A., Kendrew, S., Mills, E. A. C., Molinari, S., Moore, T. J. T., Ott, J., Pillai, T., Rathborne, J., Schilke, P., Schmiedeke, A., Testi, L., Walker, D., Walsh, A. & Zhang, Q. (2016), 'Molecular gas kinematics within the central 250 pc of the Milky Way', *Monthly Notices of the Royal Astronomical Society* **457**, 2675–2702.

Heyer, M., Krawczyk, C., Duval, J. & Jackson, J. M. (2009), 'Re-Examining Larson's Scaling Relationships in Galactic Molecular Clouds', *The Astrophysical Journal* **699**, 1092–1103.

Indriolo, N. & McCall, B. J. (2012), 'Investigating the Cosmic-Ray Ionization Rate in the

Galactic Diffuse Interstellar Medium through Observations of H^+_3', *The Astrophysical Journal* **745**, 91.

Jackson, J. (1975), *Classical electrodynamics*, Wiley.

Jackson, J. M., Geis, N., Genzel, R., Harris, A. I., Madden, S., Poglitsch, A., Stacey, G. J. & Townes, C. H. (1993), 'Neutral gas in the central 2 parsecs of the Galaxy', *The Astrophysical Journal* **402**, 173–184.

Jeans, J. H. (1902), 'The stability of a spherical nebula', *Philosophical Transactions of the Royal Society of London A: Mathematical, Physical and Engineering Sciences* **199**(312-320), 1–53.
URL: *http://rsta.royalsocietypublishing.org/content/199/312-320/1*

Kaur, A., Sood, N. K., Singh, L. & Singh, K. D. (2006), 'Differential Rotation in Self Gravitating Filaments', *Astrophysics and Space Science* **301**, 89–96.

Kawachi, T. & Hanawa, T. (1998), 'Gravitational Collapse of Filamentary Clouds', *Publications of the Astronomical Society of Japan* **50**, 577–586.

Killeen, N. E. B., Lo, K. Y. & Crutcher, R. (1992), 'Zeeman measurements of the magnetic fields at the Galactic center', *The Astrophysical Journal* **385**, 585–603.

Kirk, H., Klassen, M., Pudritz, R. & Pillsworth, S. (2015), 'The Role of Turbulence and Magnetic Fields in Simulated Filamentary Structure', *The Astrophysical Journal* **802**, 75.

Kolmogorov, A. (1941), 'The Local Structure of Turbulence in Incompressible Viscous Fluid for Very Large Reynolds' Numbers', *Akademiia Nauk SSSR Doklady* **30**, 301–305.

Koyama, K., Awaki, H., Kunieda, H., Takano, S. & Tawara, Y. (1989), 'Intense 6.7-keV iron line emission from the Galactic Centre', *Nature* **339**, 603–605.

Koyama, K., Maeda, Y., Sonobe, T., Takeshima, T., Tanaka, Y. & Yamauchi, S. (1996), 'ASCA View of Our Galactic Center: Remains of Past Activities in X-Rays?', *Publications of the Astronomical Society of Japan* **48**, 249–255.

Kritsuk, A. G., Lee, C. T. & Norman, M. L. (2013), 'A supersonic turbulence origin of Larson's laws', *Monthly Notices of the Royal Astronomical Society* **436**, 3247–3261.

Kruijssen, J. M. D., Dale, J. E. & Longmore, S. N. (2015), 'The dynamical evolution of molecular clouds near the Galactic Centre - I. Orbital structure and evolutionary timeline', *Monthly Notices of the Royal Astronomical Society* **447**, 1059–1079.

Kruijssen, J. M. D., Longmore, S. N., Elmegreen, B. G., Murray, N., Bally, J., Testi, L. & Kennicutt, R. C. (2014), 'What controls star formation in the central 500 pc of the Galaxy?', *Monthly Notices of the Royal Astronomical Society* **440**, 3370–3391.

Krumholz, M. R. & Kruijssen, J. M. D. (2015), 'A dynamical model for the formation of gas rings and episodic starbursts near galactic centres', *Monthly Notices of the Royal Astronomical Society* **453**, 739–757.

Lada, C. J., Alves, J. & Lada, E. A. (1999), 'Infrared Extinction and the Structure of the IC 5146 Dark Cloud', *The Astrophysical Journal* **512**, 250–259.

Lada, C. J., Lada, E. A., Clemens, D. P. & Bally, J. (1994), 'Dust extinction and molecular gas in the dark cloud IC 5146', *The Astrophysical Journal* **429**, 694–709.

Landau, L. & Lifshitz, E. (1987), *Fluid Mechanics*, Elsevier Science.

Landecker, T. L. (2012), 'The Role of Magnetic Fields in the Interstellar Medium of the Milky Way. Evidence from the Diffuse Polarized Radio Emission', *Space Science Reviews* **166**, 263–280.

Langer, W. D. & Penzias, A. A. (1990), 'C-12/C-13 isotope ratio across the Galaxy from observations of C-13/O-18 in molecular clouds', *The Astrophysical Journal* **357**, 477–492.

Langer, W. D., Velusamy, T., Morris, M. R., Goldsmith, P. F. & Pineda, J. L. (2017), 'Kinematics and properties of the central molecular zone as probed with [C ii]', *Astronomy & Astrophysics* **599**, A136.

LaRosa, T. N., Kassim, N. E., Lazio, T. J. W. & Hyman, S. D. (2000), 'A Wide-Field 90 Centimeter VLA Image of the Galactic Center Region', *The Astronomical Journal* **119**, 207–240.

Larson, R. B. (1981), 'Turbulence and star formation in molecular clouds', *Monthly Notices of the Royal Astronomical Society* **194**, 809–826.

Lazarian, A., Goodman, A. A. & Myers, P. C. (1997), 'On the Efficiency of Grain Alignment in Dark Clouds', *The Astrophysical Journal* **490**, 273–280.

Lis, D. C. & Goldsmith, P. F. (1991), 'High-density gas in the core of the Sagittarius B2 molecular cloud', *The Astrophysical Journal* **369**, 157–168.

Lis, D. C. & Menten, K. M. (1998), 'Infrared Space Observatory Long Wavelength Spectrometer Observations of a Cold Giant Molecular Cloud Core near the Galactic Center', *The Astrophysical Journal* **507**, 794–804.

Lombardi, M., Alves, J. & Lada, C. J. (2010), 'Larson's third law and the universality of molecular cloud structure', *Astronomy & Astrophysics* **519**, L7.

Longmore, S. N., Bally, J., Testi, L., Purcell, C. R., Walsh, A. J., Bressert, E., Pestalozzi, M., Molinari, S., Ott, J., Cortese, L., Battersby, C., Murray, N., Lee, E., Kruijssen, J. M. D., Schisano, E. & Elia, D. (2013), 'Variations in the Galactic star formation rate

and density thresholds for star formation', *Monthly Notices of the Royal Astronomical Society* **429**, 987–1000.

Mac Low, M.-M. & Klessen, R. S. (2004), 'Control of star formation by supersonic turbulence', *Reviews of Modern Physics* **76**, 125–194.

Matsumura, S., Oka, T., Tanaka, K., Nagai, M., Kamegai, K. & Hasegawa, T. (2012), 'Discovery of the Pigtail Molecular Cloud in the Galactic Center', *The Astrophysical Journal* **756**, 87.

Mauersberger, R., Henkel, C., Wilson, T. L. & Walmsley, C. M. (1986), 'Hot ammonia in the Galaxy', *Astronomy & Astrophysics* **162**, 199–210.

McKee, C. F. & Holliman, II, J. H. (1999), 'Multipressure Polytropes as Models for the Structure and Stability of Molecular Clouds. I. Theory', *The Astrophysical Journal* **522**, 313–337.

McKee, C. F. & Ostriker, E. C. (2007), 'Theory of Star Formation', *Annual Reviews of Astronomy and Astrophysics* **45**, 565–687.

McKee, C. F. & Zweibel, E. G. (1995), 'Alfven Waves in Interstellar Gasdynamics', *The Astrophysical Journal* **440**, 686.

McLaughlin, D. E. & Pudritz, R. E. (1996), 'A Model for the Internal Structure of Molecular Cloud Cores', *The Astrophysical Journal* **469**, 194.

Mills, E. A. C. (2017), 'The Milky Way's Central Molecular Zone', *ArXiv e-prints* .

Mills, E. A. C. & Morris, M. R. (2013), 'Detection of Widespread Hot Ammonia in the Galactic Center', *The Astrophysical Journal* **772**, 105.

Mizuno, A., Onishi, T., Hayashi, M., Ohashi, N., Sunada, K., Hasegawa, T. & Fukui, Y. (1994), 'Molecular cloud condensation as a tracer of low-mass star formation', *Nature* **368**, 719–721.

Morris, M., Polish, N., Zuckerman, B. & Kaifu, N. (1983), 'The temperature of molecular gas in the galactic center region', *The Astronomical Journal* **88**, 1228–1235.

Morris, M. R. (2014), 'Manifestations of the Galactic Center Magnetic Field', *ArXiv e-prints* .

Morris, M. & Serabyn, E. (1996), 'The Galactic Center Environment', *Annual Reviews of Astronomy and Astrophysics* **34**, 645–702.

Morris, M., Uchida, K. & Do, T. (2006), 'A magnetic torsional wave near the Galactic Centre traced by a "double helix" nebula', *Nature* **440**, 308–310.

Mouschovias, T. C. (1976), 'Nonhomologous contraction and equilibria of self-gravitating, magnetic interstellar clouds embedded in an intercloud medium: Star formation. I Formulation of the problem and method of solution', *The Astrophysical Journal* **206**, 753–767.

Mundy, L. G. (1994), Properties of Dark Cloud and Warm Cloud Cores, *in* D. P. Clemens & R. Barvainis, eds, 'Clouds, Cores, and Low Mass Stars', Vol. 65 of *Astronomical Society of the Pacific Conference Series*, p. 35.

Myers, P. C. & Goodman, A. A. (1988*a*), 'Evidence for magnetic and virial equilibrium in molecular clouds', *The Astrophysical Journal Letters* **326**, L27–L30.

Myers, P. C. & Goodman, A. A. (1988*b*), 'Magnetic molecular clouds - Indirect evidence for magnetic support and ambipolar diffusion', *The Astrophysical Journal* **329**, 392–405.

Nagasawa, M. (1987), 'Gravitational Instability of the Isothermal Gas Cylinder with an Axial magnetic Field', *Progress of Theoretical Physics* **77**, 635–652.

Nakano, T. & Nakamura, T. (1978), 'Gravitational Instability of Magnetized Gaseous Disks 6', *Publications of the Astronomical Society of Japan* **30**, 671–680.

Novak, G., Chuss, D. T., Renbarger, T., Griffin, G. S., Newcomb, M. G., Peterson, J. B., Loewenstein, R. F., Pernic, D. & Dotson, J. L. (2003), 'First Results from the Submillimeter Polarimeter for Antarctic Remote Observations: Evidence of Large-Scale Toroidal Magnetic Fields in the Galactic Center', *The Astrophysical Journal Letters* **583**, L83–L86.

Ostriker, E. C., Stone, J. M. & Gammie, C. F. (2001), 'Density, Velocity, and Magnetic Field Structure in Turbulent Molecular Cloud Models', *The Astrophysical Journal* **546**, 980–1005.

Ostriker, J. (1964), 'The Equilibrium of Polytropic and Isothermal Cylinders.', *The Astrophysical Journal* **140**, 1056.

Palmeirim, P., André, P., Kirk, J., Ward-Thompson, D., Arzoumanian, D., Könyves, V., Didelon, P., Schneider, N., Benedettini, M., Bontemps, S., Di Francesco, J., Elia, D., Griffin, M., Hennemann, M., Hill, T., Martin, P. G., Men'shchikov, A., Molinari, S., Motte, F., Nguyen Luong, Q., Nutter, D., Peretto, N., Pezzuto, S., Roy, A., Rygl, K. L. J., Spinoglio, L. & White, G. L. (2013), 'Herschel view of the Taurus B211/3 filament and striations: evidence of filamentary growth?', *Astronomy & Astrophysics* **550**, A38.

Pan, L. & Padoan, P. (2009), 'The Temperature of Interstellar Clouds from Turbulent Heating', *The Astrophysical Journal* **692**, 594–607.

Plante, R. L., Lo, K. Y. & Crutcher, R. M. (1995), 'The magnetic fields in the galactic center: Detection of H1 Zeeman splitting', *The Astrophysical Journal Letters* **445**, L113–L116.

Purcell, E. M. (1979), 'Suprathermal rotation of interstellar grains', *The Astrophysical Journal* **231**, 404–416.

Rathborne, J. M., Jackson, J. M. & Simon, R. (2006), 'Infrared Dark Clouds: Precursors to Star Clusters', *The Astrophysical Journal* **641**, 389–405.

Rathborne, J. M., Longmore, S. N., Jackson, J. M., Kruijssen, J. M. D., Alves, J. F., Bally, J., Bastian, N., Contreras, Y., Foster, J. B., Garay, G., Testi, L. & Walsh, A. J. (2014), 'Turbulence Sets the Initial Conditions for Star Formation in High-pressure Environments', *The Astrophysical Journal Letters* **795**, L25.

Recchi, S., Hacar, A. & Palestini, A. (2014), 'On the equilibrium of rotating filaments', *Monthly Notices of the Royal Astronomical Society* **444**(2), 1775–1782.
URL: *http://mnras.oxfordjournals.org/content/444/2/1775.abstract*

Rodríguez-Fernández, N. J., Martín-Pintado, J., Fuente, A., de Vicente, P., Wilson, T. L. & Hüttemeister, S. (2001), 'Warm H_2 in the Galactic center region', *Astronomy & Astrophysics* **365**, 174–185.

Rodríguez-Fernández, N. J., Martín-Pintado, J., Fuente, A. & Wilson, T. L. (2004), 'ISO observations of the Galactic center interstellar medium. Neutral gas and dust', *Astronomy & Astrophysics* **427**, 217–229.

Serabyn, E. & Guesten, R. (1991), 'The H II region G0.18-0.04: ionization of a molecular cloud by impact with a strong magnetic field', *Astronomy & Astrophysics* **242**, 376–387.

Serabyn, E., Lacy, J. H. & Achtermann, J. M. (1992), 'The compression of the M-0.02-0.07 molecular cloud by the Sagittarius A East shell source', *The Astrophysical Journal* **395**, 166–173.

Shafranov, V. D. (1956), 'The stability of a cylindrical gaseous conductor in a magnetic field', *The Soviet Journal of Atomic Energy* **1**(5), 709–713.
URL: *http://dx.doi.org/10.1007/BF01480907*

Shetty, R., Beaumont, C. N., Burton, M. G., Kelly, B. C. & Klessen, R. S. (2012), 'The linewidth-size relationship in the dense interstellar medium of the Central Molecular Zone', *Monthly Notices of the Royal Astronomical Society* **425**, 720–729.

Smith, M. D. & Mac Low, M.-M. (1997), 'The formation of C-shocks: structure and signatures.', *Astronomy & Astrophysics* **326**, 801–810.

Sofue, Y. (2007), 'The Galactic Center Molecular Tornado Driven by Magnetic Squeezing Mechanism', *Publications of the Astronomical Society of Japan* **59**, 189–198.

Solomon, P. M., Rivolo, A. R., Barrett, J. & Yahil, A. (1987), 'Mass, luminosity, and line width relations of Galactic molecular clouds', *The Astrophysical Journal* **319**, 730–741.

Swinbank, A. M., Papadopoulos, P. P., Cox, P., Krips, M., Ivison, R. J., Smail, I., Thomson, A. P., Neri, R., Richard, J. & Ebeling, H. (2011), 'The Interstellar Medium in Distant Star-forming Galaxies: Turbulent Pressure, Fragmentation, and Cloud Scaling Relations in a Dense Gas Disk at z = 2.3', *The Astrophysical Journal* **742**, 11.

Tielens, A. G. G. M. (2005), *The Physics and Chemistry of the Interstellar Medium*.

Tomisaka, K., Ikeuchi, S. & Nakamura, T. (1988*a*), 'Equilibria and evolutions of magnetized, rotating, isothermal clouds. II - The extreme case: Nonrotating clouds', *The Astrophysical Journal* **335**, 239–262.

Tomisaka, K., Ikeuchi, S. & Nakamura, T. (1988*b*), 'The equilibria and evolutions of magnetized, rotating, isothermal clouds. I - Basic equations and numerical methods', *The Astrophysical Journal* **326**, 208–222.

Torii, K., Enokiya, R., Morris, M. R., Hasegawa, K., Kudo, N. & Fukui, Y. (2014), 'Detailed Molecular Observations Toward the Double Helix Nebula', *The Astrophysical Journal Supplement Series* **213**, 8.

Troland, T. H. & Crutcher, R. M. (2008), 'Magnetic Fields in Dark Cloud Cores: Arecibo OH Zeeman Observations', *The Astrophysical Journal* **680**, 457–465.

Tsuboi, M., Handa, T. & Ukita, N. (1999), 'Dense Molecular Clouds in the Galactic Center Region. I. Observations and Data', *The Astrophysical Journal Supplement Series* **120**, 1–39.

Tsuboi, M., Kawabata, T., Kasuga, T., Handa, T. & Kato, T. (1995), 'Galactic Center Arc–Polarized Plumes Complex at 43 GHz', *Publications of the Astronomical Society of Japan* **47**, 829–836.

Weintraub, D. A., Goodman, A. A. & Akeson, R. L. (2000), 'Polarized Light from Star-Forming Regions', *Protostars and Planets IV* pp. 247–272.

Wilson, T. L., Rohlfs, K., Hüttemeister, S. & service), S. O. (2013), *Tools of Radio Astronomy*, Vol. Astronomy and Astrophysics Library, 6th ed. 2013 edn, Springer Berlin Heidelberg.

Wilson, T. L., Ruf, K., Walmsley, C. M., Martin, R. N., Batrla, W. & Pauls, T. A. (1982), 'Detection of the /8,8/ and /9,9/ absorption lines of ammonia - The hot molecular cloud toward SGR B2', *Astronomy & Astrophysics* **115**, 185–189.

Yusef-Zadeh, F., Hewitt, J. W. & Cotton, W. (2004), 'A 20 Centimeter Survey of the Galactic Center Region. I. Detection of Numerous Linear Filaments', *The Astrophysical Journal Supplement Series* **155**, 421–550.

Yusef-Zadeh, F., Morris, M., Slee, O. B. & Nelson, G. J. (1986), 'Nonthermal radio emission from the galactic center arc', *The Astrophysical Journal* **310**, 689–693.

Yusef-Zadeh, F., Roberts, D. A., Goss, W. M., Frail, D. A. & Green, A. J. (1996), 'Detection

of 1720 MHz Hydroxl Masers at the Galactic Center: Evidence for Shock-excited Gas and Milligauss Fields', *The Astrophysical Journal Letters* **466**, L25.